

**SEISMIC PERFORMANCE OF CONTROLLED OUTRIGGER ROCKING WALL SYSTEM
WITH DIFFERENT TYPES OF ENERGY DISSIPATION DEVICES**

by

Tianyang Qiao

B.Eng., Dalian University of Technology, 2017

A THESIS SUBMITTED IN PARTIAL FULFILLMENT OF
THE REQUIREMENTS FOR THE DEGREE OF

MASTER OF APPLIED SCIENCE

in

THE FACULTY OF GRADUATE AND POSTDOCTORAL STUDIES

(Civil Engineering)

THE UNIVERSITY OF BRITISH COLUMBIA

(Vancouver)

May 2020

© Tianyang Qiao, 2020

The following individuals certify that they have read, and recommend to the Faculty of Graduate and Postdoctoral Studies for acceptance, a thesis/dissertation entitled:

Seismic Performance of Controlled Outrigger Rocking Wall System with Different Types of Energy Dissipation Devices

submitted by Tianyang Qiao in partial fulfillment of the requirements for
the degree of Master of Applied Science
in Civil Engineering

Examining Committee:

Tony T.Y. Yang, Department of Civil Engineering, University of British Columbia
Supervisor

Yao Cui, Department of Civil Engineering, Dalian University of Technology
Additional Examiner

Abstract

Controlled Outrigger Rocking Wall (CORW) system is a novel earthquake resilient system which combines reinforced concrete wall with controlled rocking base hinge and outrigger system. At the end of the rocking base and the outrigger, different dampers are used to provide the supplemental energy dissipation needed, to control seismic response, and to reduce damage on structural walls. In this study, a 100-meter-tall prototype CORW building was designed using Equivalent Energy Design Procedure (EEDP). EEDP allows designers to design the CORW system to achieve different performance objectives under different levels of earthquake hazard. Based on the prototype design, five types of alternative dampers were selected to meet the design requirements. The seismic performance of the prototype CORW system with different dampers was systematically compared. First, hysteretic behaviors of the dampers were obtained from experimental tests. Second, constitutive models of the dampers were calibrated, and detailed finite element models of the CORW were developed. Third, nonlinear time history analyses were done for 25 combinations of dampers, with 39 input ground motions records under three hazard levels. To further validate the analyses, hybrid simulation was conducted, where two dampers were experimentally tested in laboratory, and the remainder of CORW system was simulated in a finite element program. The result shows that EEDP is efficient in designing CORW system with different types of dampers, and the performance of the CORW system is not significantly affected by different types of dampers. Hence, CORW can be used as an efficient alternative seismic force resisting system for high-rise buildings in high seismic zones.

Lay Summary

Controlled Outrigger Rocking Wall (CORW) is an innovative resilient structural system composed of concrete core wall, rocking base hinge and outrigger. A prototype CORW building was designed using Equivalent Energy Design Procedure (EEDP). Five types of dampers were selected according to design requirements. Experimental tests were conducted to obtain hysteretic behavior of the dampers. Finite element models of the CORW with different dampers were developed and subjected to different levels of ground motion excitations. The result is further validated by experimental method. The result shows that the performance of the CORW system is not significantly affected by different types of dampers. The result also indicates CORW can be efficiently designed using EEDP, where the CORW can be used as a high-performance structural system for seismic applications.

Preface

This thesis is an original, independent work of the author, Tianyang Qiao. The author was responsible for the literature review, equation derivation, numerical model development, computational analysis, experimental setup, data processing and presentation of this manuscript. This thesis has been written and revised by the author with the advisory of Prof. Tony T. Y. Yang at the Department of Civil Engineering of the University of British Columbia. It is worth noting that this thesis is also summarized into a journal article which is currently under review.

Table of Contents

Abstract.....	iii
Lay Summary	iv
Preface.....	v
Table of Contents	vi
List of Tables	x
List of Figures.....	xi
List of Symbols	xv
List of Abbreviations	xviii
Acknowledgements	xx
Dedication	xxi
Chapter 1: Introduction	1
1.1 Background.....	1
1.2 Metallic Yielding Dampers in Rocking Walls.....	2
1.2.1 MYD in PRESSSS System	2
1.2.2 MYD in Single Rocking System.....	4
1.2.3 MYD in PreWec System.....	6
1.3 Viscous Dampers in Rocking Walls	8
1.4 Self-Centering Dampers in Rocking Walls	9

1.5	Viscous Dampers in Damped Outrigger Systems	10
1.6	Metallic Yielding Damper in Damped Outrigger System	12
1.7	Controlled Outrigger Rocking Wall System with Different Dampers	14
1.8	Objectives and Research Scope	15
1.9	Thesis Organization	15
Chapter 2: Equivalent Energy Design Procedure of CORW System		17
2.1	Current Design Approach	17
2.2	Equivalent Energy Design Procedure	17
2.3	Design of CORW System	18
2.4	Design of Energy Dissipators	27
2.4.1	Self-centering Damper	28
2.4.2	Metallic Yielding Damper	29
2.4.3	Fluid Viscous Damper	30
2.4.4	Viscoelastic Damper	31
Chapter 3: Prototype CORW Building		34
3.1	Introduction to Prototype Building	34
3.2	Design of Prototype Building	35
3.3	Selection of Energy dissipators	37
3.3.1	Resilient Slip Friction Joint	37
3.3.2	Filler-free Buckling Restraint Fuse	38

3.3.3	Fluid Viscous Damper	39
3.3.4	Viscoelastic Damper	39
3.4	Controlled Rocking Base Hinge	39
Chapter 4: Numerical Modeling of CORW System.....		42
4.1	Modeling of CORW Prototype.....	42
4.1.1	Modeling of Rocking Base	44
4.1.2	Modeling of Outrigger System	46
4.1.3	Modeling of Structural Wall	47
4.2	Validation of Numerical Modeling of Rocking Base Hinge	47
4.3	Modeling of CORW Dampers.....	50
4.4	Ground Motion Selection	53
4.5	Damping Settings	56
Chapter 5: Nonlinear Time History Analysis.....		57
5.1	Results of Prototype Combination.....	57
5.1.1	Roof Drift.....	57
5.1.2	Yielding States.....	58
5.2	Comparison of Different Damper Combinations	58
5.2.1	Hysteretic Loops of Dampers	59
5.2.2	Roof Drift.....	62
5.2.3	Story Response	64

Chapter 6: Experimental Testing..... 69

6.1 Experimental setup 69

6.2 Instrumentations 71

6.3 Component Testing 73

6.3.1 Loading Protocol..... 73

6.3.2 Results and Discussions..... 74

6.4 Hybrid Simulation of CORW System 77

6.4.1 Input Ground Motion..... 78

6.4.2 Hybrid Control Strategy..... 79

6.4.3 Hybrid Simulation Algorithm..... 80

6.4.4 Hybrid Simulation Results and Validations..... 81

Chapter 7: Conclusion..... 84

Bibliography 86

Appendices..... 91

List of Tables

Table 2.1. Design objectives, hazard and structural behaviors of CORW system.....	20
Table 3.1. Summarize of design parameters of the prototype CORW.....	36
Table 3.2. Summarize of prototype damper design parameters.....	36
Table 3.3. Design parameters of self-centering damper (SCD).....	38
Table 3.4. Design parameters of filler-free buckling restraint fuse (FFBRF).....	38
Table 3.5. Parameters of fluid viscous damper (FVD)	39
Table 3.6. Parameters of viscous elastic damper (VED)	39
Table 4.1. Numerical model matrix for prototype CORW system	43
Table 4.2. Natural periods of the prototype (first 3 modes).....	54
Table 4.3. Ground motion information and scaling.....	55

List of Figures

Figure 1.1. PRESSS rocking wall system (Perez, 2004).....	3
Figure 1.2. MYD in PRESSS system (Restrepo & Rahman, 2007a).....	4
Figure 1.3. Rocking wall with externally mounted dampers (Marriott, 2009)	5
Figure 1.4. Damage states of rocking wall with externally mounted dampers (Marriott, 2009)	5
Figure 1.5. Pin-Supported Wall system (Qu et al., 2012).....	6
Figure 1.6. Steel damper in Pin-Supported Wall system (Qu et al., 2012).....	6
Figure 1.7. Schematic view of PreWEC system (Sritharan et al., 2015)	7
Figure 1.8. UFP in PreWec System (K. Twigden & Henry, 2015).....	8
Figure 1.9. PRESSS rocking wall system with viscous brace dampers (Yahya C Kurama, 2000)	9
Figure 1.10. Rocking wall with Resilient Slip Friction Joint (Ashkan Hashemi et al., 2018).....	10
Figure 1.11. Cantilever beam analytical model for damped outrigger system (Chen et al., 2010).....	11
Figure 1.12. Buckling restraint brace (BRB) outrigger damper (Lin et al., 2018).....	12
Figure 1.13. Shake-table test of combined viscously damped and BRB-damped outrigger (Xing et al., 2019)	13
Figure 1.14. Controlled Outrigger Rocking Wall (CORW) system with different types of energy dissipators	14
Figure 2.1. Concept of Equivalent Energy Design Procedure (EEDP).....	18
Figure 2.2. Concept and objectives of CORW system.....	19

Figure 2.3. Trilinear backbone curve and performance objectives of CORW system.....	20
Figure 2.4. EEDP design for SLE level	23
Figure 2.5. Schematic view of primary and secondary system.....	26
Figure 2.6. Typical hysteresis of self-centering damper (SCD).....	29
Figure 2.7. Typical hysteresis of metallic yielding damper (MYD).....	30
Figure 2.8. Typical force-deformation relation of fluid viscous damper (FVD)	31
Figure 2.9. Typical hysteresis of viscous elastic damper (VED).....	32
Figure 3.1. Geometry of CORW prototype building	35
Figure 3.2. Resilient Slip Friction Joint (A Hashemi et al., 2018).....	37
Figure 3.3. Schematic view of Controlled Rocking Base Hinge (CRBH) for tall resilient wall systems	40
Figure 3.4. Rocking and sliding shear.....	41
Figure 4.1. Schematic view of CORW system with different dampers	44
Figure 4.2. Modeling of rocking base	45
Figure 4.3. Numerical model of the prototype building.....	46
Figure 4.4. Schematic view of numerical model for validating rocking base and wall elements modeling	48
Figure 4.5. Schematic view of modeling of rocking base for validation	48
Figure 4.6. Validation of numerical modeling techniques for rocking base and wall elements	49
Figure 4.7. Stress and deformation of base springs	49

Figure 4.8. Modeling of FVD and VED	51
Figure 4.9. Experimental validations of modeling of CORW dampers	52
Figure 4.10. Response spectra of all scaled ground motions (SLE)	53
Figure 4.11. Response spectra of all scaled ground motions (DBE)	53
Figure 4.12. Response spectra of all scaled ground motions (MCE).....	54
Figure 5.1. Comparison between EEDP design and prototype results from nonlinear time history analysis	57
Figure 5.2. Local deformation of the EPP dampers	58
Figure 5.3. Sample ground motion selected for comparison	60
Figure 5.4. Ground motion acceleration time history	60
Figure 5.5. Outrigger damper hysteretic loops	61
Figure 5.6. Base damper hysteretic loops	62
Figure 5.7. Roof drift of 25 combinations from nonlinear time history analysis.....	63
Figure 5.8. Median structural response comparison for damper combinations under MCE.....	65
Figure 5.9. Damper deformation comparison for all combinations under MCE	67
Figure 5.10. Damper force comparison for all combinations under MCE.....	68
Figure 6.1. Schematic view of experimental testing setup.....	70
Figure 6.2. Experimental testing setup.....	71
Figure 6.3. Instrumentation setup	72
Figure 6.4. Sources of slippage in experimental testing setup.....	73

Figure 6.5. Loading protocol for HF2V	74
Figure 6.6. Component test result: force-deformation hysteresis of HF2V device 1.....	75
Figure 6.7. Component test result: force-deformation hysteresis of HF2V device 2.....	75
Figure 6.8. Component test result: connection slippage of HF2V	76
Figure 6.9. Component test result: force-deformation hysteresis of HF2V (end-to-end deformation)...	76
Figure 6.10. Schematic view of hybrid model	78
Figure 6.11. Ground motion time history for hybrid simulation.....	78
Figure 6.12. Response spectrum of the ground motion for hybrid simulation.....	79
Figure 6.13. Control loop diagram of hybrid low-level controller.....	79
Figure 6.14. Roof drift time history comparison between hybrid simulation and analytical simulation	81
Figure 6.15. Base moment time history comparison between hybrid simulation and analytical simulation	82
Figure 6.16. Damper displacement comparison between hybrid simulation and analytical simulation .	83
Figure 6.17. Damper force time history comparison between hybrid simulation and analytical simulation	83

List of Symbols

α = Damping exponent

β = Flag-shape hysteresis control parameter

λ = Damping constant of viscous damper

b = Post-yielding stiffness

C = Damping coefficient

D^{BM} = Roof drift of the prototype

D_y = Yielding roof drift of the ENLSDOF system

D_p = Plastic roof drift of the ENLSDOF system

D_u = Ultimate roof drift of the ENLSDOF system

d = Damper deformation

d_u = Damper ultimate design deformation

d_{OR} = Outrigger damper deformation

d_{BS} = Base damper deformation

F = Base shear

F_y = Yielding base shear of the ENLSDOF system

F_p = Plastic base shear of the ENLSDOF system

F_{PR} = Distributed base shear of the primary system

F_{SE} = Distributed base shear of the secondary system

f = Damper force

f_c' = Compressive strength of concrete

f_{OR} = Outrigger damper force

f_{BS} = Base damper force

f_u = Damper ultimate design force

$f_{u,OR}$ = Designed ultimate outrigger damper force

$f_{u,BS}$ = Designed ultimate base damper force

f_y = Yielding force of damper or reinforcing steel

f_{ye} = Effective yielding force

K_{eff} = Effective stiffness of the ELSDOF system

k = Damper initial stiffness

k_1 = Non-EPP damper initial stiffness

k_2 = Damper post-yielding stiffness

M = Moment

M^{BM} = Overturning moment of the prototype

M_u = Ultimate overturning moment

m = Mass of the system

S_a = Pseudo-acceleration

S_d = Pseudo-displacement

S_v = Pseudo-velocity

T = Natural period

T_{eff} = Effective period of the ELSDOF system

v_u = Damper ultimate velocity

List of Abbreviations

CORW = Controlled Outrigger Rocking Wall

CP = Collapse Prevention

CRBH = Controlled Rocking Base Hinge

DBE = Design Base Earthquake

DOF = Degree-of-freedom

DC = Displacement-based Control

DHS = Displacement-based Hybrid Simulation

DOF = Degree-of-freedom

EEDP = Equivalent Energy Design Procedure

ELSDOF = Equivalent Linear Single-Degree-of-Freedom

ENLSDOF = Equivalent Nonlinear Single-Degree-of-Freedom

EPP = Elastic-Perfectly-Plastic

FVD = Fluid Viscous Damper

HF2V = High-force-to-volume

HS = Hybrid Simulation

IDA = Incremental Dynamic Analysis

ISDR = Inter-story Drift Ratio

LFRS = Lateral Force Resisting System

MCE = Maximum Credible Earthquake

MDOF = Multi-degree-of-freedom

MYD = Metallic Yielding Damper

NLTHA = Non-linear Time History Analysis

PID = Proportional-integral-derivative

PRESSS = Precast Seismic Structural Systems

PREWEC = Precast Wall with End Columns

PT = Prototype

RDR = Roof drift ratio

RR = Rapid Recover

RSFJ = Resilient Slip Friction Joint

SCD = Self-Centering Damper

SDOF = Single-degree-of-freedom

SLE = Service Level Earthquake

SFRS = Seismic Force Resisting System

VED = Viscoelastic Damper

Acknowledgements

Almost three years have passed since I came to the University of British Columbia for the first time. Filled with both joy and efforts, my postgraduate study witnessed my growth and improvement. This thesis, to terminate my campus life in UBC, is the gift granted to everyone who supports me.

First and foremost, my deepest gratitude goes to my supervisor, Prof. Tony T. Y. Yang, without whose intellectual guidance and constant encouragement, impossible would this thesis come into being. I have seen the patience and prudence when he revised the drafts repeatedly and pinpointed the insufficient. He taught me how to be professional and to do the right thing even when the road got tough. I also wish to express my sincere appreciation to Prof. Geoffrey W. Rodgers from University of Canterbury, who kindly offers me experimental specimens as well as many valuable suggestions.

Meanwhile, I wish to thank my fellow lab mates, especially Lisa Tobber, for the stimulating discussions, insightful comments, and sleepless nights we were working together before the final deadline. My thesis could not be finished without you. Also, I specially thank Ryan Xu Xie for his help on my research topics and hybrid simulation setup. I would also like to thank my team members: Xi Zuo, Dorian Tung, Xiao Pan, Henry Xu and Soham Vaze, for their assistance in my experimental setup and research work.

My sincere gratitude goes to my parents who provided me with unfailing support and continuous encouragement throughout my years of study and through the process of researching and writing this thesis.

Special thanks go to my dearest girlfriend, Yumeng Lin, who accompanied with me throughout the arduous journey of completing the thesis and the toughest time during the COVID-19 crisis. Her love, encouragement, and patience are the brightest sunshine shining after those rainy days.

Dedication

This thesis is dedicated to my dearest mother Lin Xu, my father Xiangbin Qiao and my lovely girlfriend Yumeng Lin. Words cannot express how thankful I am to have you.

Chapter 1: Introduction

1.1 Background

Reinforced concrete (RC) structural wall systems are one of the popular seismic force resisting system (SFERS) for tall buildings in high seismic zones all over the world. Most conventional RC walls are designed to achieve the collapse prevention (CP) performance objective under high intensity ground motions. RC walls are designed to form plastic hinges at the base, where concrete is expected to crush and reinforcing bars will yield. This may result in severe and irreversible damage to both the structural and non-structural components in the building. Severe structural damage is difficult to repair and can result in hefty direct and indirect economic losses. As such, next-generation earthquake engineering is pushing towards resilient structural systems designed for no or low earthquake damage under strong earthquake shaking intensities.

Rocking mechanism is an effective mechanism to prevent structural damage during earthquakes. Rocking mechanism has been systematically examined in the precast seismic structural systems (PRESS) research program (Perez, 1998; Priestley et al., 1999), where a 5-story prototype building with rocking frame in one direction and rocking wall in the other direction has been experimentally tested. In the PRESS project, post-tensioning (PT) tendons were used to tie the wall and frame to the foundation. During the earthquake shaking, the bases of the wall and column were designed to uplift and returned to the original position by the gravity and PT tendon forces. This results in a nonlinear elastic lateral force-deformation response, which makes the system self-center and damage free (Belleri et al., 2014; Kurama et al., 1999b; Nazari et al., 2017; Qu et al., 2012; Twigden et al., 2017). However, pure rocking system may create uncontrolled displacement and acceleration.

One of the most effective methods to control rocking mechanism is through the use of energy dissipation devices (Restrepo & Rahman, 2007a). Depending on the damper type, dampers can absorb earthquake energy through sliding friction, material plastic deformations, and the deforming of viscous fluids. Different

damper types have been incorporated in RC walls in various ways, including controlled rocking systems and in outrigger systems. This section introduces several applications of the use of dampers in RC walls and the corresponding performance.

1.2 Metallic Yielding Dampers in Rocking Walls

Metallic Yielding Dampers (MYD) were researched by many researchers as an energy dissipation solution for rocking systems. Commonly used MYD include mild steel damper, Buckling-Restrained Fuse (BRF) (Liu & Palermo, 2020), honeycomb steel damper (Yang et al., 2019), Welded Wide Flange Fuse (WWFF) (T.Y. Yang et al., 2018), etc.

1.2.1 MYD in PRESSS System

In 1990s, a series of experimental tests were conducted by a joint US-Japan seismic research program called PRESSS (Precast Seismic Structural System). A precast rocking wall system with unbonded post-tensioning was developed and tested (Y. Kurama et al., 1999a; Y. Kurama et al., 1999b; Yahya Cuneyt Kurama, 1997). This system is composed of multiple precast wall panels with spiral confined concrete at rocking toes and unbonded PT tendons. During the earthquake shaking, the bases of the wall and column were designed to uplift and returned to the original position by the gravity and PT tendon forces. PT tendons are designed to be elastic in design-level earthquakes, so they are able to provide restoring forces to re-center the wall. This results in a nonlinear elastic lateral force-deformation response, which makes the system self-centering and damage-free.

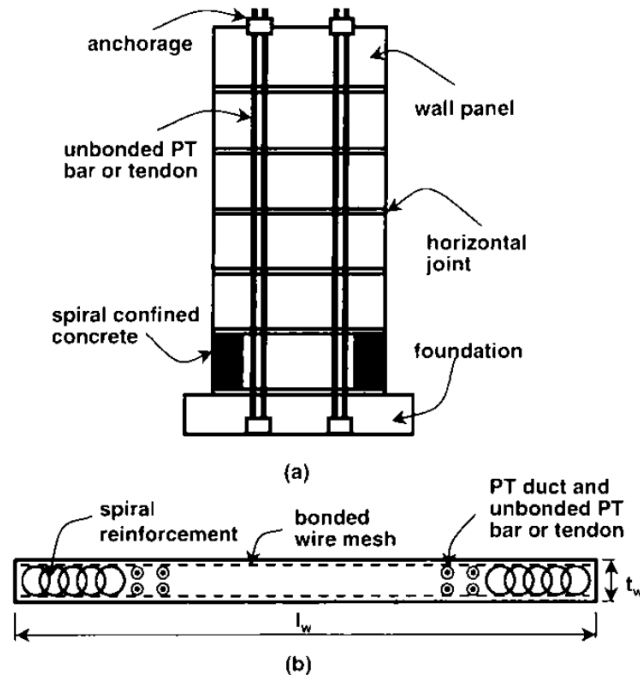


Figure 1.1. PRESSS rocking wall system (Perez, 2004)

Restrepo & Rahman (2007b) proposed dog-bone shape metallic energy dissipators installed in the PRESSS rocking wall system as shown in Figure 1.2,. These energy dissipators are made from mild reinforcing bars. One side of the energy dissipator is casted into the precast rocking wall, while the other side is welded to an anchor plate at foundation. During rocking, these bars yield in tension or compression, contributing to moment resistance and energy dissipation. This type of rocking wall has a better energy dissipation capacity provided by energy dissipators, and still can self-center due to the gravity load and additional PT load.

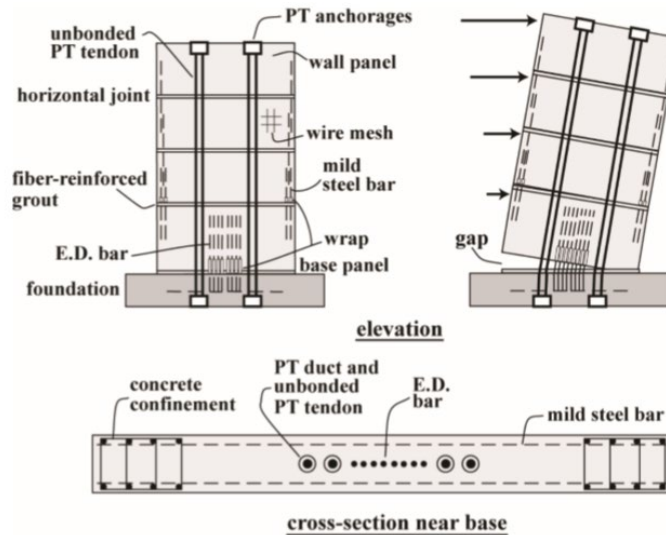


Figure 1.2. MYD in PRESSS system (Restrepo & Rahman, 2007a)

1.2.2 MYD in Single Rocking System

Sritharan et al. (2007) proposed a U-Shape Flexural Plate (UFP) connector installed vertically between wall panels. The UFPs are supposed to dissipate energy by plastic deformation due to the slipping between wall panels. The UFPs could also contribute to self-centering restoring force, together with gravity loads and PT.

Marriott (2009) proposed and experimentally tested a rocking wall system with externally-mounted metallic yielding dampers. Figure 1.3 shows the experimental setup. Steel yielding type dampers were installed externally near a planar wall, which is easy to construct and repair after earthquake. Confining steel channels with welded reinforcing bars are specially designed to protect rocking toes. From the results of the dynamic test shown in Figure 1.4, minor damage of the wall is observed, and the hysteresis shows that the system dissipated energy effectively and has a self-centering feature. The structural response is also well controlled due to the energy dissipation provided by MYD.

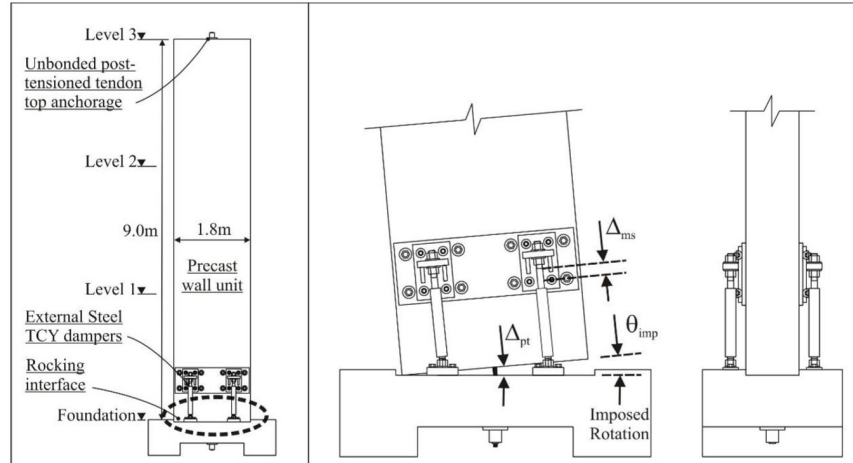


Figure 1.3. Rocking wall with externally mounted dampers (Marriott, 2009)



Figure 1.4. Damage states of rocking wall with externally mounted dampers (Marriott, 2009)

Pin-supported rocking wall is an alternative rocking wall system, composed of steel diagonal braces, pin bearing and embedded steel beam. Figure 1.5 shows typical pin-supported rocking wall system. The use of metallic dampers has been investigated by many researchers (Pan et al., 2015; Qu et al., 2012). It was observed that the metallic yielding damper installed between rocking wall and the remaining frame structure can effectively control the deformation pattern of the frame and further avoid frame failure. They further concluded that pin-supported rocking wall with metallic yielding damper was an efficient way of seismic retrofitting.

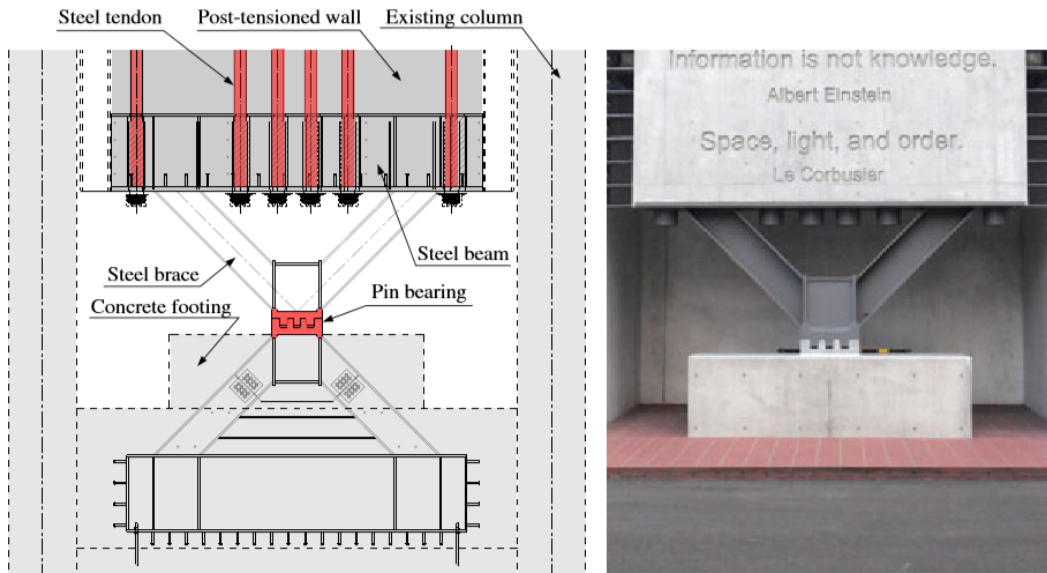


Figure 1.5. Pin-Supported Wall system (Qu et al., 2012)

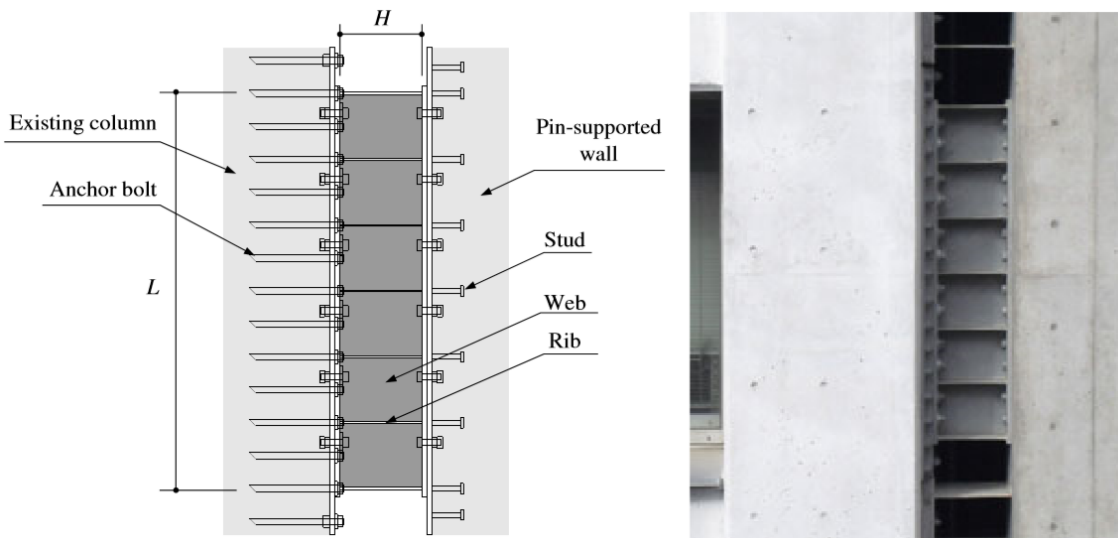


Figure 1.6. Steel damper in Pin-Supported Wall system (Qu et al., 2012)

1.2.3 MYD in PreWec System

Sritharan et al. (2015) proposed Precast Wall with End Column (PreWec) system, which is composed of a post-tensioned single precast rocking wall panel with two end columns at each side of the wall, as shown in Figure 1.7. In PreWec system, several types of metallic yielding energy dissipators were installed

between the wall panel and end columns: notched shear plate (NSP), slotted flexural plate (SFP), inclined flat bar (IFB), X shaped axial plate (XAP), pinned tension strut (PTS), U-shaped flexural plate (UFP), etc. Figure 1.8 shows a sample MYD composed of UFPs, which dissipates energy through hysteretic plastic deformation. The wall and columns are joined horizontally using special shear connectors along the vertical joints connect those MYDs. This type of wall configuration is especially suitable for multiple MYD devices. The experimental results show that PreWec with metallic yielding dampers shows low-damage and self-centering features, and the drift is also well controlled.

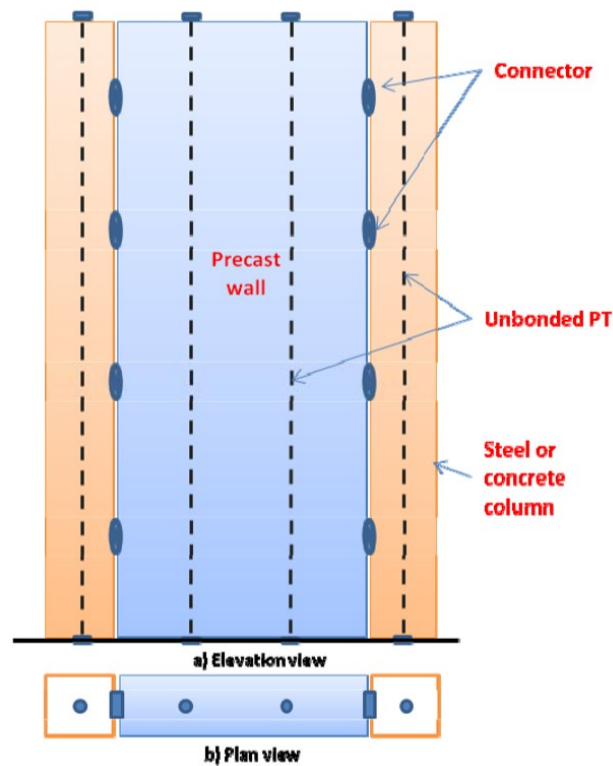


Figure 1.7. Schematic view of PreWEC system (Sritharan et al., 2015)

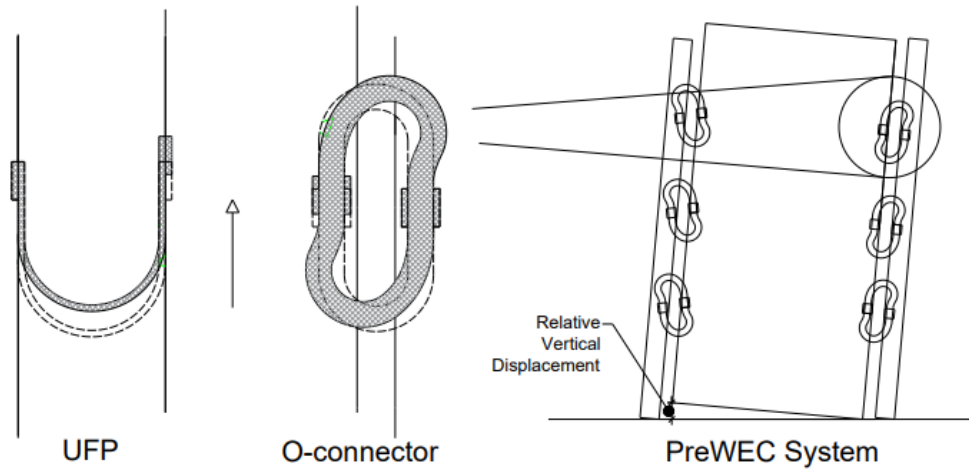


Figure 1.8. UFP in PreWec System (K. Twigden & Henry, 2015)

1.3 Viscous Dampers in Rocking Walls

Viscous damper is frequently applied for supplemental energy dissipation in structural systems. The design and behavioral investigation of viscous damper in conventional structural systems has been done by many researchers (Landi et al., 2014; Ramirez, 2001; Seleemah & Constantinou, 1997).

Application of viscous dampers in rocking wall system has been investigated by Kurama (2000). As shown in Figure 1.9, Kurama proposed a joint rocking wall system with supplemental viscous dampers installed as diagonal braces between gravity frames surrounding the wall, as an extension to PRESSS system. During rocking, due to wall uplift and gap opening at base, lateral drift and velocity occurs between the jointed wall and the gravity system, and the viscous dampers start to dissipate energy. It was observed that viscous damper is effective in controlling the structural response of rocking wall. Nonlinear dynamic analyses show that the drift is well controlled, and damage of the wall is limited only to the rocking corners.

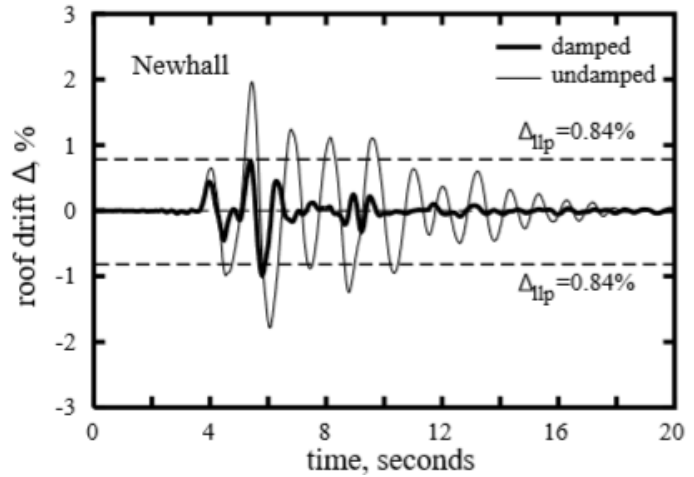
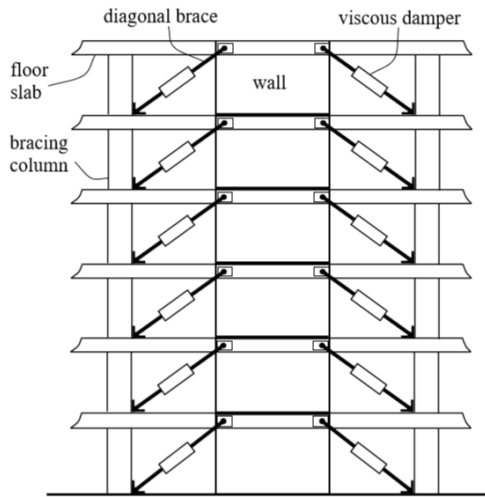
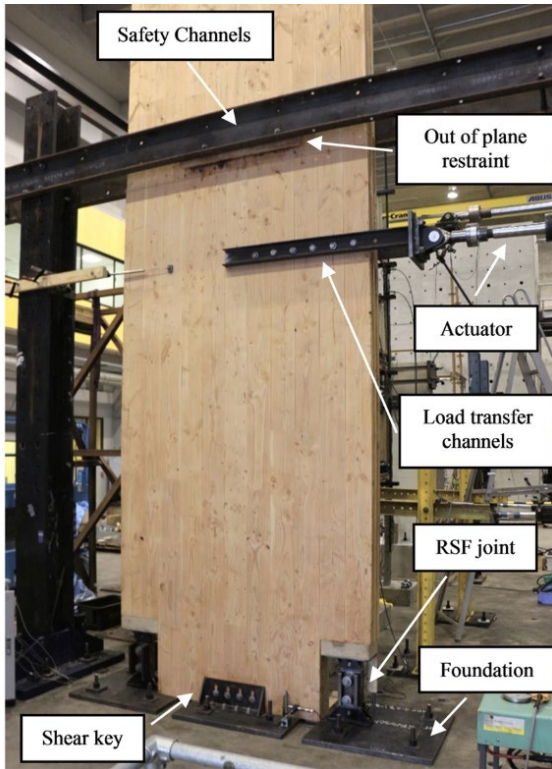


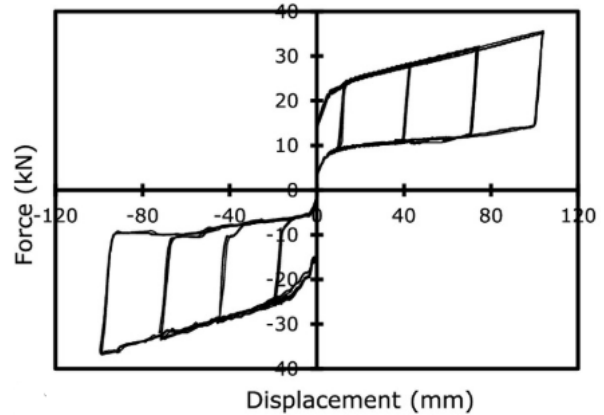
Figure 1.9. PRESSS rocking wall system with viscous brace dampers (Yahya C Kurama, 2000)

1.4 Self-Centering Dampers in Rocking Walls

Dampers with a flag-shaped self-centering force-deformation relationship is named self-centering dampers (SCD) in this study. Resilient Slip Friction Joint (RSFJ) is an innovative friction device that is capable of re-center upon unloading, with a flag-shape self-centering hysteresis as shown in Figure 1.10. Additional restoring force offered by RSFJ could efficiently eliminate residual displacement or force in the structural system. Short timber walls are usually light and not easy to re-center after earthquake. Some post-tensioning might be required. In the study, the Cross-Laminated Timber (CLT) structure equipped with RSFJ (Hashemi et al., 2018) is found to self-center without any additional gravity load or post-tensioning. It is concluded that self-centering dampers offer energy dissipation and self-centering in one pack, which is ideal for structures that requires extra restoring force to become resilient. Furthermore, the observed residual drift and force in the system are also minor, indicating the RSFJ is also excellent in energy dissipation and response control.



(a) Cross-Laminated Timber rocking wall with RSFJ



(b) Typical hysteresis of RSFJ

Figure 1.10. Rocking wall with Resilient Slip Friction Joint (Ashkan Hashemi et al., 2018)

1.5 Viscous Dampers in Damped Outrigger Systems

Outrigger system is commonly used in tall buildings. The use of outrigger system can effectively reduce the capacity demand of wall elements, resulting in a potentially larger floor area and less concrete and reinforcing material. Adding damping to outrigger system could further enhance the performance of tall building structures. To add damping at outrigger, multiple types of outrigger dampers have been researched and improved, including viscous dampers, viscoelastic dampers, and metallic dampers. Viscous damper is the conventional option for outrigger damper.

The idea of viscously damped outrigger system was initiated by Smith & Willford (2007). In their research, different types of dampers were proposed to be placed at the connection of outrigger and columns.

These dampers include fluid viscous dampers and viscoelastic dampers. Dynamic behaviors of outrigger system with or without dampers are systematically compared. They found out that adding dampers to the outrigger not only contributes to resisting wind effects, but also helps to reduce seismic response. Equipped with various types of dampers, the damped outrigger was found to be able to increase structural damping by a factor of 5~10. The use of outrigger could reduce the structural response by 30%, and net floor area by 2%. Thus, damping outrigger could enhance seismic performance and reduce response while retaining the cost-efficiency of conventional outrigger system.

With the early findings on damped outrigger system, researchers started to investigate the seismic behavior of damped outrigger system. Chen et al. (2010) proposed a beam- analysis model for tall buildings with damped outriggers. This model is composed of a cantilever beam with dashpots, which inspired further research on modeling of outrigger system behaviors, as shown in Figure 1.11. Based on the model, an explicit form for the complex modes was determined and for complex eigenvalues were solved to determine damping, outrigger design values and optimal damper position and sizing. Empirical equations were also proposed for engineering use. This numerical approach was further improved by Huang & Takeuchi (2017). Using this improved analysis approach, they concluded that the optimal outrigger location would be between 50~80% of the height of building, and the optimal damping parameter would be within 0.5~1. The damping parameter can be used to size outrigger dampers.

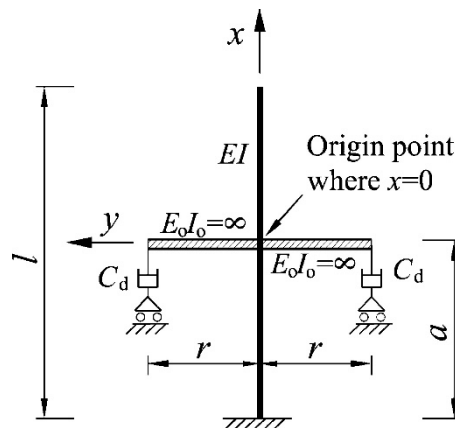


Figure 1.11. Cantilever beam analytical model for damped outrigger system (Chen et al., 2010)

Zhou & Li (2014) investigated the use of viscous dampers in outrigger system using nonlinear time history analysis. They concluded that it worked not as ideal as expected for low-intensity earthquakes. However, the viscously damped outrigger worked better under strong motions, providing around 4% of additional damping ratio.

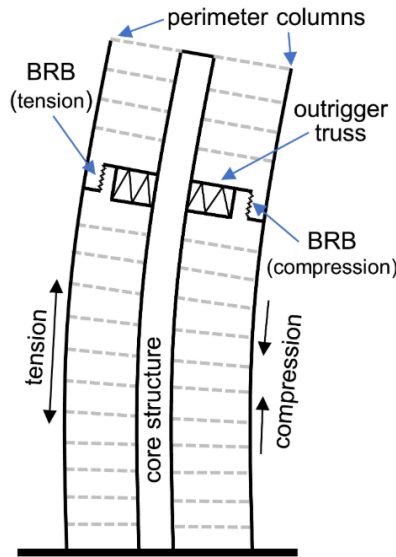


Figure 1.12. Buckling restraint brace (BRB) outrigger damper (Lin et al., 2018)

1.6 Metallic Yielding Damper in Damped Outrigger System

As a commonly used metallic yielding damper, buckling restraint brace (BRB) is also popular for damped outrigger systems. Lin et al. (2018) studied damped outrigger system with BRBs using 3 prototype buildings, with 64, 128 and 256 m building height, respectively. They concluded that BRB-damped outrigger has an optimal performance at 60~80% of the building height, and the stiffness of the BRB as outrigger damper should also be controlled within a reasonable range to control force demand in the structure while providing optimal energy dissipation. Zhou et al. (2017) compared the behavior of a conventional buckling brace with a BRB as the energy dissipating element in an outrigger. Additionally, they studied the use of BRBs in high-rise buildings using nonlinear time history analysis. Their results showed that the use of 48 BRB

members increases the damping on the building by 0.5%. Additionally, the use of well-designed BRBs protect the structure from severe damage.

The combined energy dissipation for outrigger system was investigated by (Xing et al., 2019). An optimal combination of viscous damper and BRBs for outrigger was proposed. As shown in (Xing et al., 2019), small-scale shake-table test has been conducted to study the combined damped outrigger system behavior. They concluded that the combined damped outrigger system has better performance when BRB placed higher than viscous dampers. The location of two types of dampers have significant influence on structural performance.

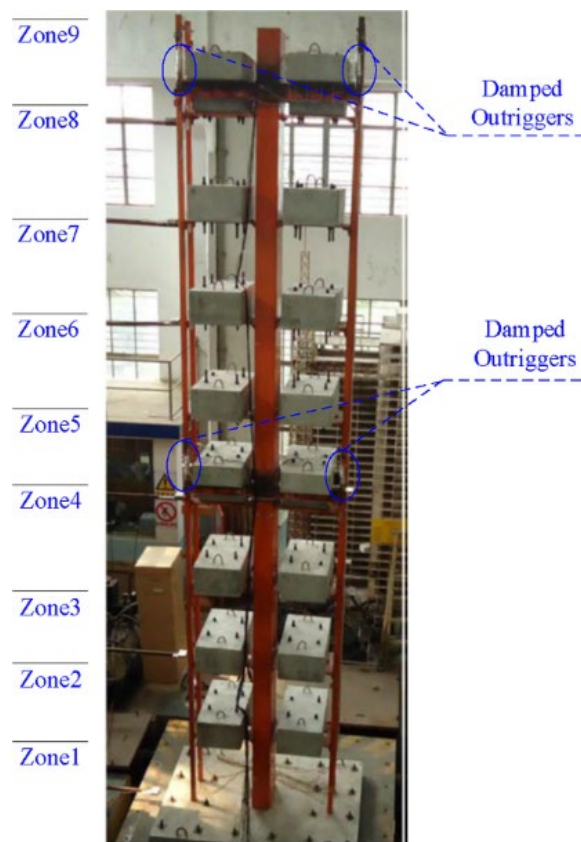


Figure 1.13. Shake-table test of combined viscously damped and BRB-damped outrigger (Xing et al., 2019)

1.7 Controlled Outrigger Rocking Wall System with Different Dampers

Both the application of self-centering and damped outrigger system in high-rise structural wall systems was successful. However, it is noted that damped outrigger wall system is based on a fix-base wall. Although damped outrigger performs well in reducing structural response in strong earthquakes, plastic hinge may still form at the base of wall, which leads to difficulties in repair after strong earthquake. In this study, damped outrigger system is combined with rocking base to achieve an alternative high-performance solution for tall buildings in terms of resilience. It is also observed that rocking may introduce unexpected structural response.

To overcome the deficiencies of both, a novel earthquake-resilient Controlled Outrigger Wall System (CORW) was proposed by Tobber et al. (2018) which combines concrete wall with rocking base and outrigger. Dampers are added at the base of the wall and at the end of the outrigger. Figure 1.14a shows the concept of the CORW. In this study, the performance of CORW with five different types of dampers is investigated, including self-centering damper (SCD), metallic yielding damper (MYD), fluid viscous damper (FVD) and viscos-elastic damper (VED), as shown in Figure 1.14b.

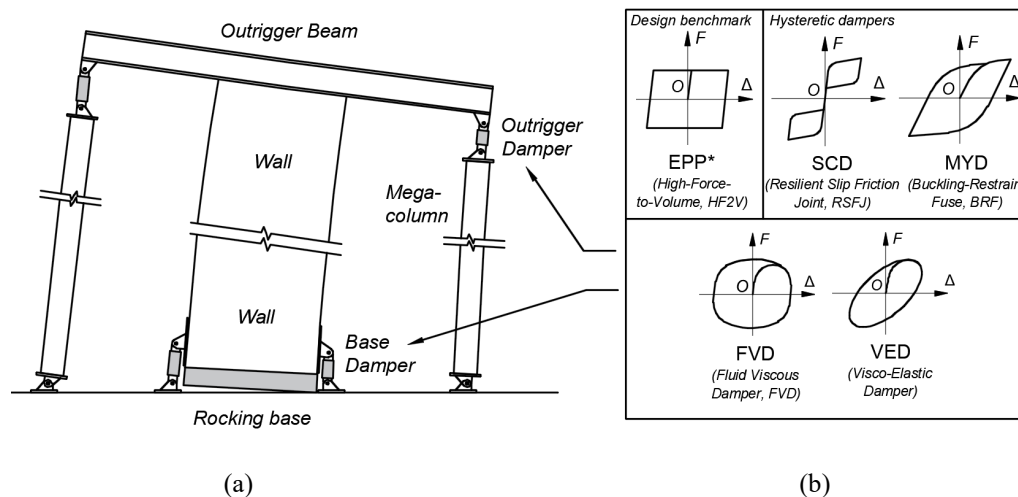


Figure 1.14. Controlled Outrigger Rocking Wall (CORW) system with different types of energy dissipators

1.8 Objectives and Research Scope

The objectives of this research are:

- 1) Evaluate the seismic performance of Controlled Outrigger Rocking Wall system designed using Equivalent Energy Design Procedure (EEDP). CORW system is a complex and innovative structural system. It was proposed recently with an assumed EPP type damper. Preliminary studies implicate excellent seismic performance. However, it is not clear how this system behaves with different damper configurations. This study aims to compare the difference in seismic performance between CORW systems with different damper combinations systematically.
- 2) Extend the EEDP procedure to select different dampers for CORW system. The proposed method allows designers to select among multiple dampers for CORW system to satisfy the design objectives. This research extends the damper selection for CORW system to viscous dampers, viscoelastic dampers, self-centering dampers and metallic yielding dampers.
- 3) Analytically study the dynamic response of CORW and compare the seismic performance of CORW with different damper configurations.
- 4) Experimentally validate the seismic performance of the CORW system using hybrid simulation. Hybrid simulation is especially powerful for evaluating performance of high-rise rocking structures, when large-scale shake-table test is not affordable nor applicable. This research aims to conduct hybrid simulation, where dampers are experimentally tested in laboratory and the remainder of the structure is numerically analyzed in computer, to validate the performance evaluation of CORW system.

1.9 Thesis Organization

- Chapter 2 presents the Equivalent Energy Design Procedure (EEDP) of Controlled Outrigger Rocking Wall (CORW) system. Design procedure for five different types of dampers including

viscous dampers, self-centering dampers and metallic yielding dampers for CORW system are presented and analyzed.

- Chapter 3 presents the design of a 100-meter-tall prototype CORW building located in Vancouver, Canada. Design parameters including structural drawings are presented, and detailed EEDP design parameters are presented. Realistic dampers are also selected and presented for the prototype.
- Chapter 4 presents the detailed development of the finite element model of CORW system, with rocking base, outrigger system, wall and different dampers. The modeling technique of the rocking base is validated by previous experimental data.
- Chapter 5 presents the results of nonlinear time history analyses of the CORW system with 25 damper combinations. The prototype combination is first compared with the design, showing that CORW with different dampers can be efficiently designed with the EEDP. The CORW system behaviors with different damper combinations are systematically.
- Chapter 6 presents the experimental program, including component tests and hybrid simulation. Testing facilities, instrumentations, test control and result are presented in this chapter. The result of the component test is used to calibrate the material models of dampers in Chapter 4. Hybrid simulation model, control strategy, hybrid simulation algorithm and result are presented. The result presented in the chapter validate the design and nonlinear time history analysis are accurate.

Chapter 2: Equivalent Energy Design Procedure of CORW System

2.1 Current Design Approach

The current force-based seismic design is easy to be adopted by engineers and building codes. However, it has several disadvantages:

- 1) It aims to achieve merely the collapse prevention (CP) performance objective under strong earthquakes. When designed for CP performance objective, the structural walls are expected to form plastic hinges at the base, where concrete crushes and reinforcing bars yield. This failure mode is sometimes not ideal. It makes repairing work extremely difficult and economically unfriendly. By using the force-based approach, the earthquake engineer cannot select other objectives such as immediate recover after medium earthquake.
- 2) It incorporates several empirical factors, which causes uncertainties in the performance of the designed structure to some extent uncertain. The structure may have some and unexpected damage.
- 3) It requires engineers to iteratively size the structural elements to satisfy both the strength and displacement requirements. For some complex structural systems, it make take a large number of iterations to finalize the structural elements.

To overcome the deficiencies, performance-based seismic design (PBSD) was proposed, offering choices of performance objectives, better performance prediction and reduced iterative procedure for designers. The performance objectives can be specified by the owner or determined by the earthquake engineer, based on the design requirements.

2.2 Equivalent Energy Design Procedure

Equivalent Energy Design Procedure (EEDP) is a novel design procedure utilizing energy balance concept with nonlinear plastic analysis to design structural systems. Detailed description of EEDP can be

found in Yang et al.'s work (T Y Yang et al., 2018). EEDP allows the engineers to determine different performance objectives for the structural system. Moreover, EEDP allows engineers to design forces and displacements at different shaking intensities without iterations.

As shown in Figure 2.1, the concept of EEDP is to equate the elastic energy (E_a) of an equivalent elastic single-degree-of-freedom (ELSDOF) system to the hysteretic energy ($E_s + E_h$) from an equivalent nonlinear single-degree-of-freedom (ENLSDOF) system.

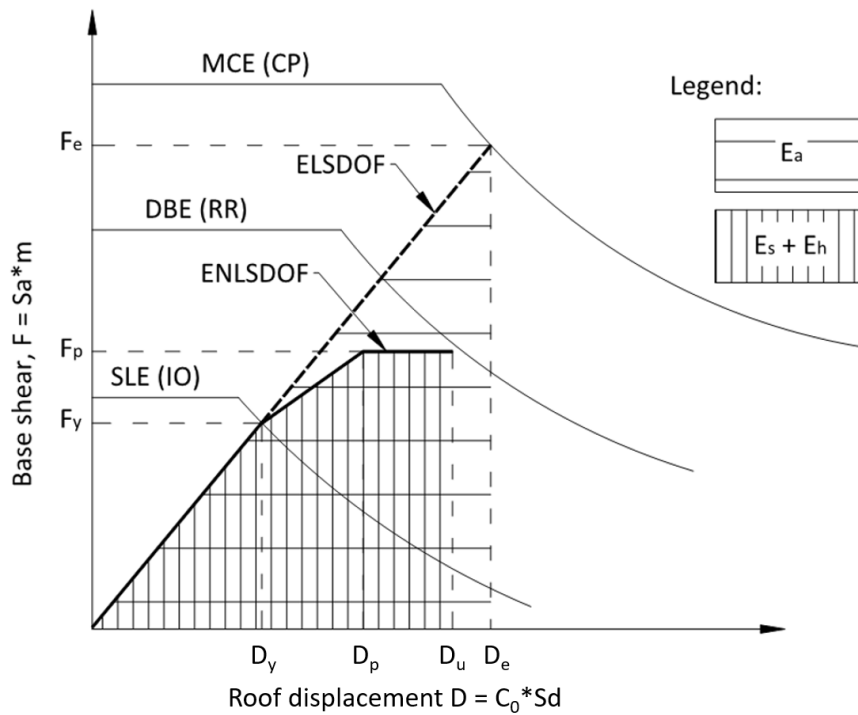


Figure 2.1. Concept of Equivalent Energy Design Procedure (EEDP)

2.3 Design of CORW System

Controlled Outrigger Rocking Wall (CORW) is designed to achieve different performance objectives at different earthquake intensities, as shown in Figure 2.2. At service level earthquake (SLE), the system is designed to remain elastic. At design base earthquake (DBE), the outrigger dampers yield and start to

dissipate energy. At maximum credible earthquake (MCE), the wall is expected to rock and the base dampers are expected to yield and dissipate energy.

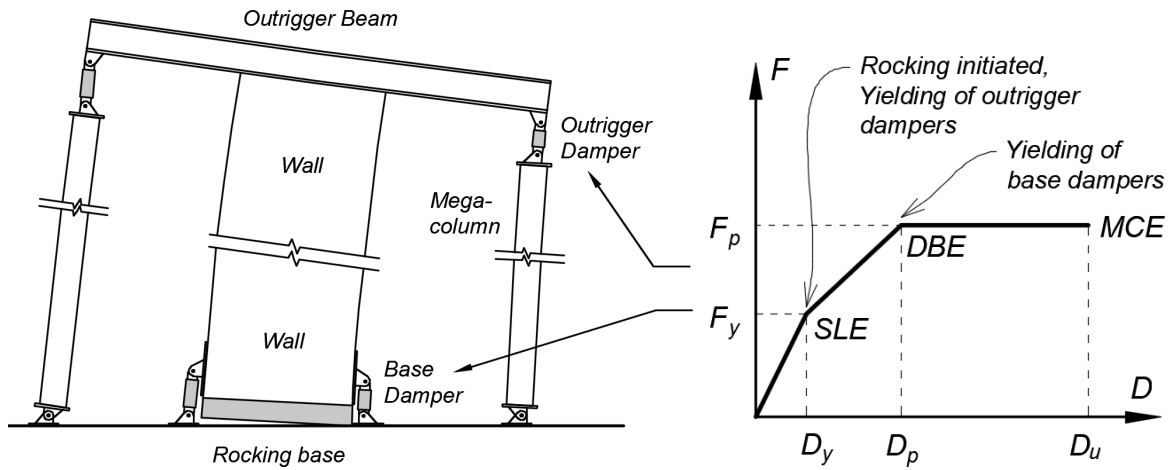


Figure 2.2. Concept and objectives of CORW system

A systematic design procedure for CORW was adopted from Tobber & Yang (2020). The design procedure is summarized as follows.

1) Selection of seismic hazard intensities and design objectives

Three hazard levels are mostly considered in practice of performance-based seismic design: Service Level Earthquake (SLE), Design Base Earthquake (DBE) and Maximum Credible Earthquake (MCE). At the SLE level intensity, the CORW is designed to remain elastic, hence the system can achieve immediate occupancy (IO) performance objective. At the design base earthquake (DBE) shaking intensity, the outrigger damper is designed to yield, while the concrete wall and the dampers at the base of the wall are designed to remain elastic. At the end of the earthquake, only the outrigger dampers need to be inspected and repaired or replaced as needed. This allows the CORW to achieve rapid return (RR) performance objective. At the maximum credible earthquake (MCE), the dampers at the base of the wall are designed to yield to provide the energy dissipation needed to allow the CORW to achieve collapse prevention (CP) performance objective. It should be note that the base dampers were designed to take less than 50% of the

overturning moment, hence CORW can be re-center after MCE shaking. Table 2.1 shows the design objectives selected for CORW at different shaking intensities.

Table 2.1. Design objectives, hazard and structural behaviors of CORW system

Performance Objective	Hazard level	Structural behavior
Immediate Occupancy (IO)	Service Level Earthquake (SLE)	The system remains elastic No element yield
Rapid Return (RR)	Design Base Earthquake (DBE)	Outrigger damper yield No structural damage
Collapse Prevention (CP)	Maximum Credible Earthquake (MCE)	Rocking initiated Base damper yield No structural damage

The performance objectives and the trilinear backbone curve of the CORW system are also shown in Figure 2.3.

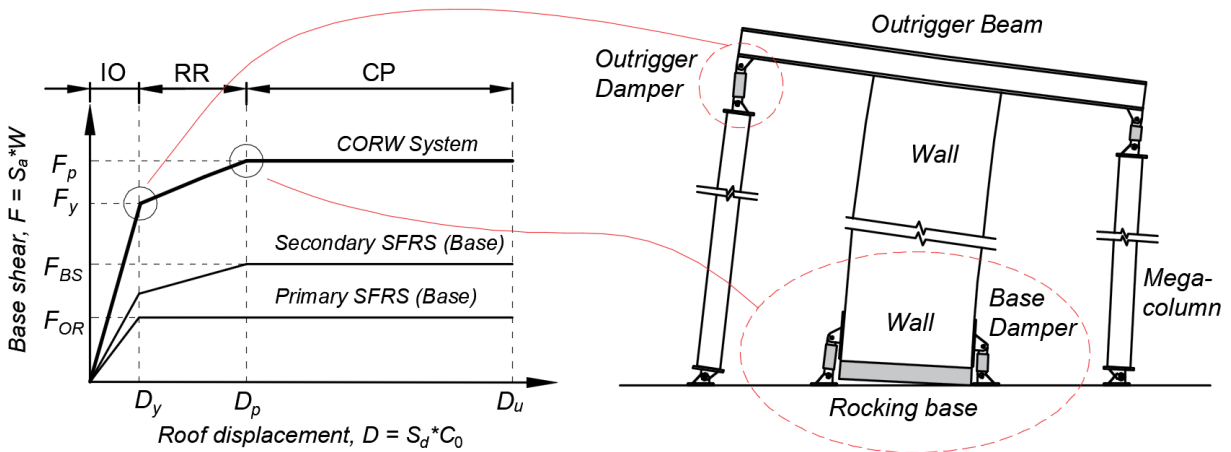


Figure 2.3. Trilinear backbone curve and performance objectives of CORW system

2) Determine the earthquake demand using modified capacity spectrum method

Once the shaking intensities have been identified, the earthquake demand can be plotted using the capacity spectrum method as shown in (2.3). The vertical axis represents the base shear of the CORW which can be approximated using Equation (2.1) proposed by Tobber et al. (20).

The selection of the shaking intensity may be specified by local building codes, owners or other stakeholders. EEDP uses the capacity spectrum method (Freeman, 1998) to plot the demand and capacity curves on the same figure. The MDOF roof displacements are estimated using the spectral displacement (S_d) multiplied by a C_0 factor. For the CORW system, C_0 can be estimated using

$$F = S_a * m * \beta_o \quad (2.1)$$

where m = mass of the building; S_a is elastic spectral acceleration; β_o is higher mode factor proposed by Tobber et al. (2018), shown in Equation (2.2), which is spectra shape dependent.

$$\beta_o = 0.04 \frac{S_a(T_2)}{S_a(T_1)} + 0.6 \quad (2.2)$$

where $S_a(T_1)$ and $S_a(T_2)$ is elastic spectral acceleration at the first and second mode, respectively.

The horizontal axis represents the roof displacement (D) of the CORW, which can be estimated using Equation (2.3).

$$D = C_0 S_d(T_1) \quad (2.3)$$

where $S_d(T_1)$ is the spectral displacement and the fundamental period (T_1) and C_0 is modification factor from the single degrees of freedom (SDOF) to the multiple degrees of freedom (MDOF) displacements as shown in Equation (2.4).

$$C_0 = 1.56 - \frac{0.05\alpha_f}{1.2 - \alpha_f} \quad (2.4)$$

where α_f , as shown in Equation (2.5), is a unitless parameter representative which relates the stiffness of the concrete wall to the stiffness of the outrigger.

$$\alpha_f = \frac{1}{\frac{E_c I_w}{k_o H_w} + 1} \quad (2.5)$$

where E_c = modulus of elasticity of concrete; I_w = moment of inertia of the section of the wall in the bending direction; H_w = total height of the wall; k_o is the stiffness of a rotational spring which represents the rotational stiffness provided by the outrigger beam, dampers and columns.

3) Select D_y and determine yielding base shear F_y at SLE level

EEDP assumes the energy dissipated by an equivalent linear single degree of freedom system (ELSDOF) will be the same as the equivalent nonlinear single degree of freedom system (ENLSDOF). At SLE level, both the NLSDOF and ELSDOF behaves linear. Hence, force-deformation response of the system will remain as a straight line from the origin to the intersection of the SLE shaking intensity. Engineers can select a yielding roof displacement (D_y), where the outrigger dampers yield. Based on the selected yield displacement, the yield base shear (F_y) can be obtained from the intersection of SLE level hazard spectrum and the selected yield roof displacement D_y . This procedure is shown in Figure 2.4.

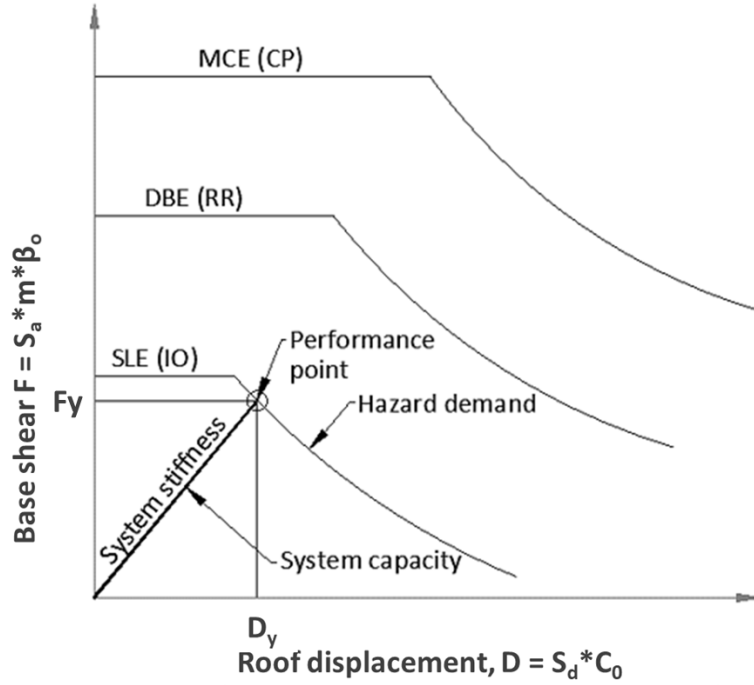


Figure 2.4. EEDP design for SLE level

4) Select D_p and determine plastic base shear F_p at DBE level

At DBE level, the base shear (F_p) and displacement (D_p) is determined by equating the elastic energy (ΔE_{E1}) to the nonlinear dynamic energy (ΔE_{ND1}), as shown in Equation (2.6).

$$F_p = 2 \frac{\Delta E_{E1}}{\gamma_a (D_p - D_y)} - F_y \quad (2.6)$$

where γ_a is the energy modification factor, which can relate the monotonic pushover energy dissipation to dynamic energy dissipation of the system, ΔE_{E1} is the incremental energy from the SLE to DBE shaking intensities, which can be calculated by Equation (2.7).

$$\Delta E_{E1} = \frac{m C_0 \beta_o}{2} (S_{a,DBE} - S_{a,SLE}) (S_{d,DBE} - S_{d,SLE}) \quad (2.7)$$

where $S_{a,DBE}$ and $S_{a,SLE}$ are the spectral accelerations from the ELSDOF for the DBE and SLE hazards, respectively; $S_{d,DBE}$ and $S_{d,SLE}$ are the spectral displacements from the ELSDOF under DBE and SLE hazards, respectively.

5) Calculate D_u and calculate ultimate base shear F_u at MCE level

At MCE level, the ultimate roof displacement can be calculated by Equation (2.8).

$$D_u = \frac{\Delta E_{E2}}{\gamma_b F_p} + D_p \quad (2.8)$$

where γ_b is energy modification factor to relate the monotonic pushover energy dissipation of the system to the incremental energy dissipation of the system when hazard changes from DBE to MCE level; ΔE_{E2} = incremental energy from the SLE to DBE hazard level, which can be calculated using Equation (2.9).

$$\Delta E_{E2} = \frac{C_0}{2} (F_{MCE} + F_{DBE}) (S_{d,MCE} - S_{d,DBE}) \quad (2.9)$$

where F_{MCE} is the elastic base shear at MCE hazard and $S_{d,MCE}$ is the spectral displacement at the MCE hazard.

6) Distribute MCE level base shear F_u to primary and secondary systems

Once the tri-linear backbone curve has been defined, the next step in EEDP is to determine the design force for the primary system (outrigger) and the secondary system (controlled rocking base). In the original derivation of EEDP, the primary and secondary systems are assumed to act in parallel. This results in the tri-linear system backbone that can be separated into two bilinear backbones, shown in Figure 3a. However, the CORW system is unique in that the primary and secondary systems act in series with the elastic wall. As a result, the primary system (outrigger) is a bilinear backbone, while the secondary system (controlled rocking base) has a tri-linear backbone.

Tobber et al. (2018) demonstrate that the portion of load resisted by the primary system and secondary systems can be calculated using Equations (2.10) and (2.11), respectively.

$$F_{PR} = \frac{3}{8} F_y \alpha_f \quad (2.10)$$

$$F_{SC} = F_p - F_{PR} \quad (2.11)$$

7) Preliminary design of the dampers

Once the forces in the primary and secondary system have been defined, the forces in the outrigger damper ($f_{u,OR}$) and base damper ($f_{u,BS}$) can be calculated using Equations (2.12) and (2.13), respectively.

$$f_{u,OR} = \frac{F_{PR} \sum_{i=1}^n (Q_{x_i} h_i)}{L_{OR}} \quad (2.12)$$

$$f_{u,BS} = \frac{F_{SE} \sum_{i=1}^n (Q_{x_i} h_i) - P_g (L_w/2)}{L_d} \quad (2.13)$$

where Q_x is the inverse triangular distributed load on the system, which can be expressed in Equation (2.14).

$$Q_x = \frac{w_x h_x}{\sum_{i=1}^x w_i h_i} \quad (2.14)$$

where w is the weight at each story, h is the story height, L_d , L_{OR} , and L_w are centerline distance between base dampers, centerline distance between outrigger dampers and depth of section of the wall, respectively.

Figure 2.5 shows the schematic view of the primary and secondary system within the CORW system.

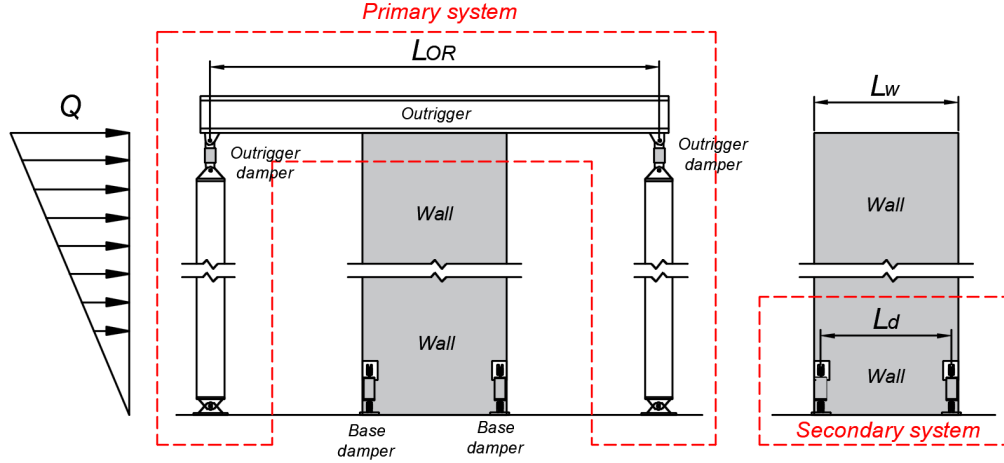


Figure 2.5. Schematic view of primary and secondary system

The ultimate plastic displacement demand for outrigger and base dampers ($d_{u,OR}$ and $d_{u,BS}$) can be calculated by Equation (2.15) and (2.16), respectively.

$$d_{u,BS} = \frac{D_u - D_p}{H_w} L_w \quad (2.15)$$

$$d_{u,OR} = \frac{L_{OR} C_\theta}{2} \left(\frac{D_u - D_p}{H_w} + \frac{F_p - F_y}{12E_c I_w} \right) \quad (2.16)$$

where by C_θ is a higher mode factor developed by Tobber et al. (2018). It should be noted that the rotation of the outrigger is amplified during dynamic response. In a cantilever beam, with a fixed base, dynamic roof rotation can be over 2.5 times the rotation under static loads. The energy dissipating outrigger reduces these amplifications, as such, for this study, $C_\theta = 1.8$, is used. Detailed derivation of C_θ is shown in Tobber et al.

Equation (2.17) and (2.18) shows the effective stiffness for the primary and secondary systems, respectively.

$$K_{eff,PR} = \frac{F_{PR}}{D_u} \quad (2.17)$$

$$K_{eff,SE} = \frac{F_{SE}}{D_u} \quad (2.18)$$

Similarly, the effective period can be determined for the primary and secondary systems using Equation (2.19) and (2.20), respectively.

$$T_{eff,PR} = 2\pi \sqrt{\frac{K_{eff,PR}}{m}} = 2\pi \sqrt{\frac{F_{PR}}{D_u m}} \quad (2.19)$$

$$T_{eff,SE} = 2\pi \sqrt{\frac{K_{eff,SE}}{m}} = 2\pi \sqrt{\frac{F_{SE}}{D_u m}} \quad (2.20)$$

where m is the total mass of the CORW system.

The energy dissipation capacity of the damper is determined. The hysteretic energy dissipation in one full cycle of displacement can be calculated using Equation (2.21), which is the area enclosed by the EPP loop.

$$W_{d,EPP} = 4f_u d_u - \frac{4f_u^2}{k} \quad (2.21)$$

where k is the initial stiffness of the EPP damper.

8) Capacity design of the wall

With the dampers designed, the structural walls, outrigger and foundation were capacity designed such they remain elastic under the maximum damper yielding forces.

2.4 Design of Energy Dissipators

Previous studies on the CORW system have assumed that the dampers have a Elastic-Perfectly-Plastic (EPP) hysteresis. There are several different types of dampers readily available to the industry which do

not follow EPP behavior. Each damper type has its own hysteretic and dynamic properties. In this study, robust design method is proposed for four types of dampers:

- 1) Self-centering damper (SCD);
- 2) Metallic yielding damper (MYD);
- 3) Fluid viscous damper (FVD);
- 4) Viscoelastic damper (VED);

For simplicity of design, minimal change to the original EEDP design procedure is used to design the dampers. Hence, each damper is designed to produce a trilinear curve that follows the EEDP designed backbone, i.e., the alternative damper should produce the designed damper force (f_u) at the designed maximum damper displacement (d_u). The design of each damper type is described in the subsequent sections.

2.4.1 Self-centering Damper

Self-centering dampers (SCD) are popular because of their flag-shaped hysteretic behavior which results in no residual deformations after strong earthquake shaking. The force in generic SCD can be calculated using Equation (2.22).

$$f_{u,SCD} = f_{act} + k_2(d_u - f_{act}/k_1) \quad (2.22)$$

where $f_{u,SCD}$ is the damper force of SCD, which needs to meet force demand f_u , f_{act} is the activation force when the damper starts to yield and dissipate energy. The flag-shape control parameter β controls the shape of the hysteretic loop of SCD. It is recommended to use as large β value as practical, to obtain optimum energy dissipation.

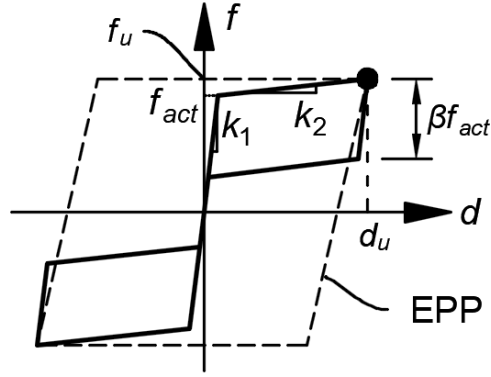


Figure 2.6. Typical hysteresis of self-centering damper (SCD)

2.4.2 Metallic Yielding Damper

Metallic yielding dampers (MYD) dissipate the earthquake energy through yielding of metals. Commonly used MYDs include Buckling-Restrained Brace (BRB) (Liu & Palermo, 2020), honeycomb steel damper (Yang et al., 2019), welded wide flange fuse (WWFF) (Yang et al., 2018). MYD are arguably some of the most popular hysteretic dampers due to their stable hysteretic behavior and relatively low manufacturing costs. Figure 2.7 shows the typical hysteretic behavior of generic idealized MYD.

Due to the variation of properties of different MYDs, it is hard to provide a formula that fits all. Hence, a simplified effective bilinear hysteretic model can be established for a generic description of the hysteresis of MYD, with initial stiffness k , hardening ratio b and effective yielding force f_{ye} . With the simplified bilinear model, the force produced by MYD can be calculated using Equation (2.23).

$$f_{u,MYD} = f_{ye} + bk(d_u - f_{ye}/k) \quad (2.23)$$

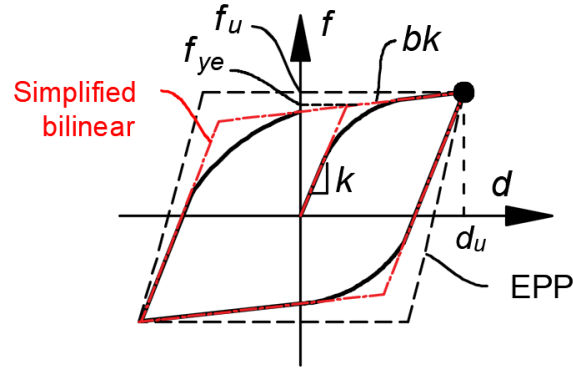


Figure 2.7. Typical hysteresis of metallic yielding damper (MYD)

2.4.3 Fluid Viscous Damper

Fluid viscous dampers (FVD) are frequently used as energy dissipation devices. FVD work by forcing viscous fluid and can reduce structural displacement and acceleration responses by providing supplemental viscous damping to the structure. FVD have been implemented to rocking wall system (Yahya, 2000) and outrigger system (Smith & Willford, 2007) in previous research. The ultimate force in a typical FVD ($f_{u,FVD}$) can be expressed in Equation (2.24).

$$f_{u,FVD} = C|v_u|^\alpha \quad (2.24)$$

where C and α are the damping coefficient and exponent of the damper, respectively, and v_u is the maximum relative velocity experienced by the viscous damper. Figure 2.8 shows the typical force-deformation relationship of FVD.

FVD is made equivalent to the EPP damper by dissipating similar amount of energy. The energy dissipated by the FVD can be calculated using Equation (2.25) (Seleemah & Constantinou, 1997)

$$W_{d,FVD} = W_{d,EPP} = \lambda C d_u^{1+\alpha} \left(\frac{2\pi}{T_{eff}} \right)^\alpha \quad (2.25)$$

where C is the damping coefficient of the damper; d_u is the deformation demand for the damper, T_{eff} is the effective period of either primary or secondary system, determined by Equation (2.19) and (2.20) in Step 8 of the EEDP design; λ is a constant related to damping exponent of viscous damper, which is either provided by damper manufacturer or Equation (2.26).

$$\lambda = 4 \cdot 2^\alpha \frac{\Gamma^2(1 + \alpha/2)}{\Gamma(2 + \alpha)} \quad (2.26)$$

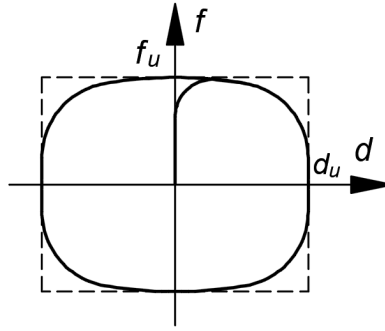


Figure 2.8. Typical force-deformation relation of fluid viscous damper (FVD)

2.4.4 Viscoelastic Damper

Viscous elastic damper (VED) is similar to FVD, except the damper has some stiffness. The ultimate force in a typical VED can be expressed in Equation (2.27).

$$f_{u,VED} = Cv + kd_u \quad (2.27)$$

where k is the added stiffness and d_u is the designed displacement of damper.

Unlike the FVD, when the VED reaches the maximum deformation, the force in VED is not zero, while the FVD is zero. In this study, solid type of viscous elastic damper is used, where high-damping solid

polymer layers are deformed in shear under input excitation. For this type of damper, C and k values are coupled. Both of them can be determined by size and type of the damping material (Constantin Christopoulos & Montgomery, 2013) using Equation (2.28) and (2.29).

$$k = G_E A / h \quad (2.28)$$

$$C = G_C A / h \quad (2.29)$$

where G_E and G_C are the shear storage modulus and the shear loss modulus of the damping material, respectively; A is the total bonded area and h is the thickness of each damping material layer.

The VED is made equivalent to the EPP damper by selecting and sizing damping material (G_E , G_C , A and h) such that it dissipates similar amount of energy with EPP damper. Equation (2.25) can still be used to calculate the energy dissipation for VED ($W_{d,VED}$). Table 3.6 shows the designed values for VED used in this study.

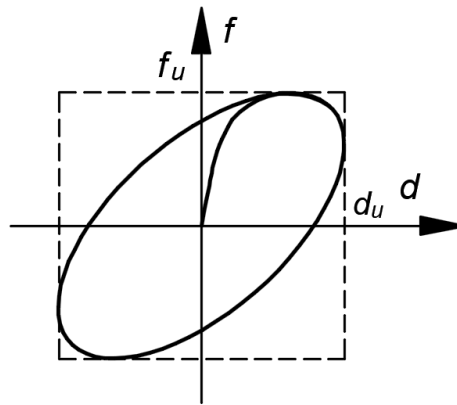


Figure 2.9. Typical hysteresis of viscous elastic damper (VED)

The use of FVD and VED may introduce unexpectedly high damping force. Since they are velocity dependent, and the in-service velocity of these dampers cannot be easily predicted. The high damping force increases the force in the structural wall and may cause damage. To prevent wall damage, α value is often

controlled within a relatively lower range (0.1~0.5) to limit damping force. Alternatively, a force-limiting device in the damper may also be useful (Smith & Willford, 2007). This device is often an optional accessory offered by damper manufacturer, such as pressure release valve.

Chapter 3: Prototype CORW Building

3.1 Introduction to Prototype Building

A 100-meter tall, 24-story office CORW as shown in Figure 5 is adopted in this study. The geometry of the prototype building was selected in consultation with local practicing engineers and is based on typical wall layouts for buildings located in the West Coast of Canada. Figure 3.1a shows the elevation view of the prototype building, and Figure 3.1b shows the typical floor plan. The site has an assumed shear wave velocity, V_{S30} , of 450 m/sec. The design spectral acceleration values are taken from the 2015 National Building Code of Canada (NBCC, 2015). The building is designed for SLE, DBE and MCE hazards representative of the 50% probability of exceedance in 30 years, and 10% and 2% probability of exceedance in 50 years, respectively.

The floor plan is assumed to be 27.2 m x 27.2 m. The floor height is assumed to be 3.96 m per floor. The structure is assumed to have no basement below grade. Two CORW systems are placed at the perimeter of the building in both the N-S and E-W directions. Four mega columns, each with a dimension of 1250 mm x 1250 mm, are placed at the ends of the outriggers. The centerline distance between mega columns is 25.76 m. The wall is assumed to have a dimension of 10100 mm x 750 mm. The cross section of the wall is constant for all floors. The specified concrete compressive strength (f_c') is 45 MPa, and the designed yielding stress of steel reinforcements is 400 MPa for all concrete components. The outrigger truss is assumed to have a moment of inertia of 1 m^4 . The gravity load and seismic mass are 2024 kN and 727 tonne for each floor, respectively. Previous studies have shown that minimal interaction between the rocking wall and the gravity system can be achieved through isolated wall-to-floor connection (Richard Henry et al., 2012b).

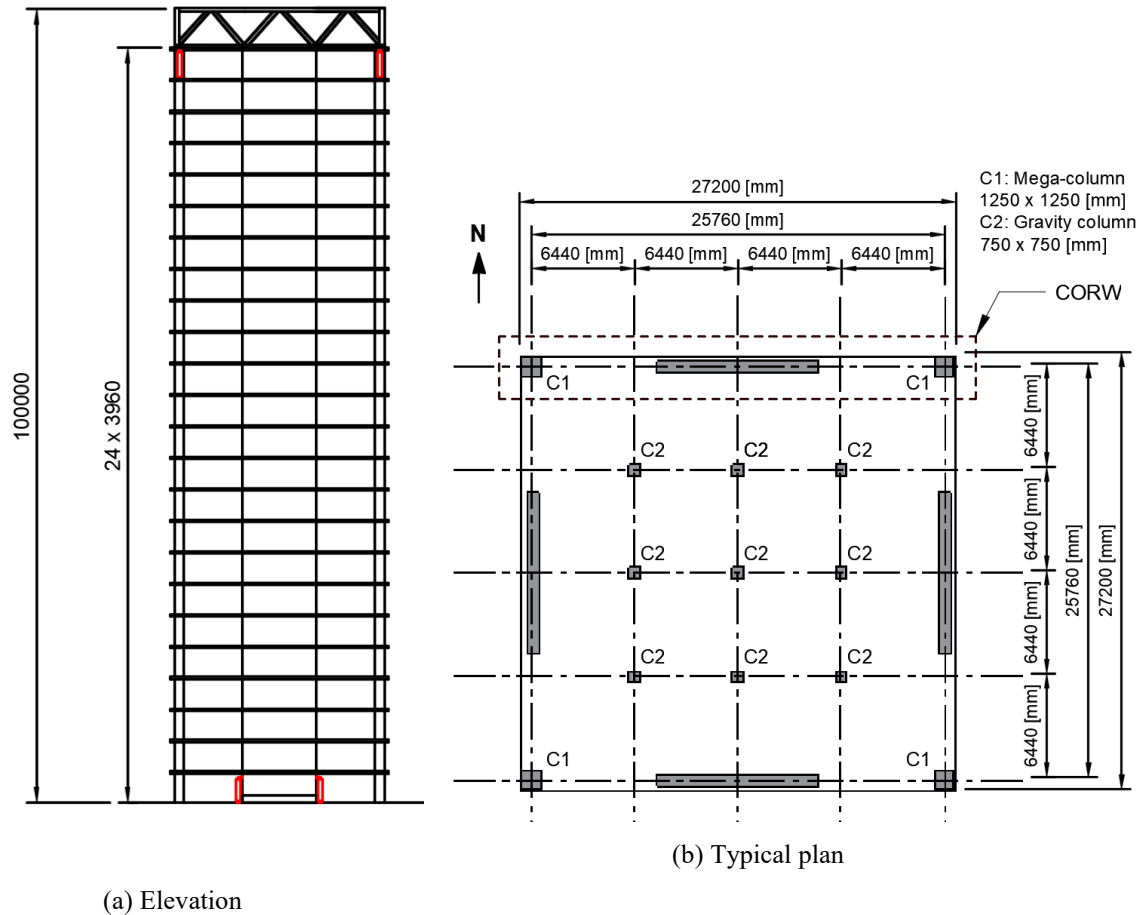


Figure 3.1. Geometry of CORW prototype building

3.2 Design of Prototype Building

The prototype building was designed using the procedure described in Chapter 2. The roof displacement values at the SLE (D_y) and the DBE (D_p) hazards were selected to be 45 and 170 mm, respectively. Using the EEDP procedure, the corresponding displacement at the MCE level hazard was solved to be 450 mm. The resulting yield shear (F_y) and ultimate shear (F_p) are 2180 kN and 5340 kN, respectively. Table 3.1 summarizes all the design parameter for the prototype CORW building.

Table 3.1. Summarize of design parameters of the prototype CORW

Hazard level	SLE	DBE	MCE
Base shear	$F_y = 2180 \text{ kN}$	$F_p = 5340 \text{ kN}$	
Displacement	$D_y = 45 \text{ mm}$	$D_p = 170 \text{ mm}$	$D_u = 450 \text{ mm}$

The prototype design utilized HF2V device (Geoffrey William Rodgers, 2009; G W Rodgers et al., 2008) with an assumed Elastic-Perfectly-Plastic (EPP) hysteresis. HF2V typically consists of a bulged central shaft surrounded by lead encased in a cylinder. Albeit that HF2V device is slightly velocity dependent, it produces a relatively constant force upon yielding, and the damping exponent is around 0.10~0.12(G W Rodgers et al., 2017). Previous research(G W Rodgers et al., 2008) on dynamic response of HF2V indicate that HF2V device can be designed as hysteretic damper. The work by Tobber et al. presented the ultimate displacement and the yielding force of the device, as shown in Table 3.2.

Table 3.2. Summarize of prototype damper design parameters

Location	Design parameter	Design value
Outrigger	Damper force	$f_{u,OR} = 2200 \text{ kN}$
	Damper deformation	$d_{u,OR} = 80 \text{ mm}$
Base	Damper force	$f_{u,BS} = 6800 \text{ kN}$
	Damper deformation	$d_{u,BS} = 30 \text{ mm}$

3.3 Selection of Energy dissipators

3.3.1 Resilient Slip Friction Joint

In this study, Resilient Slip Friction Joint (RSFJ) developed by Ashkan Hashemi et al. (2018) is selected as the SCD, as shown in Figure 3.2. RSFJ utilizes specially grooved steel cap plates with slotted holes. The slotted cap plates are post-tensioned by high-strength post-tensioned bolts and special springs. The post-tensioning can provide the device with adequate amount of friction. RSFJ can also re-center by the post-tensioned rods and the curved plate contact.

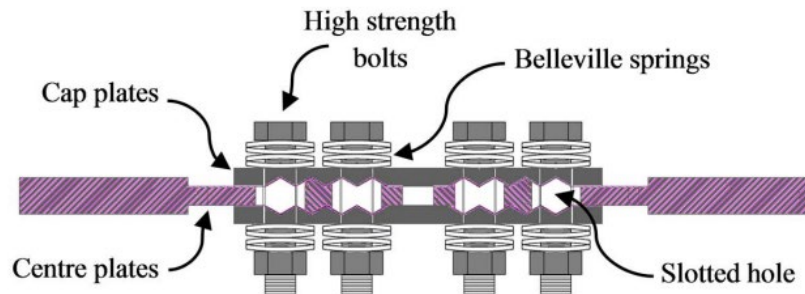


Figure 3.2. Resilient Slip Friction Joint (A Hashemi et al., 2018)

In this study, RSFJ was designed such that it meets the force demand (f_u) at the designed displacement (d_u). The initial stiffness (k_1), post-activation stiffness (k_2) and flag-shape control parameter β are adopted from the device. It is recommended to choose the lowest available post-activation stiffness (k_2) and highest available flag-shape control parameter (β) to produce a hysteretic loop as close as the benchmark EPP device. The parameters of the selected RSFJ are shown in generic self-centering formulation in Figure 2.1.

Table 3.3. Design parameters of self-centering damper (SCD)

Design parameters (outrigger, lumped)	Design parameters (base, lumped)
$k_1 = 2800 \text{ kN/mm}$ $k_2 = 9.5 \text{ kN/mm}$ $f_{act} = 1430 \text{ kN}$ $\beta = 0.84$	$k_1 = 11000 \text{ kN/mm}$ $k_2 = 37 \text{ kN/mm}$ $f_{act} = 5610 \text{ kN}$ $\beta = 0.84$

3.3.2 Filler-free Buckling Restraint Fuse

In this study, Filler-free Buckling Restraint Fuse is used for MYD. Characteristics of FFBRF have been studied in detail by Liu & Palermo (2020). FFBRF is designed and tested such that it produces the similar amount of ultimate force $f_{u,MYD}$ to the designed force f_u at the design ultimate deformation d_u . To achieve that, a section area was first selected. Then, k , f_{ye} and b values were obtained from the damper provider to estimate force $f_{u,MYD}$. By matching $f_{u,MYD}$ and f_u , the device is selected and the parameters are obtained, as shown in Table 3.4.

Table 3.4. Design parameters of filler-free buckling restraint fuse (FFBRF)

Design parameters (outrigger, lumped)	Design parameters (base, lumped)
$k = 935 \text{ kN/mm}$ $f_{ye} = 5750 \text{ kN}$ $b = 0.015$	$k = 470 \text{ kN/mm}$ $f_{ye} = 1360 \text{ kN}$ $b = 0.015$

3.3.3 Fluid Viscous Damper

In this study, Fluid Viscous Damper were selected such that it produces the same amount of full-cycle energy as EPP damper. The C and α values were determined by energy using datasheet provided by damper manufacturer. Table 3.5 shows the damper parameters of the designed FVD.

Table 3.5. Parameters of fluid viscous damper (FVD)

Design parameters (outrigger, lumped)	Design parameters (base, lumped)
$C = 400 \text{ kN(s/mm)}^{0.29}$ $\alpha = 0.29$	$C = 2000 \text{ kN(s/mm)}^{0.29}$ $\alpha = 0.29$

3.3.4 Viscoelastic Damper

In this study, Solid viscoelastic damper is used. Table 3.6 shows the parameters of the designed VED.

Table 3.6. Parameters of viscous elastic damper (VED)

Design parameters (outrigger, lumped)	Design parameters (base, lumped)
$C = 6.4 \text{ kN-s/mm}$ $k = 15 \text{ kN/mm}$	$C = 52 \text{ kN-s/mm}$ $k = 125 \text{ kN/mm}$

3.4 Controlled Rocking Base Hinge

Controlled Rocking Base Hinge (CRBH) plays an important role in controlling structural damage. As shown in Figure 3.3, CRBH often includes base armoring, base dampers, bedding layer and an optional

shear key. Local concrete damage at conventional unconfined rocking base hinge was reported in previous experimental studies (Restrepo & Rahman, 2007b). During rocking, gravity load is concentrated at one side of the wall (rocking toe). The concentrated compressive stress sometimes causes local concrete damage. Although this local damage contributes little to global behavior, it creates difficulties in re-centering and repairing. To prevent the local damage, base armoring is designed to confine the rocking toes. A well-confined rocking toe should be damage-free under designed earthquake.

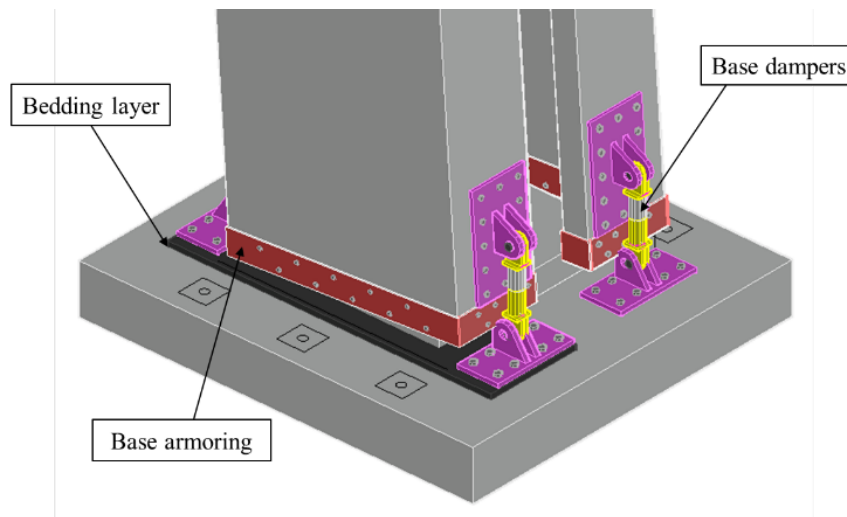


Figure 3.3. Schematic view of Controlled Rocking Base Hinge (CRBH) for tall resilient wall systems

A high strength bedding layer is necessary for the rocking base hinge, since it provides a flat, strong and relatively rigid surface for rocking, and makes the rocking behavior predictable. Previous study (R. Henry, 2011) on rocking walls without bedding layers or with weak bedding layers reported severe damage at the underneath contacting surface, which led to undesirable force-deformation response and self-centering behavior. Thus, high-strength grout bedding layer, or embedded steel, is recommended in engineering practice.

Sliding shear happens when the friction force between the base of the wall and the foundation is not enough to resist base shear. Sliding shear should always be checked when designing details of the CRBH.

Nevertheless, sliding shear is not difficult to resolve for tall and slender walls, since moment usually dominates the internal forces. This idea is shown in Figure 3.4.

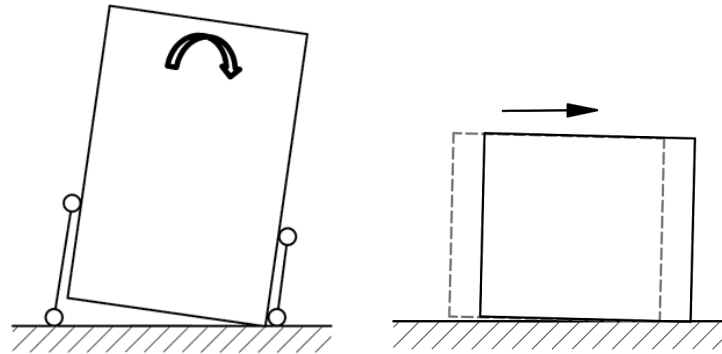


Figure 3.4. Rocking and sliding shear

Post-tensioning is often required for low-rise rocking wall systems, as mentioned in previous research. However, it is not always required for high-rise buildings. During rocking, large amount of gravity load in high-rise building could generate relatively larger restoring moment, which helps the structure to re-center. Some types of base dampers could also provide restoring moments. If the total generated restoring moment is large enough, no post-tensioning is needed for the structural system.

In previous experimental studies and earthquake observations (Restrepo & Rahman, 2007b), local concrete damage at conventional unconfined rocking base is reported. During rocking, the uplifts occurs at one side of the wall, and contact between the rocking wall and foundation is limited to the opposite side of the wall (rocking toe), which means that all gravity are loaded at the rocking toe. The rocking toes are under concentrated compressive stresses, often causing local concrete damage, where concrete crushes and reinforcing bars buckle. With the local damage, the bottom of the wall is no longer flat and thus the resilience and self-centering behavior are limited. To prevent local damage in rocking toes, the base armoring is designed to confine the rocking toes. A well-confined rocking toe is believed to be damage-free during rocking.

Chapter 4: Numerical Modeling of CORW System

Chapter 2 introduced the detailed design procedure of Controlled Outrigger Rocking Wall (CORW), and a robust procedure to determine five types of energy dissipation devices for CORW. Chapter 3 presented a 100-meter-high prototype building selected for this study, where geometry, design parameters and assumptions were included. This chapter develops a detailed finite element model for the prototype CORW building, including five types of energy dissipation devices.

Section 4.1 introduces the modeling technique of rocking base, outrigger system, and structural wall. Section 4.2 validates the modeling techniques and assumptions based on experimental results. Section 4.3 presents details about modeling different types of dampers, including EPP, SCD, MYD, FVD and VED. Section 4.4 presents the selection of ground motion and scaling.

4.1 Modeling of CORW Prototype

Due to the symmetry nature of the building, only the response of the benchmark building in the E-W direction is presented. Only one span of outrigger wall is considered.

Multiple numerical simulation models were developed in this study. As shown in Table 4.1, 5 types of dampers are considered and structural systems with 25 combinations of the 5 dampers, either at outrigger or base, are investigated. For simplicity, each combination is denoted as ‘O-B’, where O is the outrigger damper type and B is the base damper type.

Table 4.1. Numerical model matrix for prototype CORW system

Combination No.	Numerical model name	Outrigger damper type (OR)	Base damper Type (BS)
1	SCD-SCD	SCD	SCD
2	MYD-SCD	MYD	SCD
3	EPP-SCD	EPP	SCD
4	FVD-SCD	FVD	SCD
5	VED-SCD	VED	SCD
6	SCD-MYD	SCD	MYD
7	MYD-MYD	MYD	MYD
8	EPP-MYD	EPP	MYD
9	FVD-MYD	FVD	MYD
10	VED-MYD	VED	MYD
11	SCD-EPP	SCD	EPP
12	MYD-EPP	MYD	EPP
13	EPP-EPP	EPP	EPP
14	FVD-EPP	FVD	EPP
15	VED-EPP	VED	EPP
16	SCD-FVD	SCD	FVD
17	MYD-FVD	MYD	FVD
18	EPP-FVD	EPP	FVD
19	FVD-FVD	FVD	FVD
20	VED-FVD	VED	FVD
21	SCD-VED	SCD	VED
22	MYD-VED	MYD	VED
23	EPP-VED	EPP	VED
24	FVD-VED	FVD	VED
25	VED-VED	VED	VED

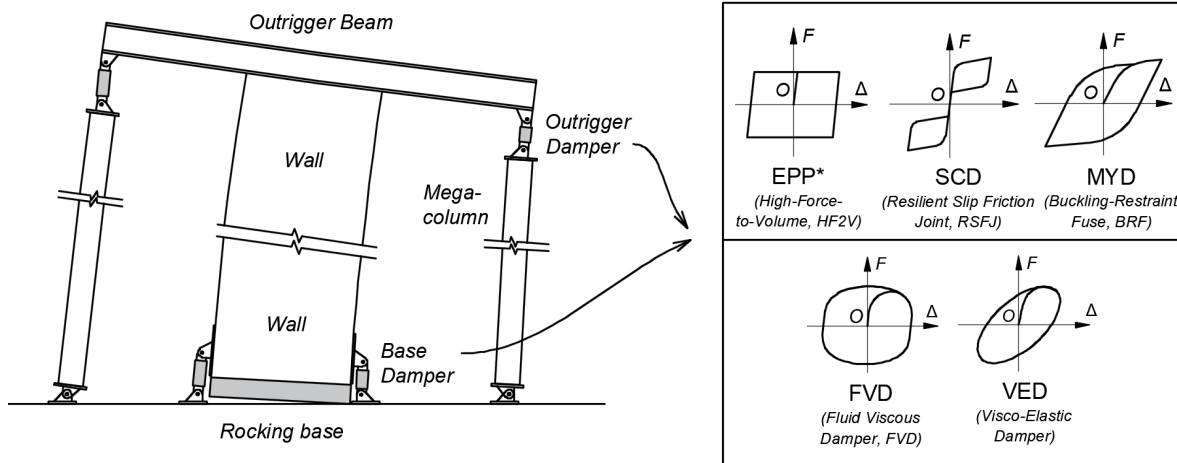


Figure 4.1. Schematic view of CORW system with different dampers

4.1.1 Modeling of Rocking Base

Three modeling techniques were mostly used in previous research to model the rocking base of rocking walls: fiber model, lumped plasticity model, and multi-spring model.

The fiber model is proposed and validated by F. J. Perez et al. (2007), where a displacement fiber-based beam-column element with zero-tension concrete material was modeled at the bottom of the wall. This modeling approach was first used to model jointed unbonded precast concrete wall system. Detailed comparison with experimental results shown excellent match. This modeling technique is schematically shown in Figure 4.2a.

The lumped plasticity model is proposed by Nazari et al. (2017), which assumes a rotational spring with flag-shaped self-centering material at the bottom of the wall. For the lack of section considerations, to use lumped plasticity model for wall section, calibration is needed to determine the parameters for the aforementioned self-centering material, and the accuracy of the lumped plasticity model is limited since it contains little section detail. This modeling technique is shown schematically in Figure 4.2b.

Multi-spring model is a less simplified version of the fiber model. As shown in Figure 4.2b, the multi-spring model consists of a number of parallel springs, all connected to the bottom node of the wall with

relatively rigid beam-column element or a rigid link constraint. The multi-spring model was validated by Watkins et al. (2014) based on shake-table test results. For each spring at the base, three parameters are often required: material, section area, and length. In their research, the material for the base springs is modified Concrete07 (from OpenSees), a compression-only concrete material adjusted to produce zero stress in tension. The section area of a spring was set as tributary section area of the wall at the location of the spring. The spring length could be determined using the equation for the H_{er} , proposed by F. J. Perez et al. (2007). Multi-spring model is computationally cheaper than the fiber model, while retaining the accuracy of the fiber model.

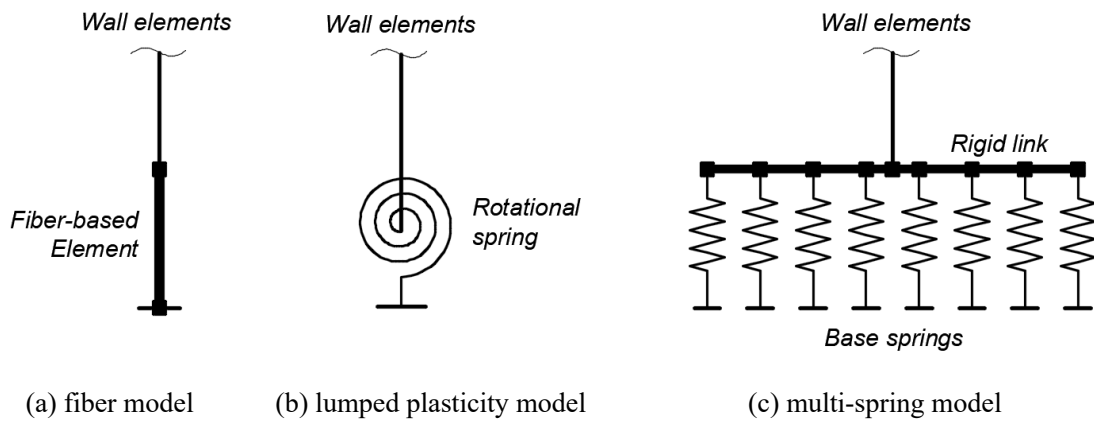


Figure 4.2. Modeling of rocking base

Multi-spring model (Watkins et al., 2014) is adopted here for the rocking base of the wall. The modeling of the rocking base of CORW uses 16 parallel springs, all fixed to the bottom of the wall with rigid beam element. For each spring at the base, three parameters are required: material, section area, and length. The material for the base springs is Concrete01, a simplified compression-only material producing zero stress under positive strain. The section area of a spring equals to the tributary section area of wall at the location of the spring. The spring length could be determined using the equation for the H_{er} , the height of the base

be taken by outrigger dampers, as well as the mega-columns. To numerically cancel the initial gravity load, the mega-columns are modeled together with a spring with a compressive initial strain. Upon the initial strain in mega-columns imposed at the first step of analysis, the mega-column deforms and release stress coming from gravity. The analysis result shows that all the gravity load goes to the wall element in the first step, and thus the initial load in outrigger damper and mega-column is numerically cancelled.

4.1.3 Modeling of Structural Wall

For simplicity, the wall is modeled using 24 elastic beam-column elements, with masses and gravity loads assigned at each upper node of the elements. Previous studies showed that the local nonlinear behavior due to rocking is often limited at a small portion of the rocking toes, and has little influence on structural behaviors (Richard Henry et al., 2012a). The outrigger dampers and base dampers are modeled using zero-length and truss elements, respectively.

4.2 Validation of Numerical Modeling of Rocking Base Hinge

To validate the above modeling techniques, numerical model with multi-spring rocking base and elastic wall elements were also created based on the specimen TW2 of the cyclic experimental tests conducted by Perez et al. (F. J. Perez, 2004; F. J. Perez et al., 2007). The numerical model for validation was shown in Figure 4.4. The resulted base-shear-lateral-drift relationship shown in Figure 4.6 indicate that the modeling technique for the rocking base, and the elastic assumption of wall elements were valid. Figure 4.7 shows the stress and deformation of the base springs during rocking, indicating that the multi-spring model is able to simulate section-level stress and strain distribution.

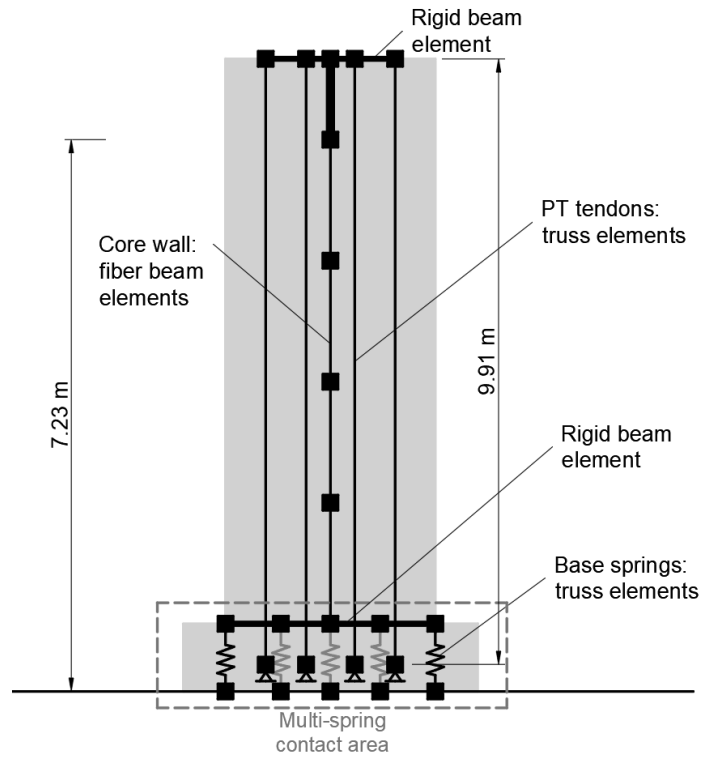


Figure 4.4. Schematic view of numerical model for validating rocking base and wall elements modeling

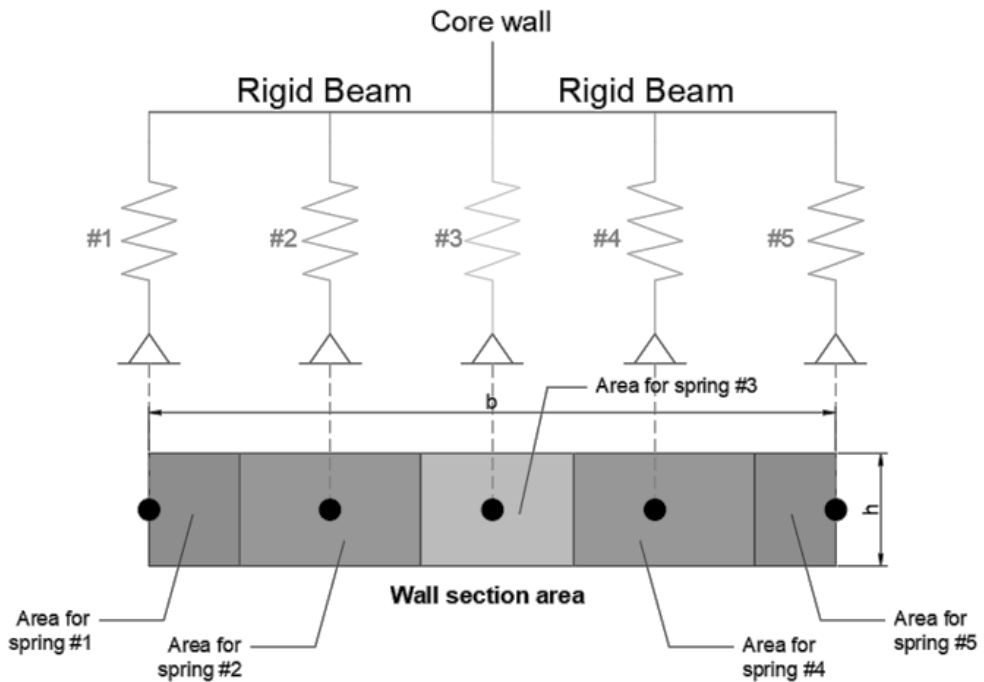


Figure 4.5. Schematic view of modeling of rocking base for validation

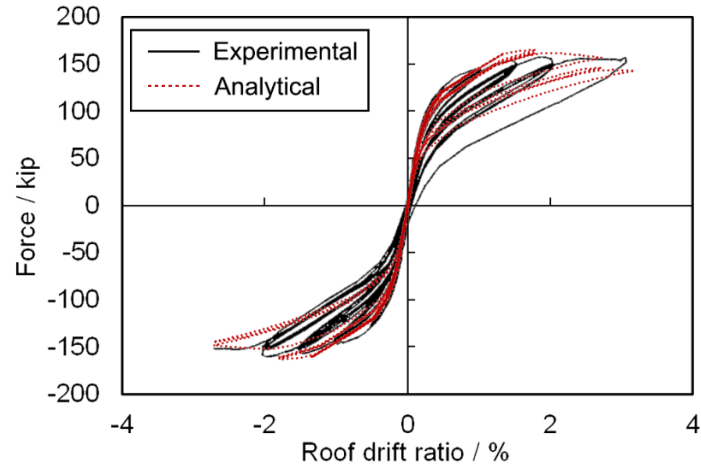


Figure 4.6. Validation of numerical modeling techniques for rocking base and wall elements

(Perez, 2004)

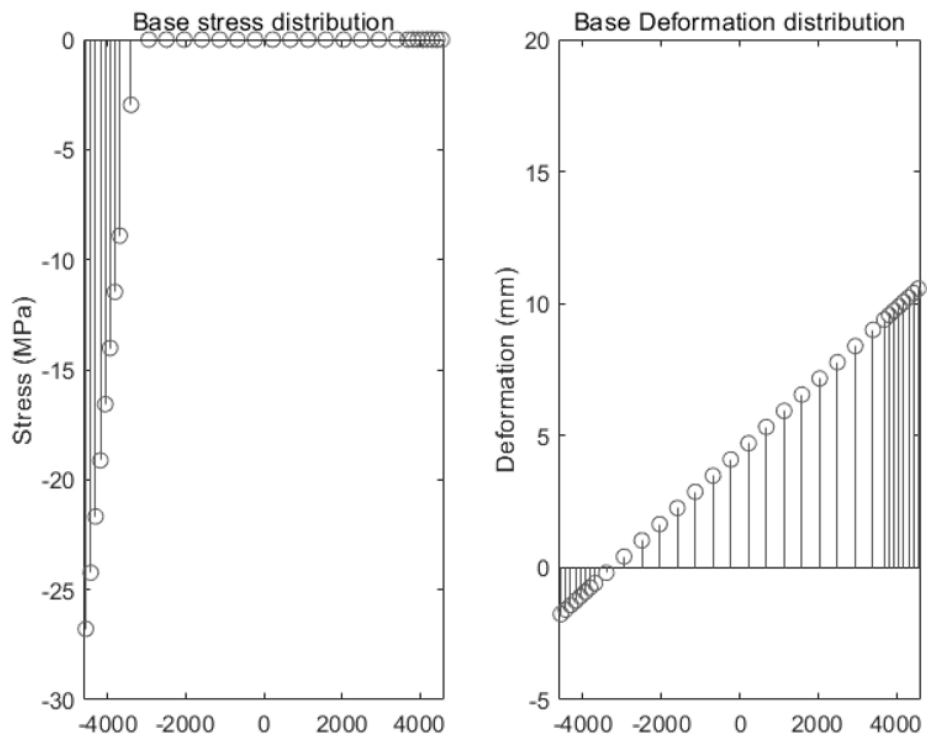


Figure 4.7. Stress and deformation of base springs

4.3 Modeling of CORW Dampers

CORW dampers are all modeled using Zero-length elements with a calibrated material model on the desired DOF, and rigid elastic material on the other DOFs. Five constitutive models were created based on experimental results of the five types of energy dissipators in OpenSees (PEER, 2006).

The RSFJ was modeled using *SelfCentering* material (Christopoulos et al., 2008) in OpenSees with the initial stiffness K_1 , post-yielding stiffness K_2 , activation force F_{act} and flag shape controlling parameter β of 0.84 to match experimental results obtained from previous research (Hashemi et al., 2018). Identical loading history was used, of which displacement amplitudes are 15, 45, 70 and 100% of the maximum displacement 100 mm.

FFBRF was modeled using Steel02 material in OpenSees. Isotropic hardening parameters a_1 and a_2 were set as 0.06 and 0.9, respectively, for a better fit to the experimental results.

HF2V was modeled using Elastic-Perfectly-Plastic material model (ElasticPP material in OpenSees). EPP is a simplified model for HF2V. The simplification has four reasons: 1) When the prototype building was originally designed, HF2V was selected. The design assumes that HF2V has an EPP hysteresis. Modeling HF2V using EPP is to be consistent with the EEDP design in order to validate it; 2) HF2V has very low velocity-dependent rate and showed a relatively flat ‘post-yielding’ behavior. Previous research (G W Rodgers et al., 2008) has pointed out that HF2V could be considered as a hysteretic elastic-plastic damper. HF2V has also been widely used in other structural systems (Rodgers, 2009; Rodgers et al., 2008; Sadeghi et al., 2020).

FVD was modeled using a Maxwell material model (ViscousDamper material in OpenSees). This type of material is composed of a dashpot with damping coefficient C and exponent α , in series with a spring with stiffness K . The model is shown schematically in Figure 4.8a. By using Maxwell model, the flexibility of damper structure and connectors are considered.

VED was modeled using Maxwell representation of solid viscoelastic material, composed of a Maxwell element with damping coefficient C and stiffness K_1 , in parallel with another spring with stiffness K_2 . The model is shown schematically in Figure 4.8b. The calibrated material was validated based on the experimental results from Aprile et al. (1997)

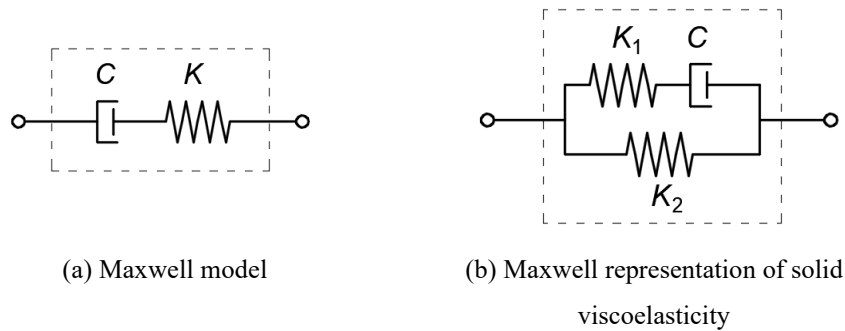
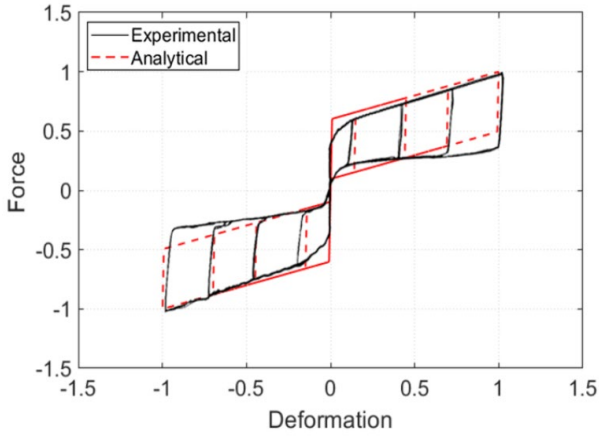
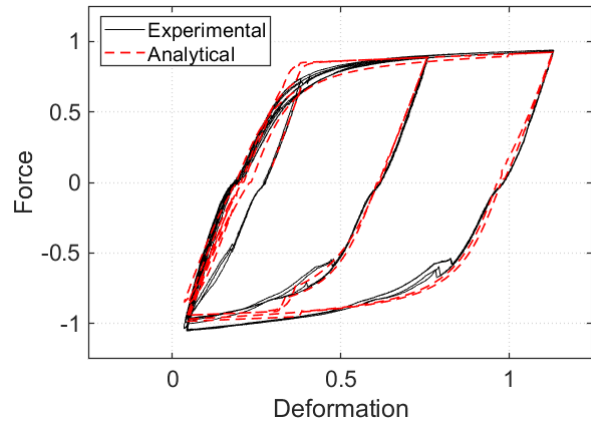


Figure 4.8. Modeling of FVD and VED

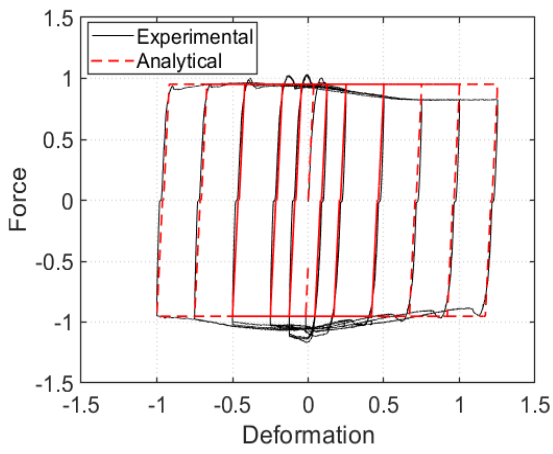
Figure 4.9 summarized all five damper models with calibrations against experimental results for validation. The experimental results are shown in black lines while the analytical results are shown in red dashed lines. It shows good match between analytical and experimental hysteresis loops for all of the five types of the dampers.



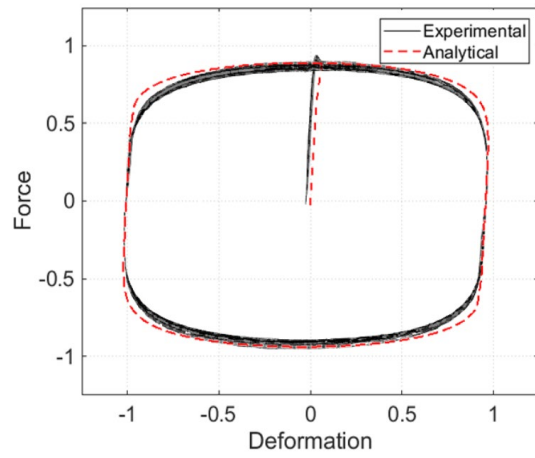
(a) SCD (RSFJ) (Hashemi et al., 2018)



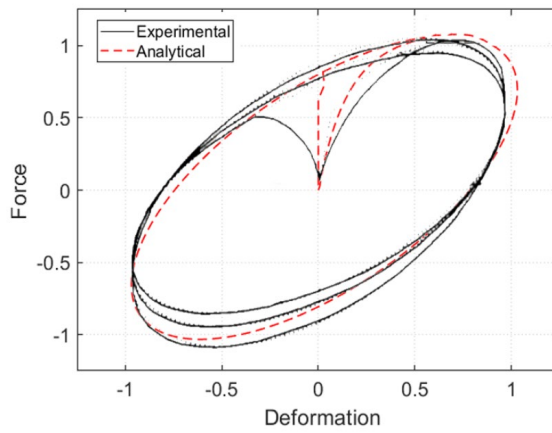
(b) MYD (FFBRF)



(c) EPP (HF2V)



(d) FVD



(e) VED (Perez, 2004)

Figure 4.9. Experimental validations of modeling of CORW dampers

4.4 Ground Motion Selection

Suite of ground motions were selected from PEER NGA West2 Database (PEER, 2013) to match the target spectra listed in Figure 4.10. The magnitudes of the earthquake events were restricted from 5.0 to 8.0. No more than two records from each event were used. The ground motion were amplitude scaled following the specifications in Commentary J of the National Building Code of Canada (NRCC, 2015). Scaling factors were limited from 0.25~4. Ground motions were scaled to match a period range of 0.3~4 sec to capture higher modes and the period elongation due to nonlinear behavior. Figure 4.10 shows the scaled ground motions compared with the design spectrums and Figure 4.11 shows the summary of the ground motions used and the scaling factors.

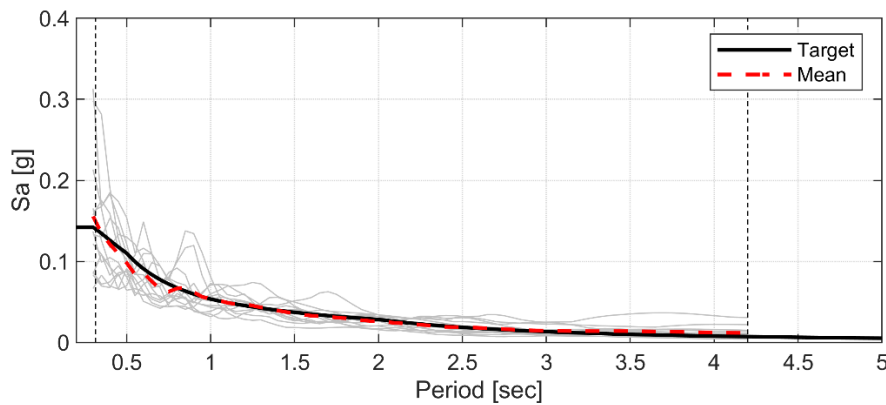


Figure 4.10. Response spectra of all scaled ground motions (SLE)

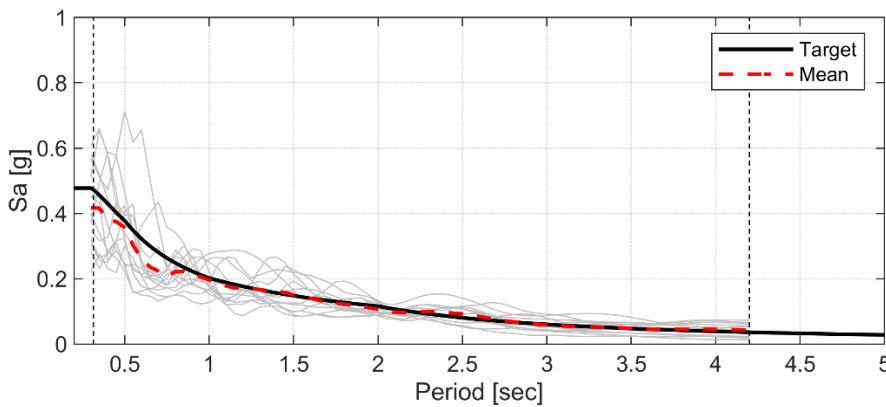


Figure 4.11. Response spectra of all scaled ground motions (DBE)

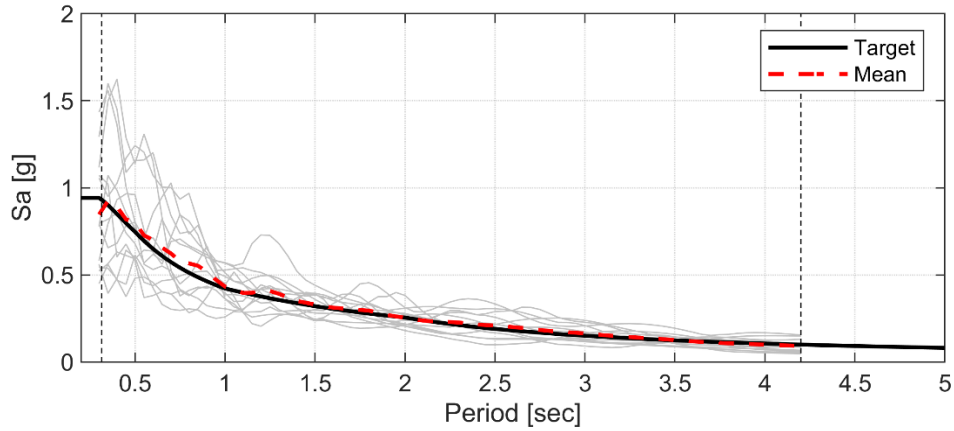


Figure 4.12. Response spectra of all scaled ground motions (MCE)

Table 4.1 shows result obtained from eigenvalue analysis using OpenSees software (PEER, 2006).

The first three modes of the prototype are 2.72, 0.51 and 0.20 seconds.

Table 4.2. Natural periods of the prototype (first 3 modes)

Mode	1	2	3
Mode shape			
Period	2.72 sec	0.51 sec	0.20 sec

The detailed information about the selected ground motions are shown in Table 4.3. Different ground motion records are selected for SLE, DBE and MCE for reasonable scaling factors. More information about the ground motions can be found in Appendix A.

Table 4.3. Ground motion information and scaling

SLE			DBE			MCE		
RSN	Event	Scale	RSN	Event	Scale	RSN	Event	Scale
9	Borrego	0.66	6	Imperial Valley	0.54	139	Tabas, Iran	2.23
25	Northern Calif-4	1.45	9	Borrego	3.15	143	Tabas, Iran	0.50
31	Parkfield	0.50	28	Parkfield	3.10	187	Imperial Valley	3.03
65	San Fernando	0.73	96	Managua	0.82	285	Irpinia, Italy-1	2.05
93	San Fernando	0.83	138	Tabas, Iran	1.32	292	Irpinia, Italy-1	1.18
164	Imperial Valley-6	0.33	187	Imperial Valley-6	1.15	313	Corinth, Greece	1.83
187	Imperial Valley-6	0.35	294	Irpinia, Italy-1	3.59	587	New Zealand-2	1.93
280	Trinidad	0.77	302	Irpinia, Italy-2	1.34	796	Loma Prieta	1.69
281	Trinidad	0.54	352	Coalinga-01	1.48	827	Cape Mendocino	2.04
288	Irpinia, Italy-1	0.43	832	Landers	1.06	832	Landers	2.39
294	Irpinia, Italy-1	0.97	1633	Manjil, Iran	0.53	1633	Manjil, Iran	1.20
353	Coalinga-1	0.66	3750	Cape Mendocino	0.59	3750	Cape Mendocino	1.32
832	Landers	0.30	4843	Chuetsu-oki, Japan	1.13	3757	Landers	1.77

4.5 Damping Settings

Overall, Rayleigh stiffness and mass proportional damping of 2.5% to the first and third mode was assigned to the model. Committed stiffness matrix was used for the stiffness proportion during analysis.

It is noted that the base springs in the multi-spring model are typical penalty elements (Hall, 2006), which may introduce unrealistic damping force if assigned Rayleigh stiffness proportional damping. When modeling the rocking base, the stiffness of the base spring is high in compression, in order to minimize the penetration of the wall base into the foundation, and low in tension to allow uplifting. If the stiffness proportion of damping is computed using such high stiffness in compression, large damping force could be generated upon uplifting, which could potentially restrain further movement and produce extremely high resisting forces. The base springs are created to implement restraints as rocking surface and are not expected to produce much damping effect. Thus, stiffness proportions of Rayleigh damping of the base springs are removed to avoid unrealistic high damping forces.

Chapter 5: Nonlinear Time History Analysis

Adopting the modeling technique presented in Chapter 4, nonlinear time history analysis was conducted for all damper combinations for the prototype CORW building under 13 ground motions at 3 hazard levels. In total, 975 cases were analyzed. Section 5.1 presents the results obtained from the nonlinear time history analysis of the prototype model (EPP as both outrigger and base dampers), including roof drift and overturning moment, story drift, acceleration, story moment, story shear and local deformation. Section 5.2 presents the systematical comparison of the 25 combinations of dampers, including hysteretic loops, roof drifts, energy dissipation, various story responses and damper velocities.

5.1 Results of Prototype Combination

5.1.1 Roof Drift

Each of the ground motions were analyzed for the prototype CORW system with EPP dampers for both outrigger and base. Figure 5.1 shows the normalized peak roof drifts (D) normalized using the designed ultimate roof drifts (D_u) at the MCE hazard level, where the median, upper and lower 75 percentile and extreme values are shown on each box plot. The results show that the median roof drift matched the designed target roof drift under all three hazard levels considered.

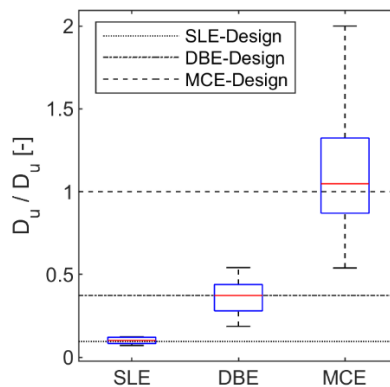


Figure 5.1. Comparison between EEDP design and prototype results from nonlinear time history analysis

5.1.2 Yielding States

Figure 5.2a presents the maximum peak damper deformation (d_{OR}) of the two outrigger dampers (east and west side) recorded from nonlinear time history analyses which is normalized using the ultimate design displacements ($d_{u,OR}$). Figure 5.2b shows the similar local deformation for the base dampers (d_{OR}) normalized using the ultimate design displacements ($d_{u,BS}$). In addition, a dash line has been added to indicate the yield displacement of the dampers. As expected, at the SLE hazard level, neither the base nor outrigger dampers has yielded. This indicates that the CORW remain fully elastic. At the DBE level, outriggers dampers have yielded, while the median base dampers have a displacement almost equal to the yield displacement. At MCE level, both outrigger and base dampers have yield under all ground motions. These results imply that the procedure outlined in this paper is effective in designing CORW system.

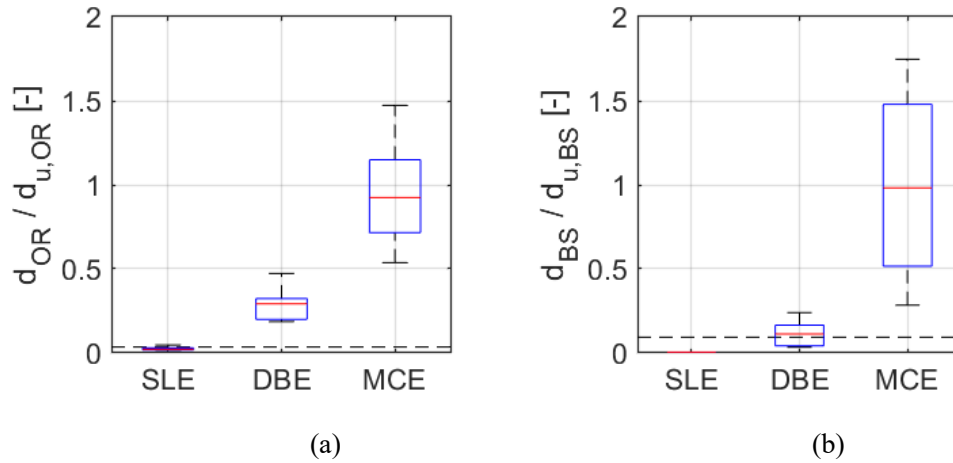


Figure 5.2. Local deformation of the EPP dampers

5.2 Comparison of Different Damper Combinations

To compare the response of CORW with different dampers, the analytical study was expanded to include nonlinear time history analyses of the CORW prototype building with 25 different damper combinations (5 types for outrigger damper, and 5 types for base damper) under all selected ground motions. In total, 975 analysis cases were analyzed. For simplicity, O-B denotes the damper combination, where O is the type of

outrigger damper and B is the type of base damper, e.g., EPP^O-FVD^B denotes EPP damper is used as the outrigger damper, while FVD is used as the base damper. The benchmark model which uses the EPP^O-EPP^B is denoted as ‘BM’ in the following text.

5.2.1 Hysteretic Loops of Dampers

Figure 5.3 and Figure 5.4 shows response spectrum and acceleration time history of a typical ground motion #143, which has a similar response spectrum to the mean and target spectra. This ground motion was recorded from the 1978 Tabas Earthquake, at Tabas Station, with a scaled peak ground acceleration of 0.43g, and a 5%~95% strong motion duration of 16.5 seconds.

shows all hysteretic loops of outrigger dampers and base dampers for the 25 combinations, respectively. The force and deformation are normalized using the F_u and D_u of the EPP^O-EPP^B design. Each row of the subplots shows the combinations with the same type of outrigger dampers. Each column of the subplots shows the combinations with the same type of base dampers. Hysteretic loops in solid and dashed lines stand for dampers installed at the East and West side of the prototype building, respectively. Based on the results presented, the damper response is not significantly affected by the different damper combinations. In general, almost all damper forces (SCD, MYD, EPP and FVD) are capped by 120% of the design force, while the damper force in the VED dampers are capped by 150% of the design force. Such over strength of the damper needs to be accounted for during design, hence the connection and the remaining of the structure can be capacity designed to remain elastic. It should be note that if needed, specially designed connections (Smith & Willford, 2007) can be placed at the end of the damper to do not exceed the ultimate force design limits.

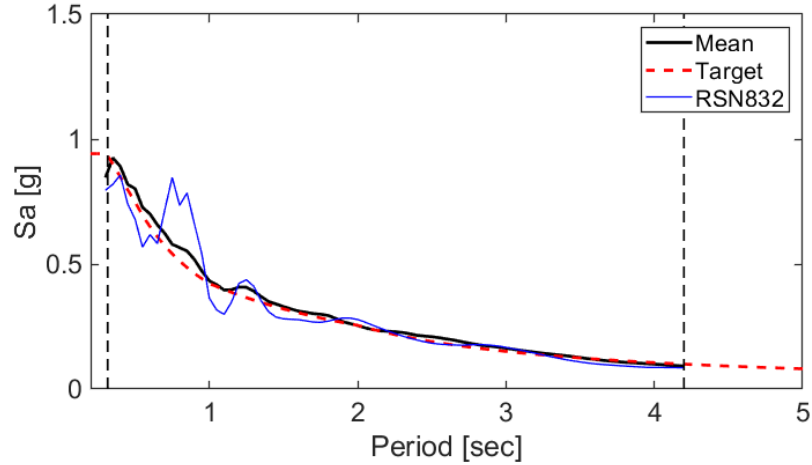


Figure 5.3. Sample ground motion selected for comparison

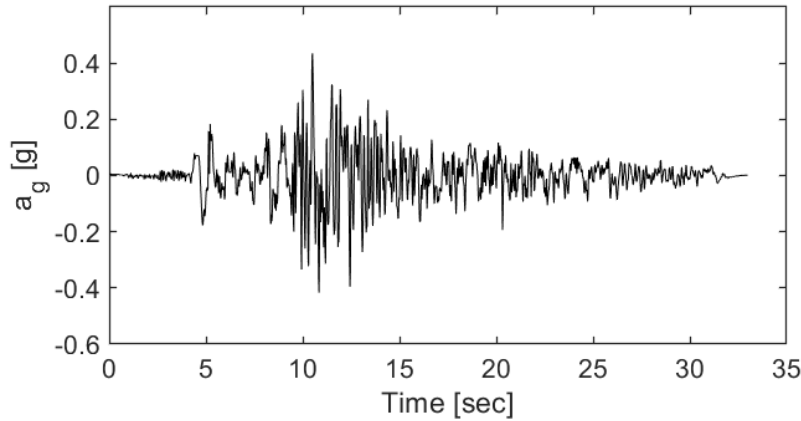


Figure 5.4. Ground motion acceleration time history

Figure 5.5 and Figure 5.6 shows all hysteretic loops of outrigger dampers and base dampers for the 25 combinations, respectively. The force and deformation are normalized using the F_u and D_u of the EPP^O-EPP^B design. Each row of the subplots shows the combinations with the same type of outrigger dampers. Each column of the subplots shows the combinations with the same type of base dampers. Hysteretic loops in solid and dashed lines stand for dampers installed at the East and West side of the prototype building, respectively. Based on the results presented, the damper response is not significantly affected by the different damper combinations. In general, almost all damper forces (SCD, MYD, EPP and FVD) are capped by 120% of the design force, while the damper force in the VED dampers are capped by 150% of

the design force. Such over strength of the damper needs to be accounted for during design, hence the connection and the remaining of the structure can be capacity designed to remain elastic. It should be note that if needed, specially designed connections (Smith & Willford, 2007) can be placed at the end of the damper to do not exceed the ultimate force design limits.

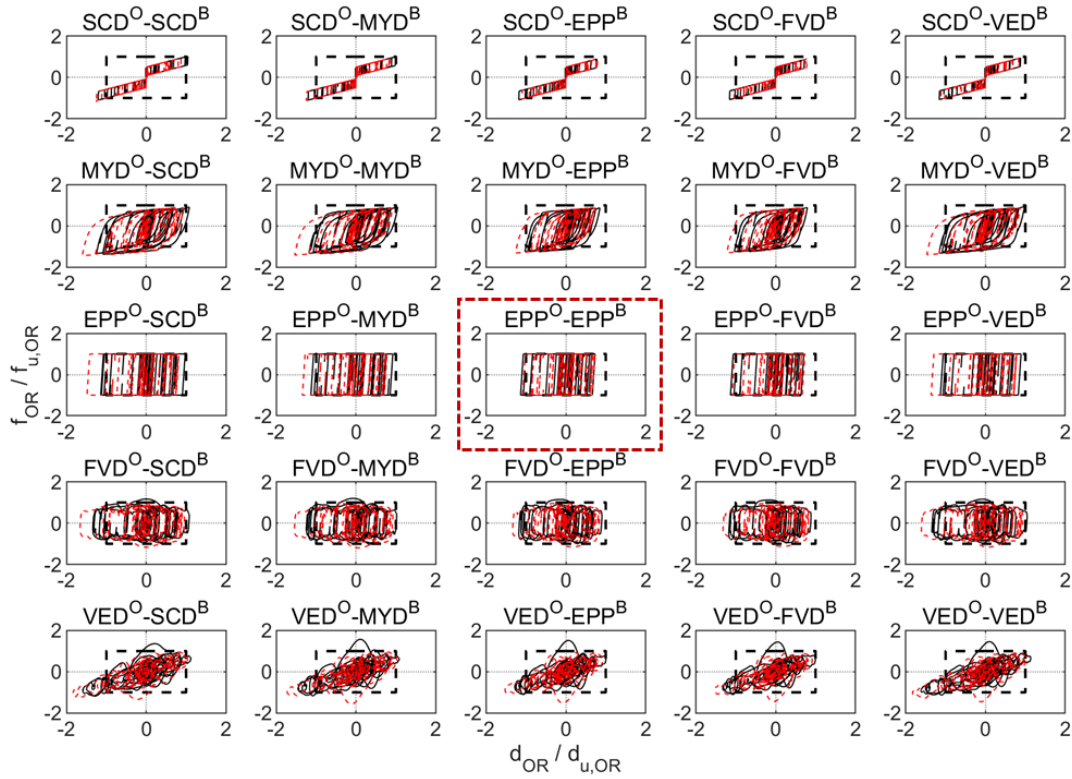


Figure 5.5. Outrigger damper hysteretic loops

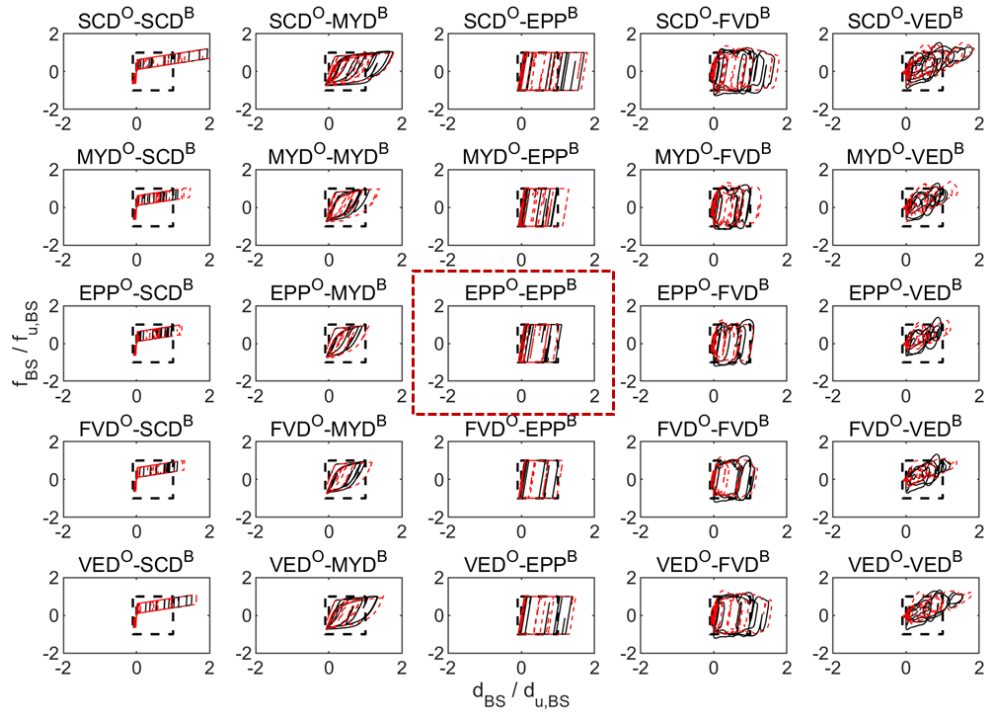


Figure 5.6. Base damper hysteretic loops

5.2.2 Roof Drift

Figure 5.7 shows a box plot of resulted peak roof drift ratio (RDR). Each box stands for the distribution of response for a certain combination, under 13 ground motions. The center dot shows the median value, and the black bar shows the range between -75 and +75 percentile. The bars further extend to show extreme values. In addition, a dash line is added to the graph to show the target design RDR at the SLE, DBE and MCE hazard levels. Overall, at all hazard levels, the median RDRs matches well to the target RDR for all damper configurations considered. At the SLE hazard level, all median RDR matches the target RDR with low standard deviation. At the DBE and MCE hazard levels, when the outrigger is equipped with the SCD and VED, the RDR has higher median and standard deviation as compared to the MYD, EPP damper and FVD. It should be note that the RDR is more sensitive to the outrigger damper as compared to the base damper.

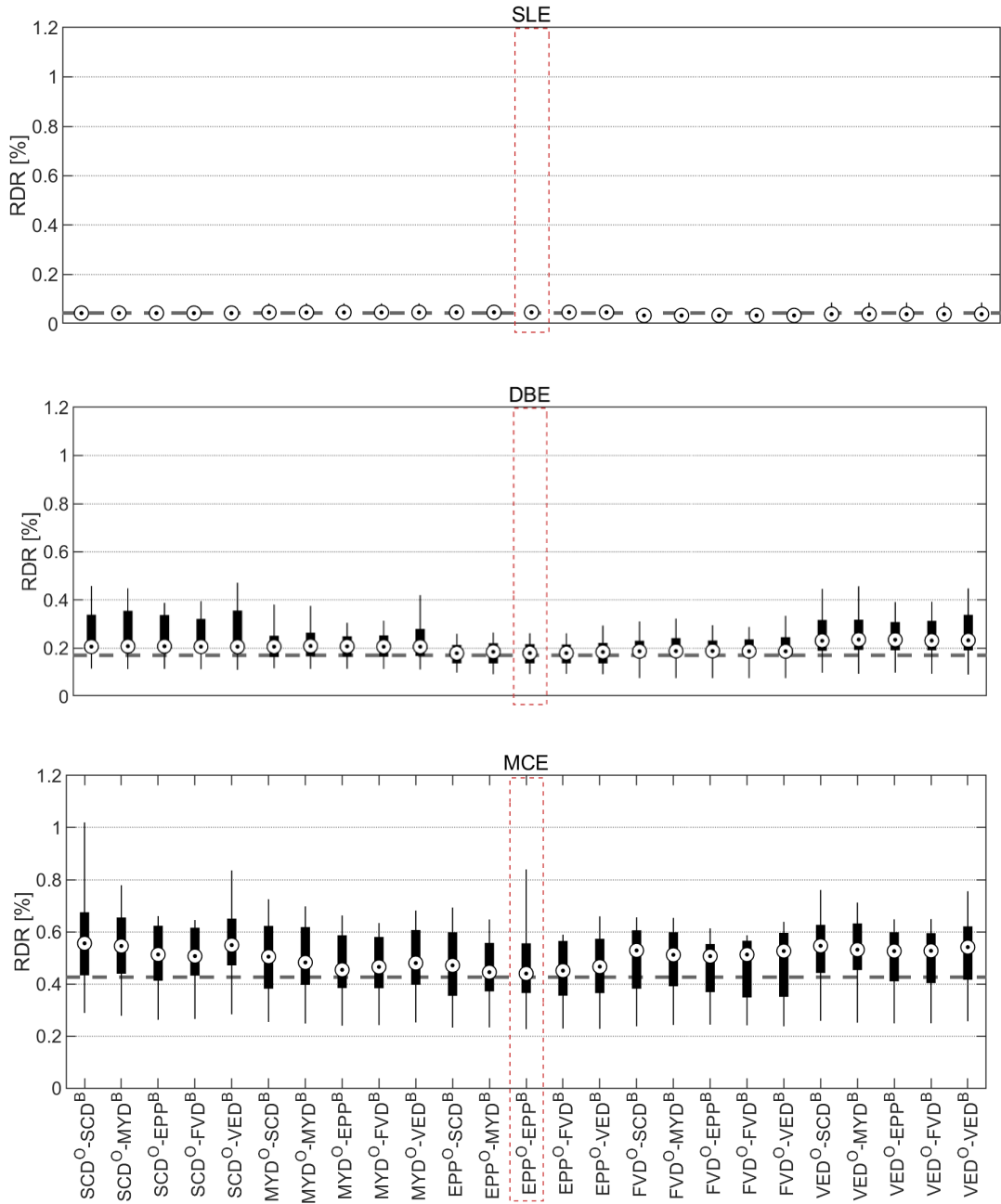


Figure 5.7. Roof drift of 25 combinations from nonlinear time history analysis

(SLE, DBE and MCE)

5.2.3 Story Response

Figure 5.8 present the peak story drift, inter-story drift ratio (ISDR), floor acceleration, story shear demand capacity ratio (DCR) and moment DCR results of the wall under the 25 damper combinations, respectively. The result shows that the responses of the wall is very comparable for all damper configurations. Overall, the structure has well controlled ISDR, peak floor acceleration, shear and moment DCRs.

ISDR is well under control, while the acceleration is also reasonable under all hazard levels considered. The story moment and story shear are both under the capacity, implicating efficient damper design. The peak ISDR of all combinations range 95~124% of the benchmark. The acceleration response ranges slightly more, from 89 to 150% of the benchmark for all combinations except for SCD^O-SCD^B and SCD^O-MYD^B at MCE level. SCD^O-SCD^B and SCD^O-MYD^B exhibits 40~70% higher acceleration at first three levels, and 15~16% higher at rooftop compared with the benchmark at MCE level. On the other hand, combinations with FVD or VED as outrigger dampers exhibit 10~30% lower acceleration than the benchmark, especially in SLE and DBE. Viscous dampers as outrigger dampers may control the acceleration of CORW system even better than EPP.

The maximum shear of observed among all models reaches 76% of the shear capacity. For all combinations, individual maximum shear DCR range 36~76%. Hence, elastic assumption for wall elements used in numerical modeling is still acceptable. The structural wall remains undamaged though MCE level earthquake excitation for all combinations.

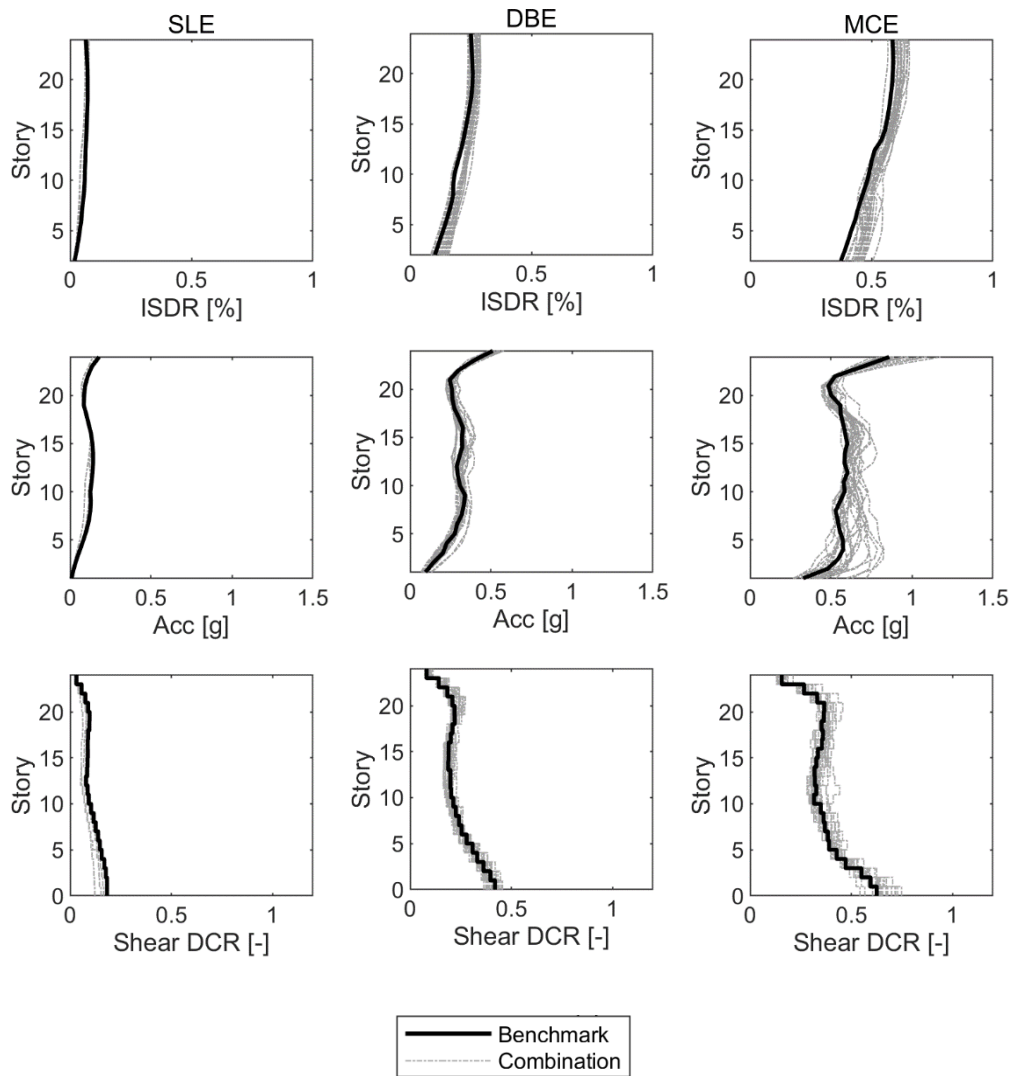


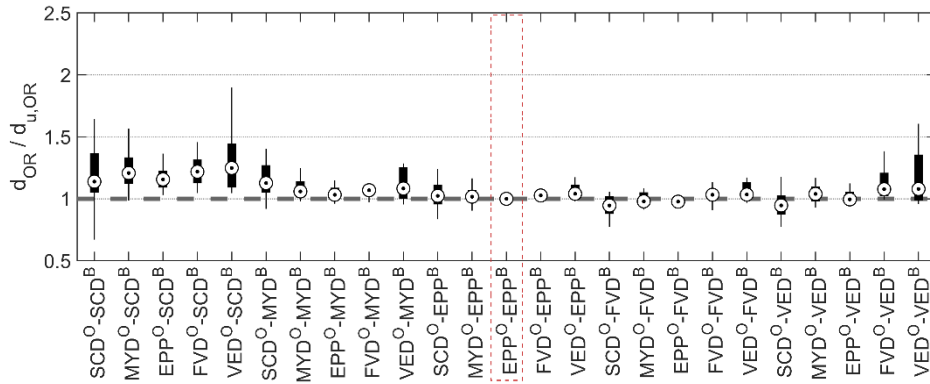
Figure 5.8. Median structural response comparison for damper combinations under MCE

Figure 5.9a-b shows the peak local deformation of the dampers at outrigger (d_{OR}) and base (d_{BS}) under MCE level hazard, normalized by their designed ultimate values ($d_{u,OR}$ and $d_{u,BS}$), respectively. Overall, the peak outrigger damper displacement is very comparable for all damper combinations considered. The SCD and VED has slightly higher median and standard deviation of the damper displacement than the MYD,

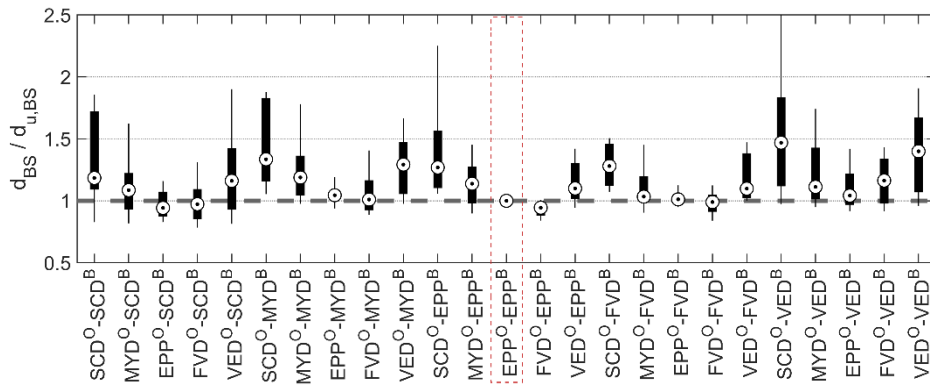
EPP damper and FVD. On the other hand, base damper displacement varies significantly with different damper configurations.

For base dampers among different combinations, the median peak local deformation ranges from 95% to 120% of the benchmark combination, which means that it introduces approximately 25% error in the estimation of local deformation for alternative dampers. For all combinations except for VED, the median local deformation of outrigger dampers fluctuates between 95% and 140% of the benchmark combination, suggesting that base dampers have relatively more deviation, in terms of local response. When designing dampers using the proposed procedure, designers may need to be conservative in local deformation demand to ensure the dampers have sufficient deformation capacity.

Combinations with FVD (designed with an equivalent energy to EPP) showed excellent match in both the local and global responses, indicating the proposed design procedure for FVD is efficient. Compared with FVD, VED showed large deviation in local deformation, which may be explained by the uncertainty and sensitivity caused by its significant velocity dependency. When applied in engineering practice, more conservativity should be considered for VED.



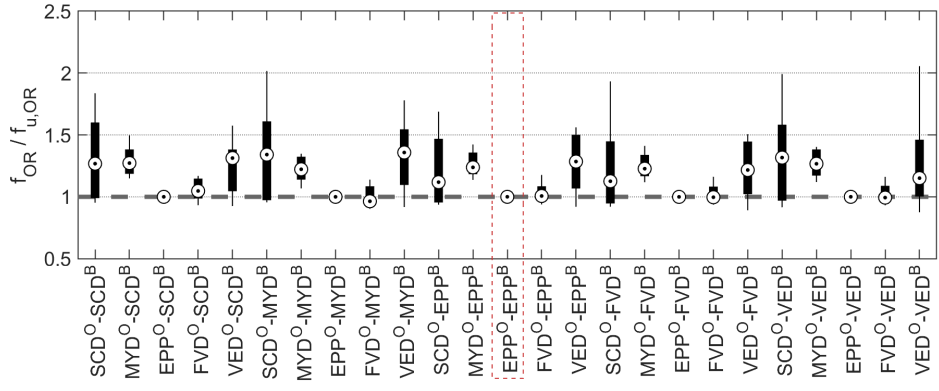
(a) Outrigger dampers



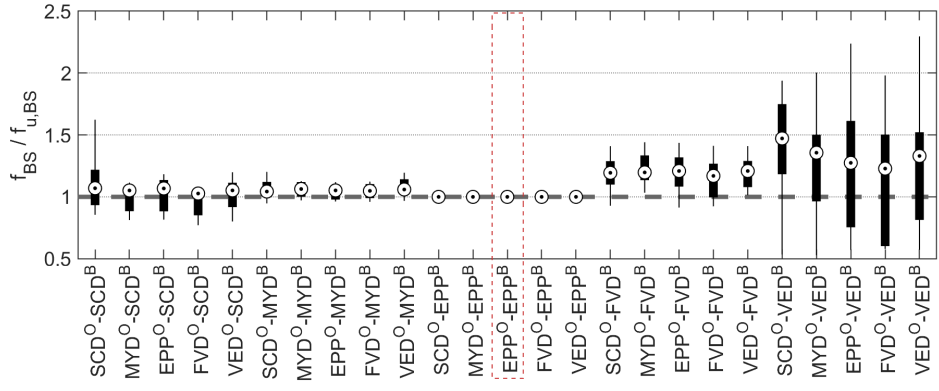
(b) Base dampers

Figure 5.9. Damper deformation comparison for all combinations under MCE

For base dampers, VED has a nearly 50% overstrength. Comparing two types of viscous dampers VED with FVD, VED has much higher overstrength and uncertainty in force, which can be explained by VED's high velocity dependency. High velocity dependency introduces more overstrength and uncertainty in local deformation and force, which is not ideal for CORW system. In engineering practice, force-limiting devices may be required to control the overstrength of VED. Despite the diversity in local behaviors, the global response remains similar among all combinations, which indicates that the design is still efficient with sufficient conservativity in local damper design.



(a) Outrigger dampers



(b) base dampers

Figure 5.10. Damper force comparison for all combinations under MCE

Chapter 6: Experimental Testing

Intensive numerical studies in the previous chapter has shown that EEDP global and local design and are response well. The numerical studies also show that the CORW system can be applied as an efficient, resilient SFRS. However, the accuracy of the numerical results needs to be further validated by experimental results. Hybrid simulation is an experimental method that combines laboratory testing and numerical simulation, where one portion of the structure, which is hard to model, being tested in laboratories, while the rest of the structural system, which is easier to predict, being numerically solved in computer.

Using hybrid simulation to validate numerical results instead of conventional shake table testing has four advantages. First, it is both challenging and cost-inefficient to launch a series of large-scale shake table tests for high-rise structural systems. Second, it is not ideal to drastically scale down concrete specimens since small-scaled concrete and reinforcements have significantly different behavior compared with realistic ones. Third, frequent pounding between the rocking base and the foundation in CORW system and the shake table makes it difficult to measure acceleration and control the table (Crozet et al., 2019). Finally, it is easy to test multiple innovative specimens as a part of the structural system in hybrid simulations, while parts in shake-table test specimens may not be easily changed or modified.

In this chapter, two HF2V dampers were experimentally tested in the Structural Laboratory of the University of British Columbia, while the remainder of the structural system was numerically analyzed in computer utilizing the Advance Control Testing System (ACTS) controller and software. The resulted structural response from hybrid simulation is used to validate the numerical results.

6.1 Experimental setup

The component tests took place in the Structural Laboratory of the Department of Civil Engineering, at the University of British Columbia, Canada. The laboratory has a 450 m² area for all structural engineering testing setup, where a 4.9-meter-high L-shaped strong wall was built on a 9.0 x 22.0 m strong floor. The

laboratory is also equipped with two sets of MTS hydraulic systems: a MTS 506.61 model hydraulic unit, capable of providing 70 gpm flow rate at 3000 psi working pressure, located in the basement; a MTS hydraulic unit capable of providing 20 gpm flow rate at 3000 psi working pressure, located to the northbound facility room of the laboratory.

The designated testing setup is located in the southwest corner of the L-shaped strong wall, consists of two dynamic actuators, load cells, roller-based loading case, two specimens and a reaction seat, as shown in Figure 6.1. The two MTS 201.60 model actuators are able to generate 648 kN force in tension, and 1013 kN force in compression, powered by the 20 gpm, 3000 psi hydraulic MTS power unit. The actuators also have built-in Temposonics linear displacement transducers. The maximum stroke of the actuator is 508 mm.

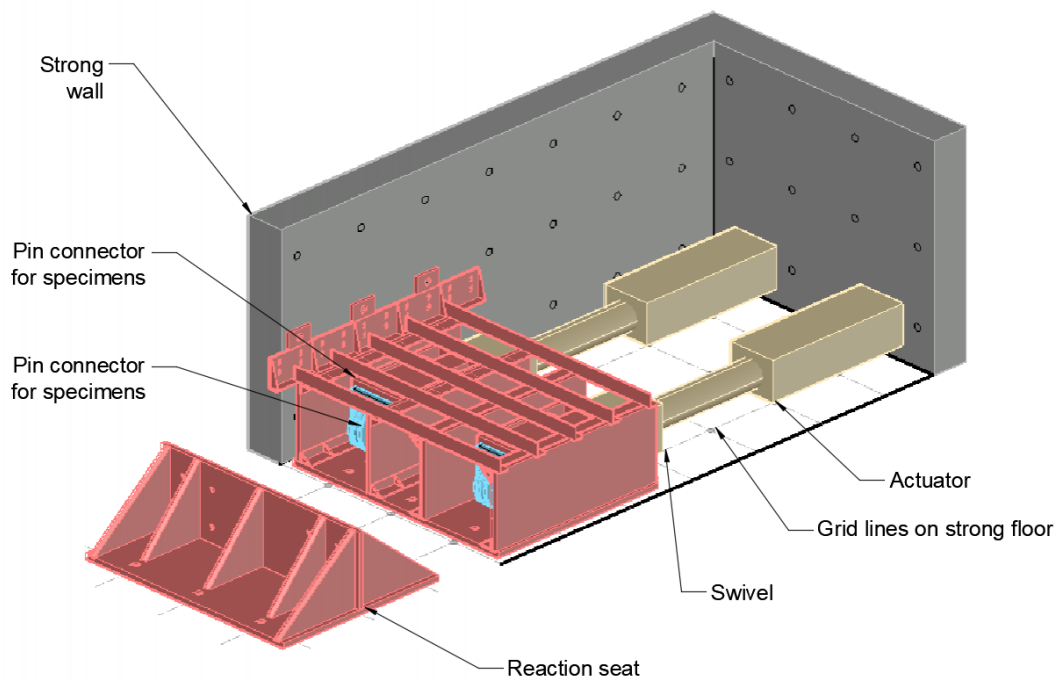
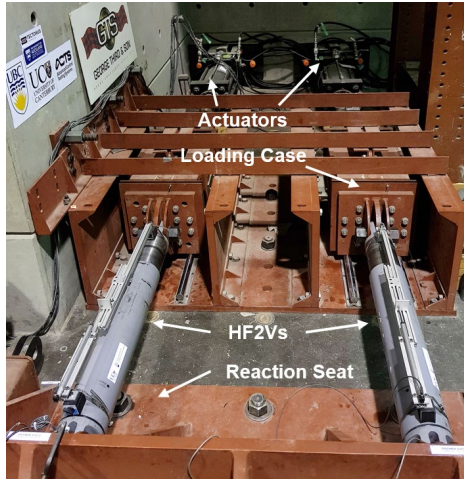
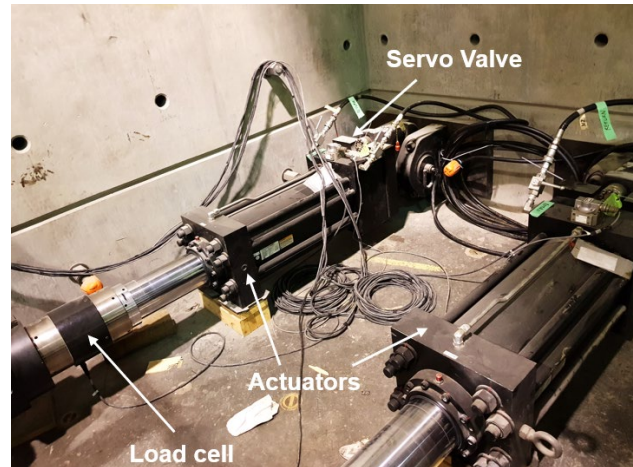


Figure 6.1. Schematic view of experimental testing setup



(a) Overall view of test setup



(b) Actuators and servo valves

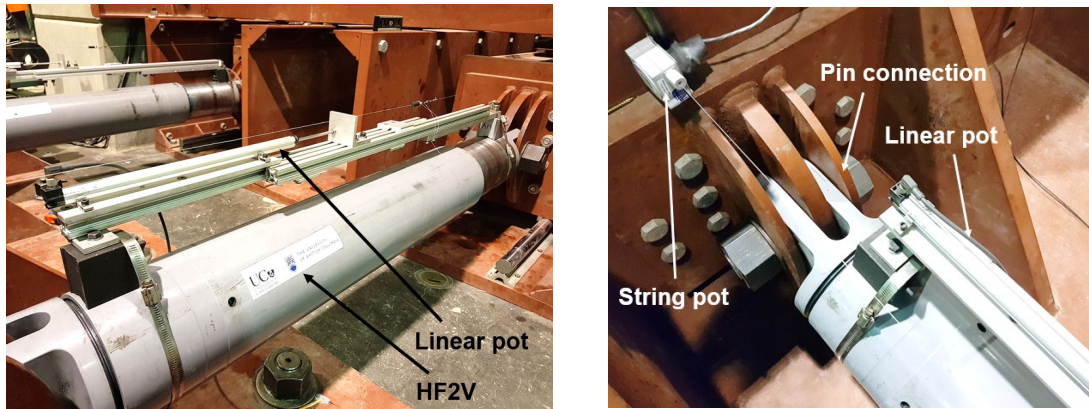
Figure 6.2. Experimental testing setup

The actuator is connected to a swivel and then to the loading case, mounted on wheels and floor tracks to reduce friction. The loading case also has steel wheels the other three side surfaces, in order to guide the uniaxial movement. The reaction seat is connected to the strong floor by six post-tensioned threaded rods with 50.8 mm nominal diameter, providing approximately 1000 kN clamping force. The two specimens were to be connected to the loading case and the reaction seat by 50.8-mm-diameter high-strength true pins at both ends. The industry sponsors include George Third & Son, Pacific Bolt Manufacturing Ltd., Custom Plate & Profiles, Canadian Institute of Steel Construction, StarSeismic, and Tectonus.

6.2 Instrumentations

The instrumentation of the testing setup includes two load cells for force feedback, two linear potentiometers by Novotechnik for displacement feedback, two string potentiometers, and two built-in Temposonics displacement transducer for displacement monitoring and measurement, and cameras. The two linear potentiometers are mounted directly on specimen body by aluminum tracks, in order to measure the core displacements of the specimens. The aluminum tracks are connected to magnetic bases and steel

straps on both ends. The magnetic bases and steel straps are expected to provide adequate friction force to prevent any sliding between instruments and surfaces of the specimens.



(a) Linear potentiometer

(b) String potentiometer

Figure 6.3. Instrumentation setup

Trial tests show three sources of slippage in the testing setup – clearance in the true pin connections, slippage between the reaction seat and the strong floor, and slippage between the swivel of actuator and the loading case. These sources of slippage are minimized by taking the core displacement as displacement feedback for controller. Among these three sources of slippages, the clearance between pin and pin connector exists in engineering practice as pin connection is not always perfectly tight. However, it is not ideal to include slippage in the displacement feedback for control, since it creates difficulties in determining the initial position of the damper, which adds uncertainty to damper and structural behavior. The initial slippage also produces a much lower initial stiffness than the damper’s stiffness. The stiffness will drastically change after slippage, which create difficulties in both low-level and high-level control. Thus, the core displacement of damper is used as displacement feedback for control. To evaluate this slippage, two string potentiometers are installed to record the end-to-end deformation, running from the loading case to the reaction seat.

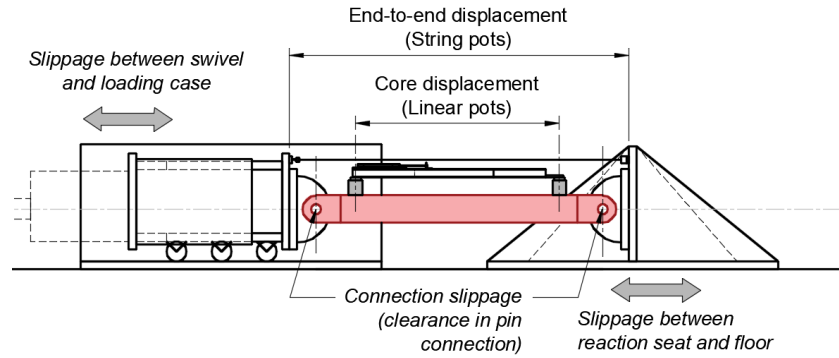


Figure 6.4. Sources of slippage in experimental testing setup

A data acquisition system provided by Advanced Control Testing System (ACTS) have been set up to acquire and process all signals, from load cells, linear potentiometers, string potentiometers and Temposonics displacement transducers, taking up 2A/B, 5A/B, 6A/B and 4A/B channels of the ACTS data acquisition system, respectively. The linear potentiometers and Temposonics displacement transducer use 7 V excitation and produce single ended analog signals, while the load cell uses 10 V excitation. A 15 Hz Butterworth second-order low-pass filter, and a 50 Hz third-order Butterworth low-pass filter are applied for all displacement and force signals, respectively.

6.3 Component Testing

Two High-Force-to-Volume (HF2V) devices are available for component testing. This section presents the mechanism, loading protocol, test results and discussions of HF2V devices.

6.3.1 Loading Protocol

The quasi-static cyclic loading protocol of the component test follows ATC-24 (Mortazavi et al., 1992) guidelines for loading protocols. Considering that the HF2V have very low yielding deformation and relatively large and highly nonlinear inelastic deformation, the loading protocol has been slightly modified. The six cycles with an amplitude lower than yielding deformation are removed, and replaced by three cycles

at 5 mm. The deformation amplitudes are set as 5, 10, 20, 30 and 40 mm for both tensile and compressive directions, and 50 mm for tensile direction.

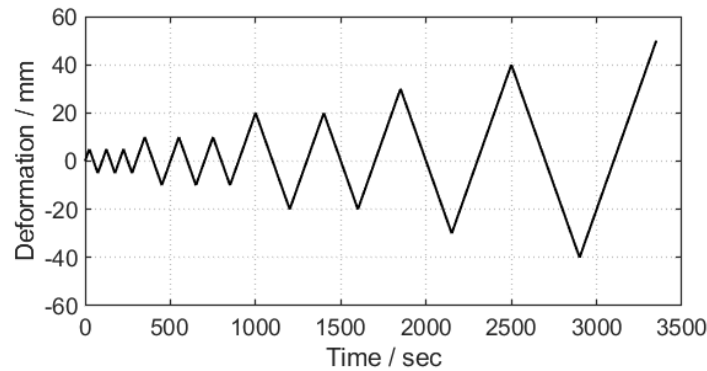


Figure 6.5. Loading protocol for HF2V

6.3.2 Results and Discussions

The tested force-deformation hysteresis for both devices in the laboratory are shown together in Figure 6.6. The hysteretic behavior of the HF2V devices are found to be close to elastic-plastic hysteretic behavior with weak a velocity-dependency described in various constitutive models. The force levels are between 350~450 kN in tension, and 450~550 kN in compression. The asymmetry of force levels in compression and tension should be caused by the asymmetrical dynamic friction in the device. Almost no overstrength could be found while deformation increases, which makes the capacity design for other structural elements easier and makes it capable to protect other structural elements during major earthquake events. The optimal area enclosed by the force-deformation hysteresis also shows excellent hysteretic energy dissipation capacity of the device.

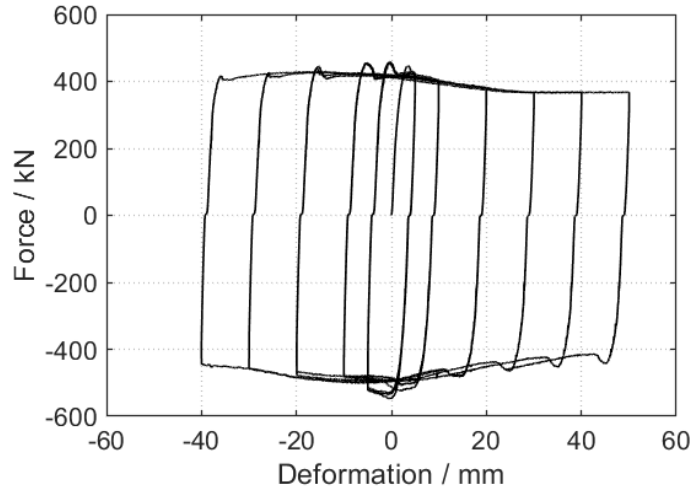


Figure 6.6. Component test result: force-deformation hysteresis of HF2V device 1

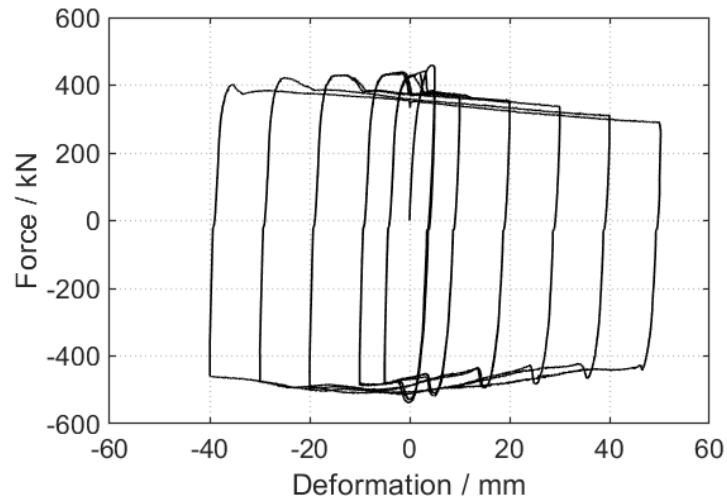
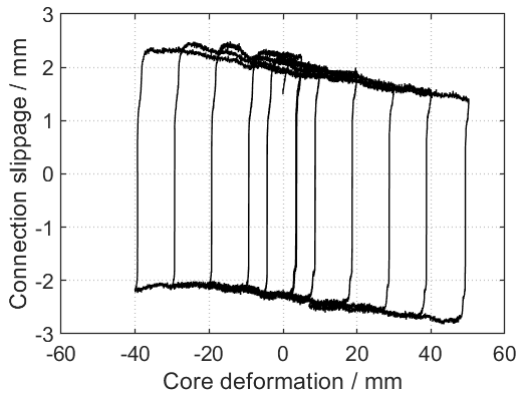
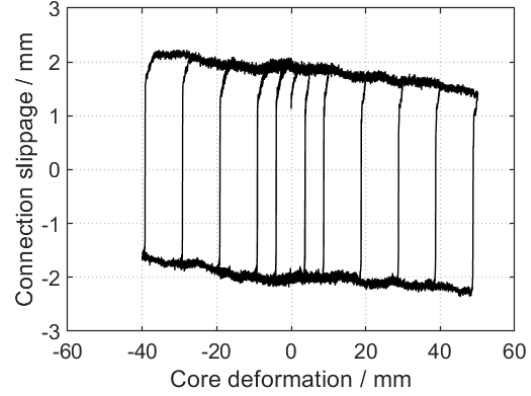


Figure 6.7. Component test result: force-deformation hysteresis of HF2V device 2

The connection slippage could be determined by subtracting core deformation from end-to-end deformation. As shown in Figure 6.8, the connection slippage happens upon reverse of the direction of imposed displacement. The connection slippage displacement keeps stable in most cycles, between 3.5~4 mm.



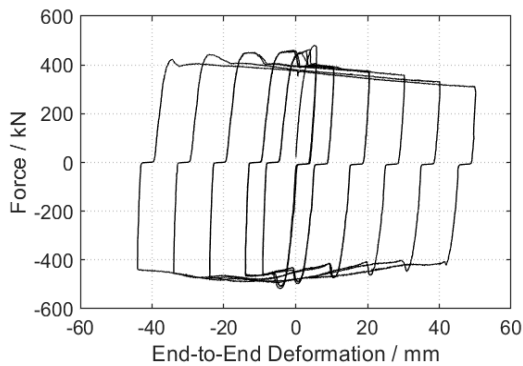
(a) HF2V device 1



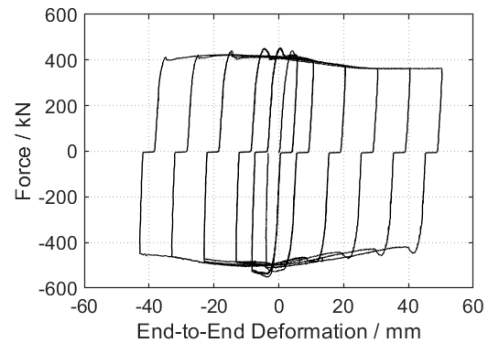
(b) HF2V device 2

Figure 6.8. Component test result: connection slippage of HF2V

The force-deformation relationships of both HF2V devices with end-to-end deformation are shown in Figure 6.9. The connection slippage could potentially create a ‘zero-initial-stiffness zone’, which not only affects the initial stability of the structure, but also make the SLE or DBE seismic structural behavior hard to predict. For example, if the device is used as outrigger damper in CORW system, under initial earthquake excitation, it may pick up force immediately, or slip to a certain point. Thus, the displacement of the outrigger is uncertain. This uncertainty could potentially make the performance under SLE and DBE levels hard to predict. Thus, it is recommended to reduce connection slippage as much as possible when used in CORW system.



(a) HF2V device 1



(b) HF2V device 2

Figure 6.9. Component test result: force-deformation hysteresis of HF2V (end-to-end deformation)

6.4 Hybrid Simulation of CORW System

The hybrid simulation model of the prototype CORW building is shown in Figure 6.10, where a pair of outrigger dampers were experimentally tested in the laboratory while the remainder of the structural system were analyzed in computer. The experimental setup remains the same as the component test setup. The setup has been presented in Chapter 3. It consists of two dynamic actuators, load cells, roller-based loading case, two specimens and a reaction seat. The two specimens are HF2Vs, connected to the loading case and the reaction seat by true pins at both ends.

The analytical sub-assembly resumes most modeling assumptions presented in Chapter 4. Multi-spring model is used to model the rocking base, with Concrete01 material and tributary wall section area assigned to each of the base springs. The wall was modeled as elastic beam-column (EBC) element. The mega-column was modeled as truss element. The base dampers were numerically modeled using the same parameters as modeled in Chapter 4. Nevertheless, the base dampers are not expected to yield at DBE hazard level so they should stay elastic during the hybrid simulation.

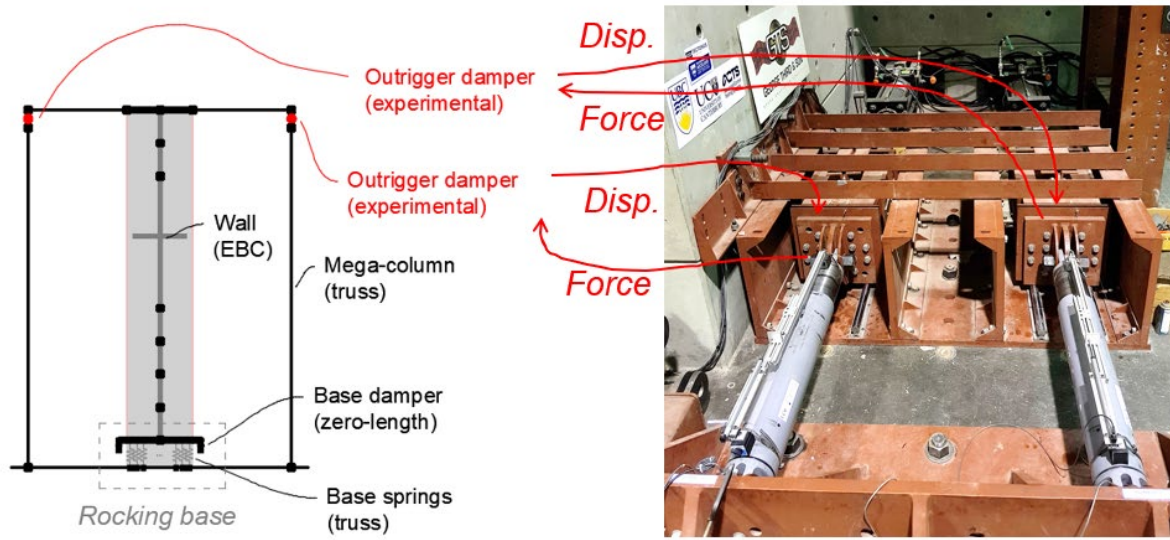


Figure 6.10. Schematic view of hybrid model

6.4.1 Input Ground Motion

The ground motion hazard and scaling of the hybrid simulation is slightly different from those mentioned in the nonlinear time history analysis section. Site class B is selected for hybrid simulation, which slightly reduces the intensity of the input ground motion.

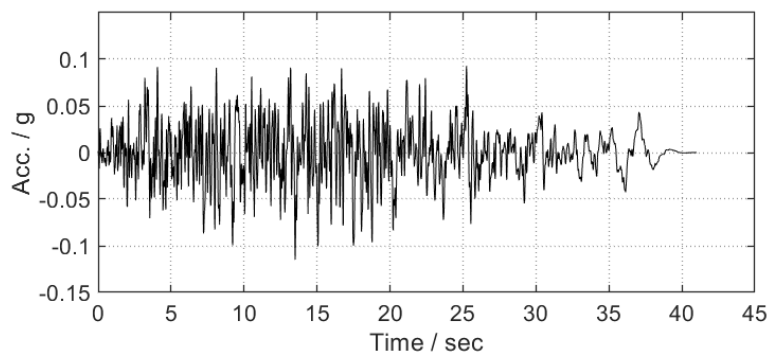
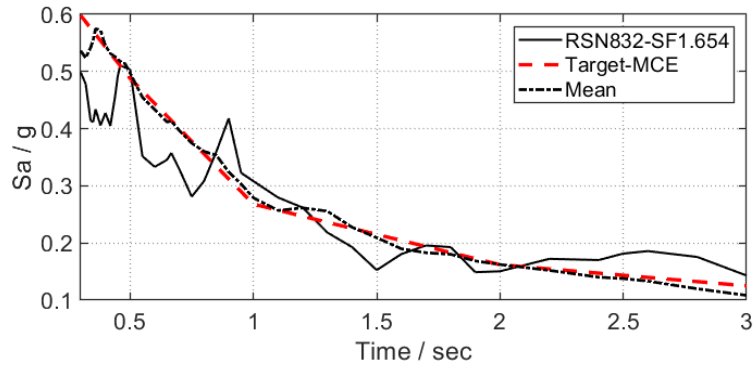


Figure 6.11. Ground motion time history for hybrid simulation



(b) Response spectrum

Figure 6.12. Response spectrum of the ground motion for hybrid simulation

6.4.2 Hybrid Control Strategy

A low-level controller in hierarchical control framework is setup to receive a reference signal, from a high-level controller. The reference signal is implemented through a closed loop control shown in Figure 6.13. The control error is defined as the difference between the reference signal and the displacement feedback measured by sensors. The error is sent to a PID controller, which produces command signals and send to the servo valves on the actuators to initiate motion. For the designated hybrid simulation, core deformations of the two specimens measured by the linear potentiometers are used as displacement feedback, while the reaction force measured by load cells on the two actuators are used as force feedback. The load cell typically needs 10 V excitation and produces Wheatstone bridge analog signals, and filtered by a 1.6 kHz low-pass filter with a gain of 100.

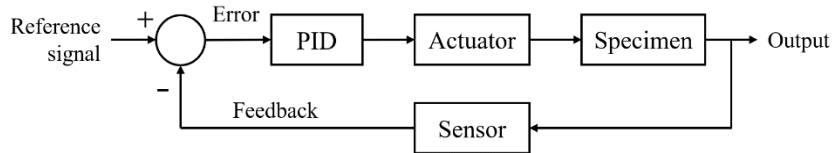


Figure 6.13. Control loop diagram of hybrid low-level controller

The high-level controller is a part of the analytical sub-assembly, which generates reference signals and receive both displacement and force feedback.

6.4.3 Hybrid Simulation Algorithm

The generalized equation of motion of a multi-degree-of-freedom (MDOF) system at analytical time step n is shown in Equation (6.1).

$$[M]\{\ddot{u}_n\} + [C]\{\dot{u}_n\} + \{R\} = \{P\} \quad (6.1)$$

where $[M]$, $[C]$ and $[R]$ are the mass matrix, damping matrix and resisting force vector of the MDOF system, respectively; $\{\ddot{u}_n\}$, $\{\dot{u}_n\}$ and $\{u_n\}$ are the acceleration vector, velocity vector and resisting force vector at a certain time t_n , respectively; $\{P\}$ is the exterior force vector.

This study is typically a displacement-based hybrid simulation (Yang et al., 2017). At time step $n+1$, the algorithm starts with a trial global displacement vector $\{u_{n+1}\}$ and transforms it to a trial local displacement vector $\{v_{n+1}\}$. With $\{v_{n+1}\}$ sent to both analytical and experimental sub-assemblies, the local element forces are returned and assembled into a local element force vector $\{q_{n+1}\}$, and then transformed to resisting force vector $\{R_{n+1}\}$. This procedure could be described in Equation (6.2).

$$\{R_{n+1}\} = [A_f]^T \{q_{n+1}\} = [A_f]^T f(\{v_{n+1}\}) = [A_f]^T f([A_f]\{u_{n+1}\}) \quad (6.2)$$

where $[A_f]$ is the compatibility matrix of the system, and f shows constitutive relationship of analytical or experimental sub-assembly. At the same time, $\{\dot{u}_{n+1}\}$ and $\{\ddot{u}_{n+1}\}$ are determined using classical Newmark integration method (average-acceleration time-step integration shown in Equation (6.3)).

$$\begin{cases} \{\ddot{u}_{n+1}\} = \frac{1}{\beta h^2} (\{u_{n+1}\} - \{u_n\} + h\{\dot{u}_n\}) - \left(\frac{1}{2\beta} - 1\right) \{\ddot{u}_n\} \\ \{\dot{u}_{n+1}\} = \frac{\gamma}{\beta h} (\{u_{n+1}\} - \{u_n\}) + \left(1 - \frac{\gamma}{\beta}\right) \{\dot{u}_n\} + \left(1 - \frac{\gamma}{2\beta}\right) h\{\ddot{u}_n\} \end{cases} \quad (6.3)$$

Substituting Equation (6.2) and (6.3) into Equation (6.1), the dynamic equilibrium equation of motion at time step $n+1$ could be obtained, as shown in Equation (6.4). With $\{u_{n+1}\}$ as the only unknown variable, equation could be numerically solved using Newton-Raphson iteration method.

$$\begin{aligned}
& [M] \left(\frac{1}{\beta h^2} (\{u_{n+1}\} - \{u_n\} + h\{\dot{u}_n\}) - \left(\frac{1}{2\beta} - 1 \right) \{\ddot{u}_n\} \right) \\
& + [C] \left(\frac{\gamma}{\beta h} (\{u_{n+1}\} - \{u_n\}) + \left(1 - \frac{\gamma}{\beta} \right) \{\dot{u}_n\} + \left(1 - \frac{\gamma}{2\beta} \right) h\{\ddot{u}_n\} \right) \\
& + [A_f]^T f([A_f]\{u_{n+1}\}) - \{P\} = \{0\}
\end{aligned} \tag{6.4}$$

6.4.4 Hybrid Simulation Results and Validations

The results of hybrid model of the CORW prototype building obtained by hybrid simulation was compared with the response of pure numerical simulation model used in Chapter 5 subjected to the same earthquake excitation under DBE level. The results show a good match between match analytical results and hybrid simulation results. As shown in Figure 6.14, the resulted roof drift of hybrid simulation is slightly higher than analytical simulation because of the slippage and measurement errors occurred in the experimental testing.

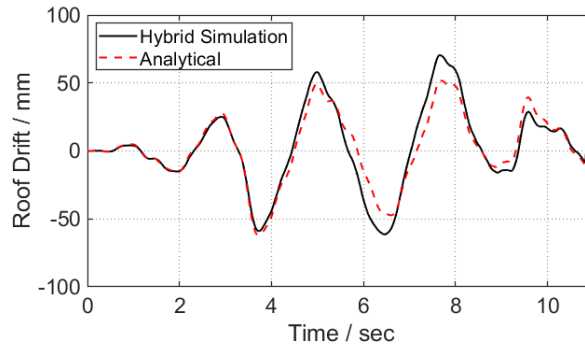


Figure 6.14. Roof drift time history comparison between hybrid simulation and analytical simulation

As shown in Figure 6.15, the difference in base moment of hybrid simulation and analytical simulation is much smaller as the system level force is capped by the energy dissipation devices. This results also indicate that seismic forces are controlled well in CORW system with HF2V devices. The overstrength of the system is minor.

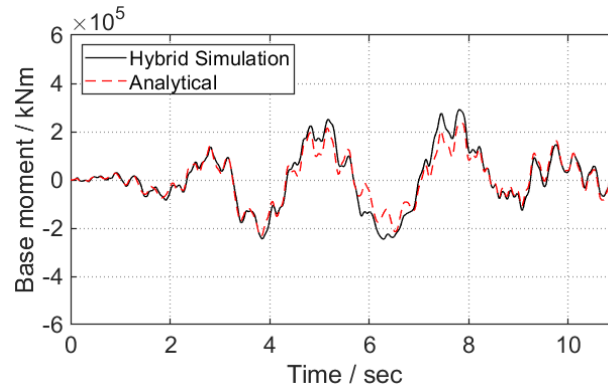


Figure 6.15. Base moment time history comparison between hybrid simulation and analytical simulation

As shown in Figure 6.16 and Figure 6.17, the damper deformation and force obtained from hybrid simulation differ from the analytical simulation more than global response. In general, the damper deformation is larger than analytical results by 10~20%. This difference comes from the discrepancy between idealized constitutive model and realistic damper behaviors. First, some slippage exists in the true pin connection. Clearance between the clevis of the damper and the pin hole the reaction seat allows movement of the pin. The clearance depends on the manufacturing quality of the connection, and also the initial position of the damper. Although this slippage has limited influence on the global structural system when damper yields, it may make dampers yield later than expected. Second, the flexibility of the pin rod may also affect the deformation. Third, the HF2V device exhibits nonlinearity upon yielding, but this nonlinearity is not considered well in the idealized constitutive model.

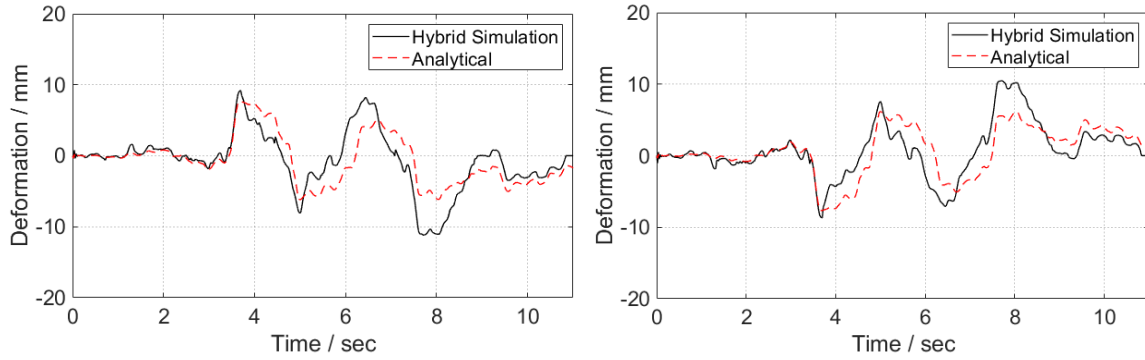


Figure 6.16. Damper displacement comparison between hybrid simulation and analytical simulation

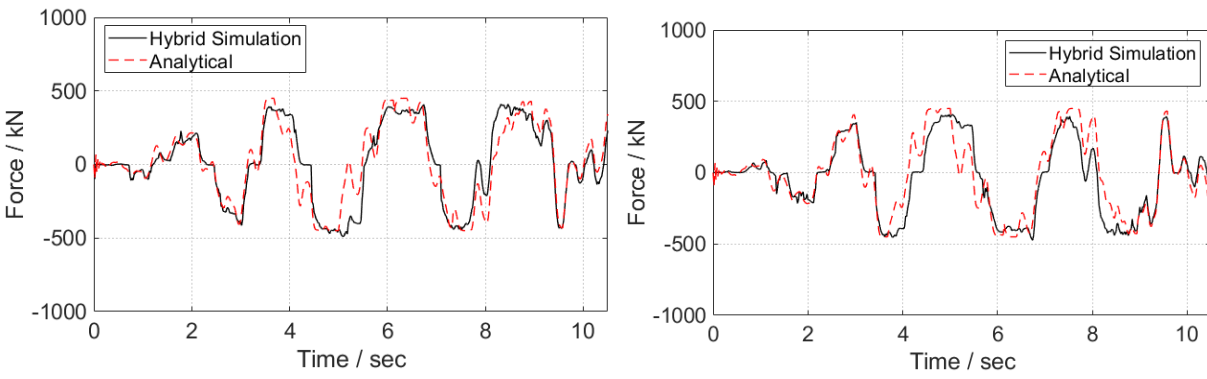


Figure 6.17. Damper force time history comparison between hybrid simulation and analytical simulation

The result obtained from hybrid simulation indicates fair match to the analytical results. The match indicates that the analytical simulation is valid. It also indicates that the hybrid simulation is a powerful tool to evaluate seismic performance of CORW system at low cost and good accuracy.

Chapter 7: Conclusion

This study presents the design and seismic performance assessment of the innovative Controlled Outrigger Rocking Wall (CORW) system implementing different types of dampers. CORW system is a novel structural system which combines concrete wall with damped outrigger and rocking base. In this paper, detailed design procedures for the CORW and the dampers using the equivalent energy design procedure (EEDP) is systematically presented. The seismic performance of the EEDP designed CORW with 25 different dampers combinations was systematically examined using nonlinear time history analysis. The results show EEDP can effectively design the CORW to achieve different performance at different levels of earthquake shaking intensities. At the service level earthquake (SLE), all structural components remained elastic. Hence the structure has achieved the immediately occupancy (IO) performance objective. At the design base earthquake (DBE), only the outrigger dampers have yielded, while the rest of the structural component remains elastic. Hence, the structure has achieved rapid return (RR) performance objective. At the maximum credible earthquake (MCE), both the outrigger and base dampers have yielded, while the global structural response still remain stable, hence the structure has achieved collapse prevention (CP) objective. Overall, the study shows that CORW is a robust structural system for tall building seismic applications, where the performance can be well controlled using with different dampers configurations.

Further research can be done regarding the following directions:

- 1) Hybrid simulation of the innovative CORW system with viscous dampers: Hybrid simulation is a powerful tool to experimentally evaluate the seismic behavior of tall rocking systems (with pounding effects). The hybrid simulation done in this study is merely a validation of the numerical simulation. It only focuses on HF2V damper (considered as a hysteretic damper). Further research could be done to experimentally test more dampers with the hybrid model and setup.
- 2) Numerical studies show viscous damper is also good energy dissipator solution for CORW system.

It is also valuable to conduct real-time hybrid simulation of CORW system where viscous dampers

are experimentally tested, to further evaluate system behavior with viscous dampers, as an alternative solution to energy dissipation for CORW or other rocking systems.

- 3) Refine the design of viscous damper for CORW system: The design of viscous damper for CORW system utilizes velocity correction factor to relate pseudo-velocity to actual velocity. The procedure of obtaining velocity correction factor is sometimes complicated, and the design requires iterations. Further research needs to be done to refine the design procedure to make it simpler and easier.

Bibliography

Aprile, A., Inaudi, J. A., & Kelly, J. M. (1997). Evolutionary Model of Viscoelastic Dampers for Structural Applications. *Journal of Engineering Mechanics, ASCE*, 123(6), 551-560.

Belleri, A., Schoettler, M. J., Restrepo, J. I., & Fleischman, R. B. (2014). Dynamic Behavior of Rocking and Hybrid Cantilever Walls in Precast Concrete Building. *ACI structural journal*, 111(3).

Chen, Y., McFarland, D. M., Wang, Z., Spencer, B. F., & Bergman, L. A. (2010). Analysis of Tall Buildings with Damped Outriggers. *Journal of structural engineering, ASCE*, 136(11), 1435-1443.

Christopoulos, C., & Montgomery, M. (2013). Viscoelastic Coupling Dampers (Vcds) for Enhanced Wind and Seismic Performance of High-Rise Buildings. *Earthquake Engineering & Structural Dynamics*, 42(15), 2217-2233.

Christopoulos, C., Tremblay, R., Kim, H.-J., & Lacerte, M. (2008). Self-Centering Energy Dissipative Bracing System for the Seismic Resistance of Structures: Development and Validation. *Journal of structural engineering, ASCE*, 134(1), 96-107.

Crozet, V., Politopoulos, I., & Chaudat, T. (2019). Shake Table Tests of Structures Subject to Pounding. *Earthquake Engineering & Structural Dynamics*, 48(10), 1156-1173.

Freeman, S. A. (1998). *The Capacity Spectrum Method*. Paper presented at the Proceedings of the 11th European conference on earthquake engineering, Paris, France.

Hall, J. F. (2006). Problems Encountered from the Use (or Misuse) of Rayleigh Damping. *Earthquake Engineering & Structural Dynamics*, 35(5), 525-545.

Hashemi, A., Zarnani, P., Masoudnia, R., & Quenneville, P. (2018). Experimental Testing of Rocking Cross-Laminated Timber Walls with Resilient Slip Friction Joints. *Journal of structural engineering, ASCE*, 144(1), 04017180.

Hashemi, A., Zarnani, P., & Quenneville, P. (2018). *Development of Resilient Seismic Solutions for Timber Structures Using the Resilient Slip Friction Joint (RSFJ) Technology*. Paper presented at the World conference on timber engineering.

Henry, R. (2011). *Self-Centering Precast Concrete Walls for Buildings in Regions with Low to High Seismicity*. (Ph. D.), University of Auckland,

Henry, R., Brooke, N. J., Sritharan, S., & Ingham, J. M. (2012a). Defining Concrete Compressive Strain in Unbonded Post-Tensioned Walls. *ACI structural journal*, 109(1).

Henry, R., Ingham, J., & Sritharan, S. (2012b). *Wall-to-Floor Interaction in Concrete Buildings with Rocking Wall Systems*. Paper presented at the New Zealand Society of Earthquake Engineering Conference, Christchurch, New Zealand.

Huang, B., & Takeuchi, T. (2017). Dynamic Response Evaluation of Damped-Outrigger Systems with Various Heights. *Earthquake Spectra*, 33(2), 665-685.

Kurama, Y., Pessiki, S., Sause, R., & Lu, L.-W. (1999a). Seismic Behavior and Design of Unbonded Post-Tensioned Precast Concrete Walls. *PCI journal*, 44(3), 72-89.

Kurama, Y., Sause, R., Pessiki, S., & Lu, L.-W. (1999b). Lateral Load Behavior and Seismic Design of Unbonded Post-Tensioned Precast Concrete Walls. *ACI structural journal*, 96(4).

Kurama, Y. (1997). *Seismic Analysis, Behavior, and Design of Unbonded Post-Tensioned Precast Concrete Walls*. (9730301 Ph.D.), Lehigh University, Bethlehem, Pennsylvania.

Kurama, Y. (2000). Unbonded Post-Tensioned Precast Concrete Walls with Supplemental Viscous Damping. *ACI Structural Journal*, 97(4), 648-658.

Landi, L., Fabbri, O., & Diotallevi, P. P. (2014). A Two-Step Direct Method for Estimating the Seismic Response of Nonlinear Structures Equipped with Nonlinear Viscous Dampers. *Earthquake Engineering & Structural Dynamics*, 43(11), 1641-1659.

Lin, P.-C., Takeuchi, T., & Matsui, R. (2018). Seismic Performance Evaluation of Single Damped-Outrigger System Incorporating Buckling-Restrained Braces. *Earthquake Engineering & Structural Dynamics*, 47(12), 2343-2365.

Liu, R., & Palermo, A. (2020). Characterization of Filler-Free Buckling Restrained Fuse-Type Energy Dissipation Device for Seismic Applications. *Journal of structural engineering, ASCE*, 146(5), 04020059.

Marriott, D. (2009). *The Development of High-Performance Post-Tensioned Rocking Systems for the Seismic Design of Structure*. (Ph. D.), University of Canterbury, Christchurch, New Zealand.

Mortazavi, S. M. R., Ghassemieh, M., & Ghobadi, M. S. (1992). ATC-24, Guidelines for Seismic Testing of Components of Steel Structures.

Nazari, M., Sritharan, S., & Aaleti, S. (2017). Single Precast Concrete Rocking Walls as Earthquake Force-Resisting Elements. *Earthquake Engineering & Structural Dynamics*, 46(5), 753-769.

NRCC. (2015). National Building Code of Canada 2015, Ottawa, Canada.

Pan, P., Wu, S., & Nie, X. (2015). A Distributed Parameter Model of a Frame Pin-Supported Wall Structure. *Earthquake Engineering & Structural Dynamics*, 44(10), 1643-1659.

PEER. (2006). Opensees: Open System for Earthquake Engineering Simulation: Pacific Earthquake Engineering Research Center, University of California, Berkeley, California.

PEER. (2013). *PEER NGA-West2 Database*: Pacific Earthquake Engineering Research Center (PEER), University of California, Berkeley, California.

Perez, F. J. (1998). *Lateral Load Behavior and Design of Unbonded Post-Tensioned Precast Concrete Walls with Ductile Vertical Joint Connectors*. (Ph. D.), Lehigh University, Bethlehem, Pennsylvania.

Perez, F. J. (2004). *Experimental and Analytical Lateral Load Response of Unbonded Post-Tensioned Precast Concrete Walls*. (Ph. D.), Lehigh University, Bethlehem, Pennsylvania.

Perez, F. J., Sause, R., & Pessiki, S. (2007). Analytical and Experimental Lateral Load Behavior of Unbonded Posttensioned Precast Concrete Walls. *Journal of structural engineering, ASCE*, 133(11), 1531-1540.

Priestley, M. J. N., Sritharan, S., Conley, J. R., & Pampanin, S. (1999). Preliminary Results and Conclusions from the Presss Five-Story Precast Concrete Test Building. *PCI Journal*, 44(6), 42-67.

Qu, Z., Wada, A., Motoyui, S., Sakata, H., & Kishiki, S. (2012). Pin-Supported Walls for Enhancing the Seismic Performance of Building Structures. *Earthquake Engineering & Structural Dynamics*, 41(14), 2075-2091.

Ramirez, O. M. (2001). *Development and Evaluation of Simplified Procedures for the Analysis and Design of Buildings with Passive Energy Dissipation Systems*. (Ph.D.), State University of New York at Buffalo, Buffalo, New York.

Restrepo, J. I., & Rahman, A. (2007a). Seismic Performance of Self-Centering Structural Walls Incorporating Energy Dissipators. *Journal of structural engineering, ASCE*, 133(11), 1560-1570.

Restrepo, J. I., & Rahman, A. (2007b). Seismic Performance of Self-Centering Structural Walls Incorporating Energy Dissipators. *Journal of Structural Engineering*, 133(11), 1560-1570.

Rodgers, G. W. (2009). *Next Generation Structural Technologies: Implementing High Force-to-Volume Energy Absorbers*. (Ph. D.), University of Canterbury, Christchurch, New Zealand.

Rodgers, G. W., Chase, J., Causse, R., Chanchi, J., & MacRae, G. A. (2017). Performance and Degradation of Sliding Steel Friction Connections: Impact of Velocity, Corrosion Coating and Shim Material. *Engineering Structures*, 141, 292-302.

Rodgers, G. W., Solberg, K. M., Chase, J. G., Mander, J. B., Bradley, B. A., Dhakal, R. P., & Li, L. (2008). Performance of a Damage - Protected Beam - Column Subassembly Utilizing External Hf2v Energy Dissipation Devices. *Earthquake Engineering & Structural Dynamics*, 37(13), 1549-1564.

Sadeghi, M. A., Yang, T. Y., Bagatini-Cachuço, F., & Pan, S. (2020). Seismic Design and Performance Evaluation of Controlled Rocking Dual-Fused Bridge System. *Engineering Structures*, 212, 110467.

Seleemah, A., & Constantinou, M. C. (1997). *Investigation of Seismic Response of Buildings with Linear and Nonlinear Fluid Viscous Dampers*: National Center for Earthquake Engineering Research Buffalo, State University of New York at Buffalo, Buffalo, New York.

Shoujun, W., Peng, P., & Dongbin, Z. (2016). Higher Mode Effects in Frame Pin-Supported Wall Structure by Using a Distributed Parameter Model. *Earthquake Engineering & Structural Dynamics*, 45(14), 2371-2387.

Smith, R. J., & Willford, M. R. (2007). The Damped Outrigger Concept for Tall Buildings. *Structural Design of Tall & Special Buildings*, 16(4), 501-517.

Sritharan, S., Aaleti, S., Henry, R. S., Liu, K.-Y., & Tsai, K.-C. (2015). Precast Concrete Wall with End Columns (Prewec) for Earthquake Resistant Design. *Earthquake Engineering & Structural Dynamics*, 44(12), 2075-2092.

Sritharan, S., Aaleti, S., & Thomas, D. J. (2007). *Seismic Analysis and Design of Precast Concrete Jointed Wall Systems*. Retrieved from Precast/Prestressed Concrete Institute.

Tobber, L., & Yang, T. Y. (2020). *Development of Next Generation High-Performance Earthquake-Resilient Tall Buildings*. Retrieved from International Joint Research Laboratory of Earthquake Engineering (ILEE), Shanghai, China.

Tobber, L., Yang, T. Y., & Adebar, P. (2018). *Development of High-Performance Earthquake-Resilient Tall Buildings*. Paper presented at the Eleventh U.S. National Conference on Earthquake Engineering, Los Angeles, California.

Twigden, K., & Henry, R. S. (2015). *Experimental Response and Design of O-Connectors for Rocking Wall Systems*. Retrieved from University of Auckland, Auckland, New Zealand.

Twigden, K. M., Sritharan, S., & Henry, R. S. (2017). Cyclic Testing of Unbonded Post-Tensioned Concrete Wall Systems with and without Supplemental Damping. *Engineering Structures*, 140, 406-420.

Watkins, J., Henry, R., & Sritharan, S. (2014). *Computational Modeling of Self-Centering Precast Concrete Walls*. Paper presented at the 4th ECCOMAS Thematic Conference on Computational Methods in Structural Dynamics and Earthquake Engineering, Kos Island, Greece.

Xing, L., Zhou, Y., & Aguaguña, M. (2019). Optimal Vertical Configuration of Combined Energy Dissipation Outriggers. *The Structural Design of Tall and Special Buildings*, 28(4), e1579.

Yahya, C. K. (2000). Seismic Design of Unbonded Post-Tensioned Precast Concrete Walls with Supplemental Viscous Damping. *ACI structural journal*, 97(4).

Yang, T. Y., Banjuradja, W., & Tobber, L. (2018). Experimental Test of Welded Wide Flange Fuses. *Key Engineering Materials*, 763, 414-422.

Yang, T. Y., Li, T., Tobber, L., & Pan, X. (2019). Experimental Test of Novel Honeycomb Structural Fuse. *Engineering Structures*, 201, 109814.

Yang, T. Y., Tung, D. P., & Li, Y. (2018). Equivalent Energy Design Procedure for Earthquake Resilient Fused Structures. *Earthquake Spectra*, 34(2), 795-815.

Zhou, Y., & Li, H. (2014). Analysis of a High-Rise Steel Structure with Viscous Damped Outriggers. *The Structural Design of Tall and Special Buildings*, 23(13), 963-979.

Zhou, Y., Zhang, C., & Lu, X. (2017). Seismic Performance of a Damping Outrigger System for Tall Buildings. *Structural Control and Health Monitoring*, 24(1), e1864.

Appendices

Appendix A Ground motions

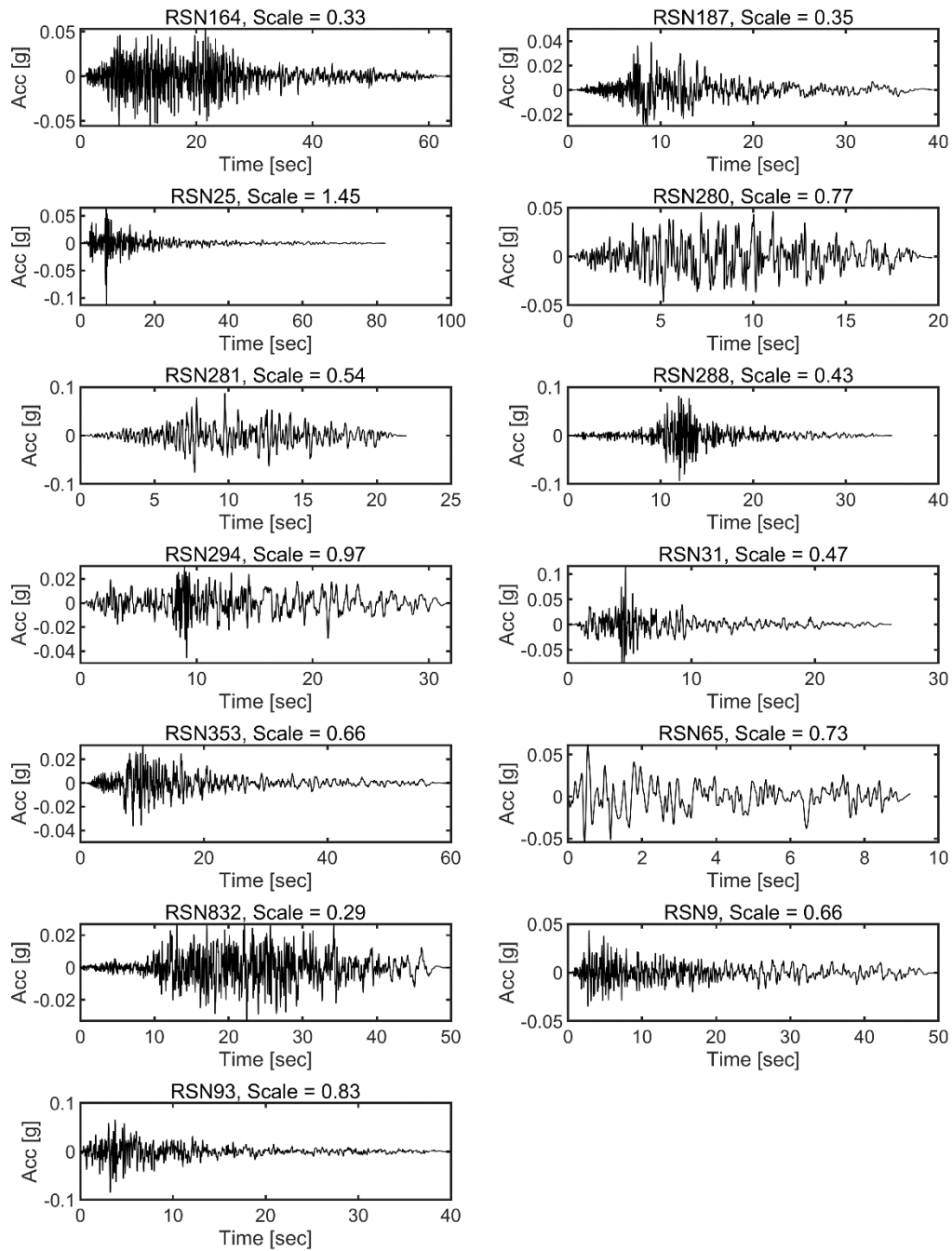


Figure A.1. motion time histories under SLE (1~13)

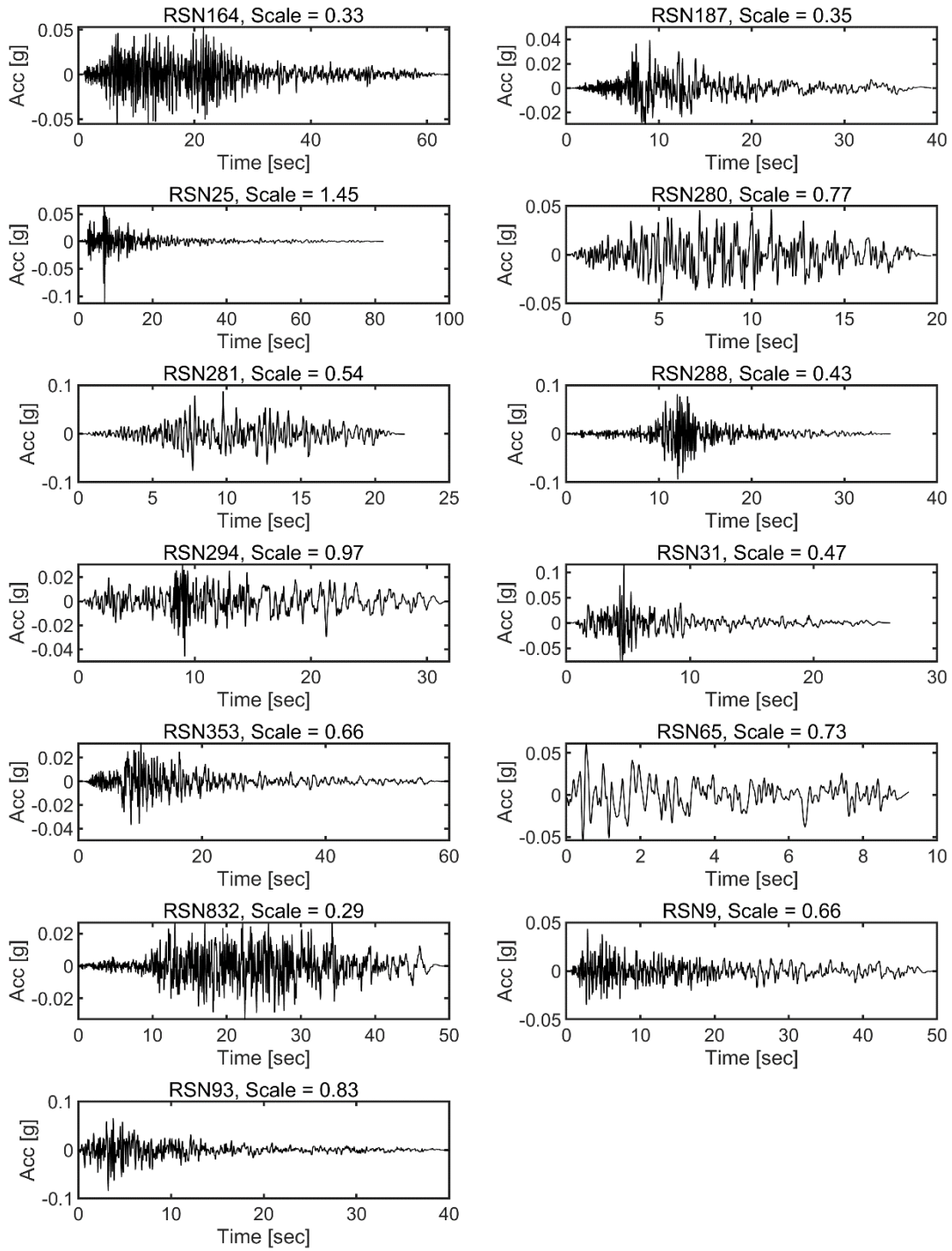


Figure A.2. Ground motion time histories under DBE (1~13)

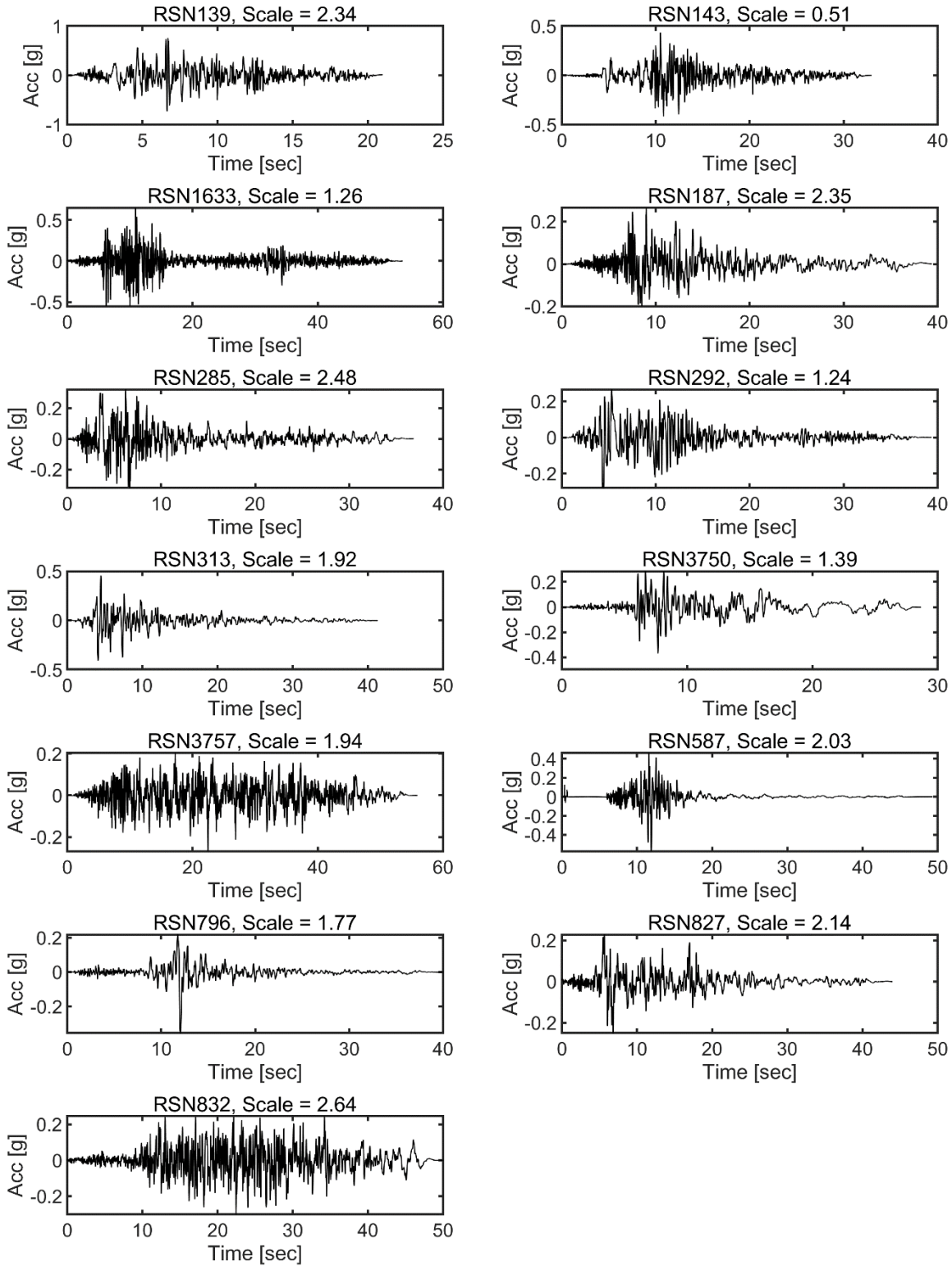


Figure A.3. Ground motion time histories under MCE (1~13)

Appendix B Resulted damper Hysteretic Loops

This appendix shows damper hysteresis at all hazard levels under alternative typical ground motions, normalized to design values (in black dashed lines). Black and red dashed lines indicate dampers at different locations.

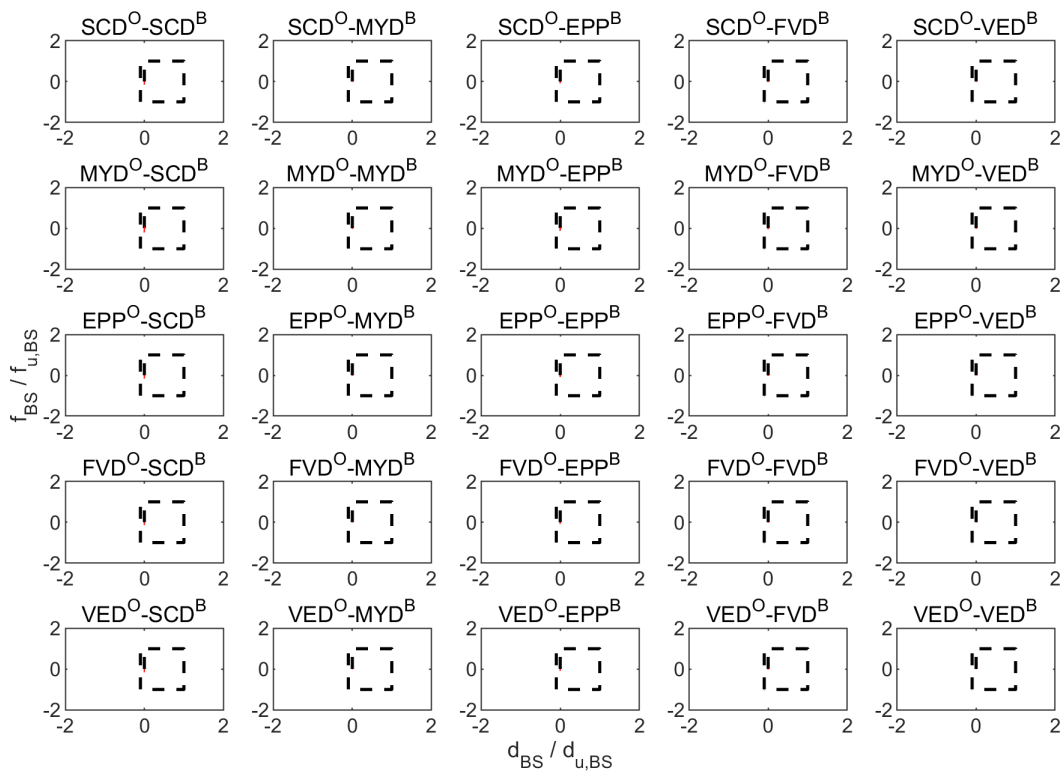


Figure B.1. Base damper hysteresis at SLE level (GM #25)

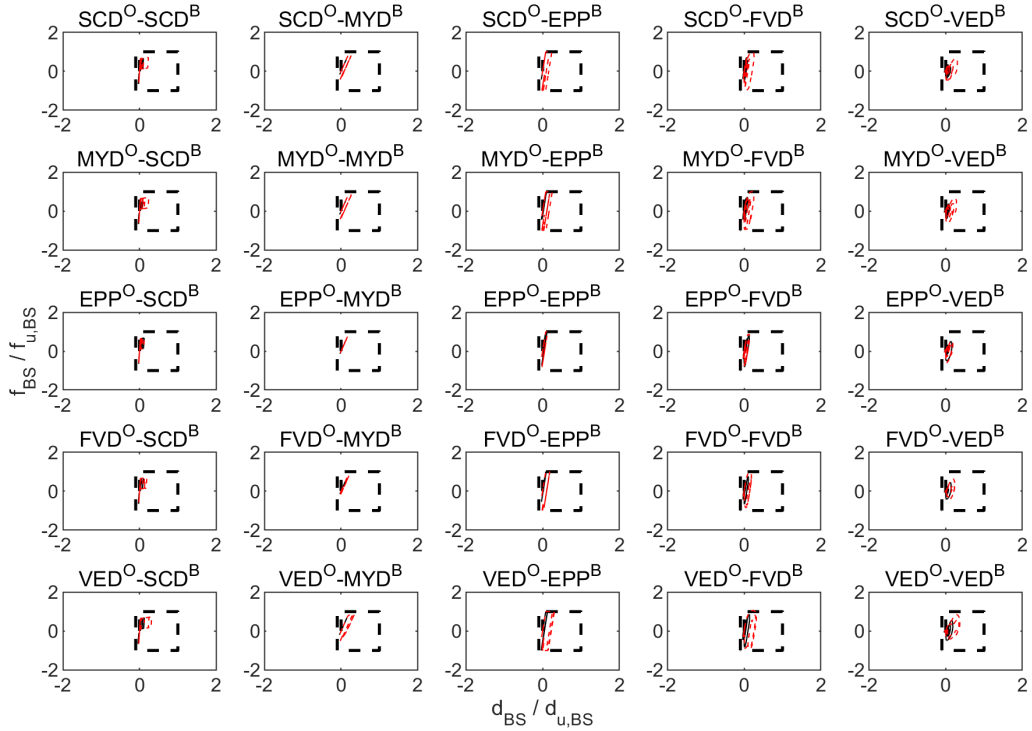


Figure B.2. Base damper hysteresis at DBE level (GM #9)

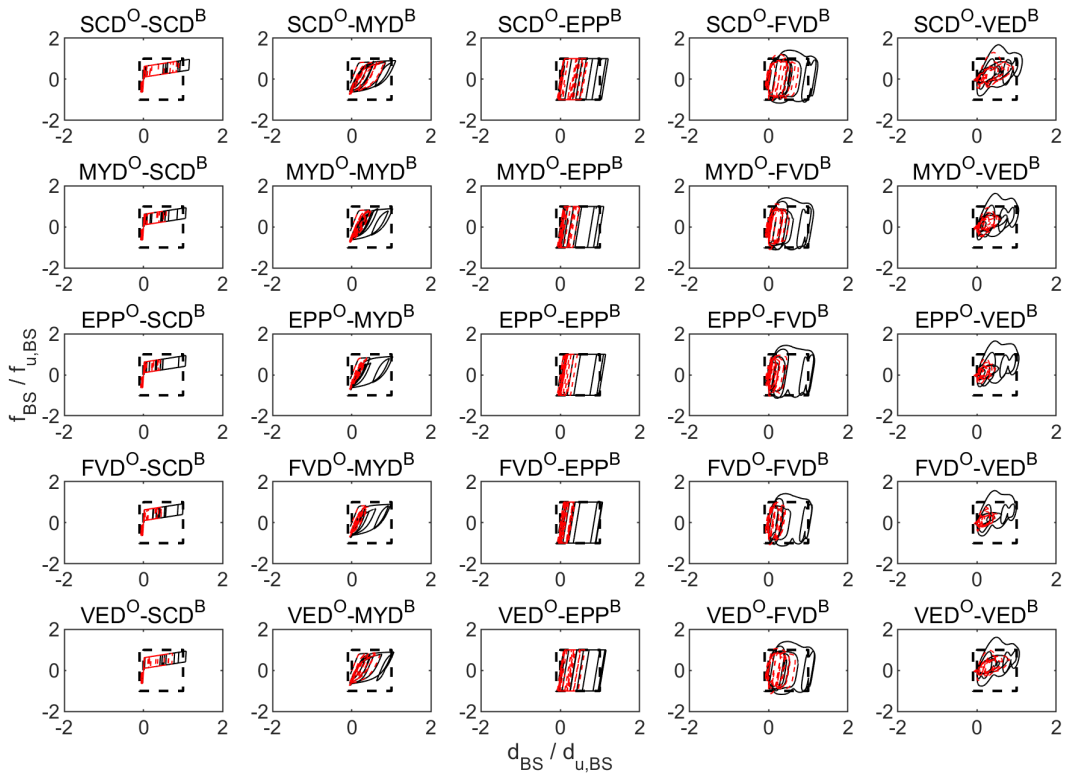


Figure B.3. Base damper hysteresis at MCE level (GM #832)

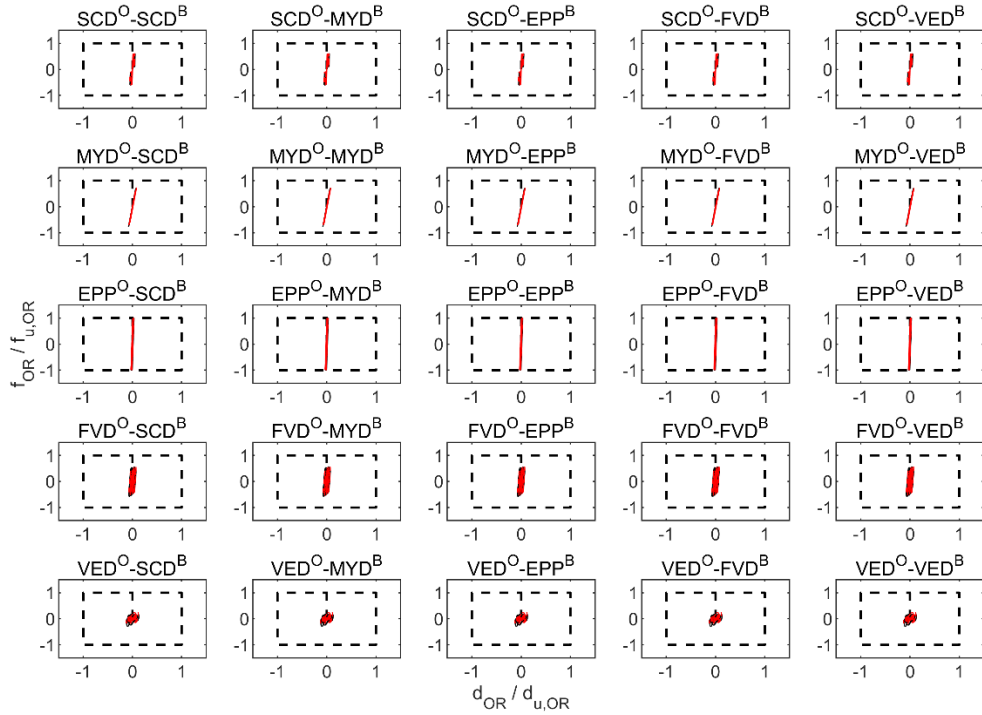


Figure B.4. Outrigger damper hysteresis at SLE level (GM #187)

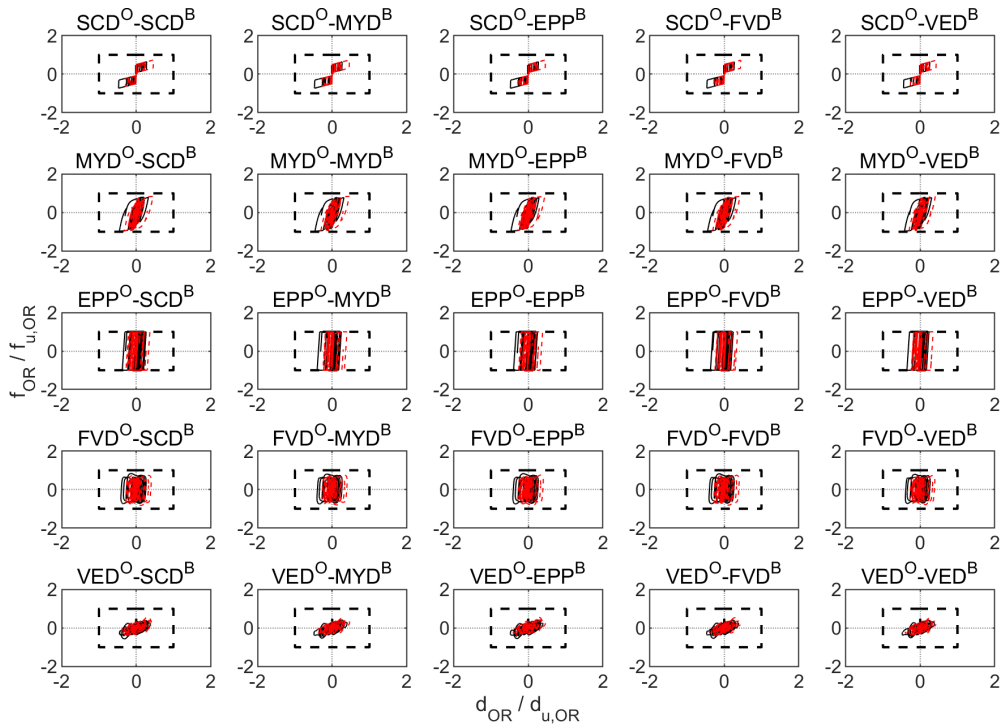


Figure B.5. Outrigger damper hysteresis at DBE level (GM #6)

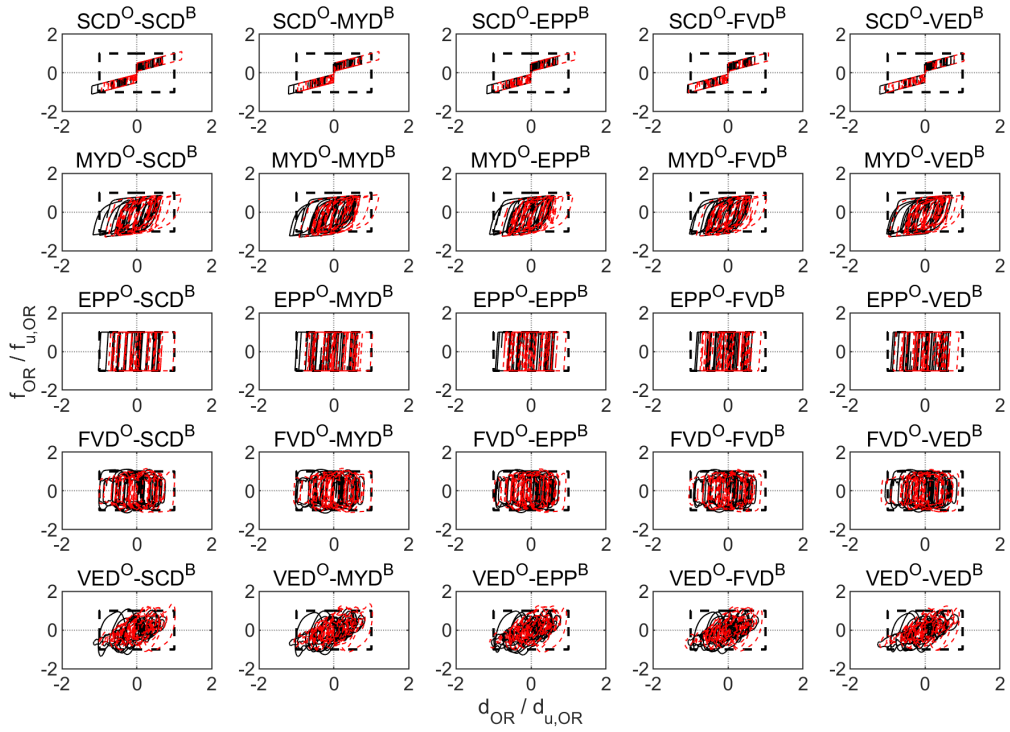


Figure B.6. Outrigger damper hysteresis at MCE level (GM #139)